Doctoral Dissertations and Master's Theses

Fall 12-2017

Design of Flight Control Laws for a Novel Stratospheric Dual-Aircraft Platform

Cindy Nshuti
Embry-Riddle Aeronautical University

Follow this and additional works at: https://commons.erau.edu/edt

Part of the Aerospace Engineering Commons, and the Automotive Engineering Commons

DESIGN OF FLIGHT CONTROL LAWS FOR A NOVEL STRATOSPHERIC DUAL-

AIRCRAFT PLATFORM

A Thesis

Submitted to the Faculty

of

Embry-Riddle Aeronautical University

by

Cindy Nshuti

In Partial Fulfillment of the

Requirements for the Degree

of

Master of Science in Unmanned and Autonomous Systems Engineering

December 2017

Embry-Riddle Aeronautical University

Daytona Beach, Florida

DESIGN OF FLIGHT CONTROL LAWS FOR A NOVEL STRASTOSPHERIC DUAL-AIRCRAFT PLATFORM

by

Cindy Nshuti

A Thesis prepared under the direction of the candidate's committee chairman, Dr. Hever Moncayo, Department of Aerospace Engineering, and has been approved by the members of her thesis committee. It was submitted to the School of Graduate Studies and Research and was accepted in partial fulfillment of the requirements for the degree of Master of Science in Unmanned and Autonomous Systems Engineering.

THESIS COMMITTEE

Chairman, Dr. Hever Moncayo

Member, Dr. William Engblom
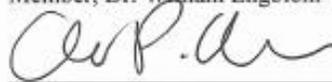
Member, Dr. Claudia Moreno

Graduate Program Coordinator, Dr. Richard Stansbury

Date 12/6/17

Dean of College of Engineering, Dr. Maj Mirmirani,

Date 12/6/17
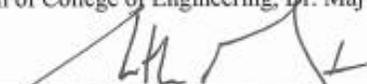
Vice Chancellor, Academic Support, Dr. Christopher Grant

Date 12/6/17

ACKNOWLEDGMENTS

TABLE OF CONTENTS

LIST OF TABLES

LIST OF FIGURES

SYMBOLS

α	Angle of attack
β	Sideslip angle
ϕ, θ, ψ	Euler angles
u, v, w	Body frame velocities
$a_x\ a_y\ a_z$	Body frame accelerations
p, q, r	Roll rate, pitch rate, yaw rate
$\delta_e \delta_r \delta_a \delta_f$	Elevator, Rudder, Aileron, Flaps
ζ	Scale factor

ABBREVIATIONS

ADB	Air Data Boom
DAP	Dual-Aircraft Platform
DCM	Direct Cosine Matrix
EKF	Extended Kalman Filter
ERAU	Embry-Riddle Aeronautical University
FDCRL	Flight Dynamics Control Research Lab
GCS	Ground Control Station
GPS	Global Positioning system
IMU	Inertial Measurement Unit
KSC	NASA Kennedy Space Center
KF	Kalman Filter
NED	North-East-Down reference frame
PI	Performance Index
PID	Proportional Integral Derivative
PWM	Pulse Width Modulation
PX4	Pixhawk Autopilot
RC	Radio Control
RX	Receiver
SLF	NASA Shuttle Landing Facility
SPR	Strictly Positive Real
TX	Transmitter
UAS/UAV	Unmanned Autonomous Systems/Vehicle
uORB	micro-Object-Request-Broker application

ABSTRACT

Dual-aircraft platform (DAP) is a novel concept that features two glider-like unmanned aerial systems (UAS) tethered via a thin adjustable cable allowing them to sail back-and-forth, without propulsion, using vertical wind shear. DAP offers the potential of a low-cost atmospheric satellite. This thesis presents the results of an initiative to demonstrate this novel flight concept through modeling, simulation, and flight testing at Embry-Riddle Aeronautical University (ERAU).

A realistic simulation environment, described herein, was developed to support the development and testing of flight control systems. This environment includes nonlinear aerodynamic models for the aircraft, a multi-element cable dynamics model, propeller-motor thrust model, control surface actuator models, and permits time-varying wind profiles. This simulator offers both pilot-in-the-loop control and autonomous sailing flight control, and X-Plane interface to provide visualization cues.

An intensive flight test program, described herein, was conducted to support the validation of the DAP concept. MAXA Pro 4m gliders were assembled, instrumented, and flight tested in an effort to physically demonstrate the sailing mode of flight. The flight test program described here focuses on the capability to sail with one aircraft (i.e., fly without propulsion) while "towing" (i.e., pulling) a moving truck as an intermediate step towards the more complex scenario of sailing with two connected aircraft.

Two vital elements of the flight software are implemented and analyzed herein. The accuracy of wind estimation techniques is evaluated using flight testing. The robustness of an $\mathcal{L}_1$ adaptive controller is evaluated within the flight simulation environment by comparing its performance with a conventional controller.

CHAPTER 1: Introduction

1.1. Background

Aircraft platforms that can station-keep in the stratosphere for years at a time are often referred to as Atmospheric Satellites because they can perform the same functions as satellites, including providing broadband service and capturing images from on high. However unlike stationary orbiters, these platforms can be retrieved, upgraded and reused. They could be operated and bought at a fraction of the cost of current orbital satellites, and therefore can be used in missions such as patrolling national borders, expanding cellular coverage or monitoring the ozone layer (Bleicher, 2013).

Atmospheric Satellites are expected to make an enormous impact on society by diversifying and expanding surveillance capabilities, communication bandwidths and availability. They could potentially be integrated into the National Airspace System (NAS) to improve inter-aircraft communications and support navigation. Although atmospheric satellites have the potential for exceptional societal and economic impact the platforms present a long-standing challenge to the aeronautics community (Engblom & Decker, 2016).

Previous efforts include the various versions of Solara by Titan Aerospace which was acquired by Google in 2014. The Solara drones use solar-power for flight and to power to their payload, the solar panels also charge batteries for night flight. This means there are dependent on location and the time of year, and for longer daylight hours to support payload (Gallagher, 2013). Other solar powered attempts include Boeing and DARPA's SolarEagle, Airbus's Zephyr and NASA's AeroVironment's Helios which have not been entirely successful, the latter crashed during a climb to altitude when a cloud intercepted

the sun (Boyle, 2016). In order to improve the solar energy collected, the wing structures are very large and flexible which creates a limit to the aircraft's structural integrity and system reliability.

Northrop Grumman's Global Hawk is a fueled aircraft so it is limited in range and endurance measured in days, and amount of payload requiring power. There is also Concordia Project a high-altitude balloon however they are not expected to station-keep and their flight paths are dependent on prevailing winds (Engblom W. , 2014).

An alternative method for achieving long endurance flights is dynamic soaring, that is extracting energy from the available wind shear. Dynamic soaring is a specialized form of gliding flight that is revealed in nature by birds such as the albatross seabird which harnesses abundant energy during flight by flying through a boundary layer between two layers of air with different wind velocities (Sechrist, 2002). Research such as Selig (Sukamar & Selig, 2013) has demonstrated that it is possible to perform dynamic soaring in high-wind conditions at high altitudes in the atmospheric boundary layer with model-scale unpowered sailplanes having both high lift-to-drag ratio and high wing loading. Dynamic soaring is also observed in remote-controlled sailplanes using wind gradients created by mountain ridges (Sechrist, 2002).

1.2. Dual-Aircraft Platform

The Dual-Aircraft Platform (DAP) is fundamentally different from the aforementioned atmospheric satellite concepts. DAP, illustrated in Figure 1, is a patented concept which uses wind gradients as the primary energy source with the potential to station-keep for long periods of time and sail within the stratosphere (i.e. above 60,000ft) (Palm Coast, FL, US Patent No. 8,931,727 B2, 2015). This novel concept features two

glider-like unmanned aerial systems (UAS) tethered via a strong, thin adjustable cable allowing them to sail back-and-forth without propulsion using levels of natural wind shears at different altitudes (Engblom W. , 2014).

Figure 1 Dual-aircraft platform configuration (Engblom W. A., et al., 2016)

In principle, the UAS platforms operate similar to kite-surfing in which the upper glider described as the *SAIL*, provides lift and aerodynamic thrust, while the lower glider referred to as the *BOARD*, prevents the platform from drifting downwind by providing an upwind force displayed in Figure 1 (Engblom & Decker, 2016). The nonlinearities due to the combination of two UAS, cable dynamics and wind make this an unprecedented dynamic and control problem and require the development of simulation tools and advanced control architectures. This thesis study supports the proof of DAP through modeling, simulation and flight testing.

1.3. Literature Review

1.3.1. Controllers

An exact model is often unavailable when designing a controller for any plant, uncertainties such as external forces, dynamic friction or additional dynamics due to damaged parts can significantly affect the plant and can be hard to model and sense. A good controller needs to be capable to counteract those uncertainties (Mehdi S. B., 2012).

1.3.2. Conventional Controllers

Conventional controllers play a vital role in industries such as manufacturing, aerospace, robotics and other prominent industrial fields. Consequently, there is extensive theoretical examples and design methods. Advantages include their simplicity, transparent nature and adequate performance (Ting & Ayoubi, 2012). Some well-known approaches include: linear quadratic optimal regulator and proportional, integral and derivative (PID) (Pfeifer & Kassab, 2012). Apart from these, design techniques such as pole placement are also used to achieve desired system dynamics.

In aerospace, linear quadratic control techniques have been used for both rotary UAVs (Franko, 2009) and fixed wing UAVs (Kinoshita & Imado, 2006). In (Masar & Stohr, 2011) gain-scheduled linear quadratic regulator (LQR) controller is developed for an autonomous airship. LQR has shown to be effective on a number of UAV applications (Oner, et al., 2009). To improve the overall effectiveness and disturbance rejection (Hajiyev & S., 2013) applied a Kalman Estimator to the LQR control system.

Pole assignment or pole placement is a linear methodology employed to locate the poles of the closed-loop system ensuring the desired dynamic response. It is only applied

for systems that are fully controllable and observable. (Sung & Yoonsu, 2003) demonstrates a linear dynamic feedback controller utilizing pole placement and Kalman Filtering for a UAV's control system. For numerous problems, it is unnecessary to have exact placement hence it is sufficient to place the poles in the left-half-plane of the closed-loop system (Chilali & Gahinet, 1996).

PID controllers widely used for UAV applications (Beard, et al., 2005) (Beard & McLain, 2012), such as fixed wing (Kada & Ghazzawi, 2011), rotary wings (Perhinschi, 1997), quadrotors (Salih, Moghavvemi, Mohamed, & Gaeid, 2010) (Jun & Yuntang, 2011) and lighter-than-air aircrafts (Azinheira, Paivab, Ramos, & Bueno, April 2000). (Wilburn, Perhinschi, Moncayo, Karas, & Wilburn, 2013) shows that both outer and inner loop can be based on PID controller compensation.

(Ting & Ayoubi, 2012) points out that for nonlinear systems with unknown characteristics or unknown functions in high performance operating conditions, that these ranges may exceed the potential of conventional controllers.

1.3.3. Adaptive Controllers

An adaptive controller has the ability to control a plant with uncertainties. The main idea is to approximate the uncertainties by observing output or state of the system, then adapting to them appropriately. Contingent on current operational conditions, the adaptive controller is capable of modifying its own structure and/or parameters (gains). Although majority of design methods for adaptive control systems focus only on the variation of the gains rather than modifying the structure (Krishnamoorthy, 2015). The dynamics of an aircraft are non-linear and time varying and they operate over a wide range of speeds and altitudes which means they can profit from adaptive control laws.

Model Reference Adaptive Control (MRAC) is a traditional adaptive control architecture that is widely used and is shown to have good features in terms of performance such as the time-diminishing error on tracking the reference model and it provides the possibility for rigorous stability proofs (Moncayo H. , et al., 2013). For MRAC, to ensure close to desired performance a fast adaption is usually required which unfortunately makes the system less robust (Mehdi, 2012) because increasing adaptation rate will excite an oscillatory high frequency response in the control input, so a limit has to be established on the rate of adaptation and therefore consequently limiting the speed of convergence (Moncayo H. , et al., 2013). A filtered version MRAC, known as $\mathcal{L}_1$ adaptive control has been proposed to mitigate these issues (Cao & Hovakimyan, 2006a) (Cao & Hovakimyan, 2006b).

$\mathcal{L}_1$ control first appeared in 2006 showing its results in (Cao & Hovakimyan, 2006a) and (Cao & Hovakimyan, 2006b), with further developments finalized in (Hovakimyan & Cao, 2010). The significant characteristic of $\mathcal{L}_1$ adaptive control theory is the decoupling of control (action) and adaptation (learning) loops, this guarantees robustness with fast adaptation. In this framework, fast adaptation means that the rate of adaptation can be chosen so that its time scale is faster than the underlying closed loop dynamics and the plant parameter variances. Robust adaptation means that regardless of fast adaption in $\mathcal{L}_1$'s architecture, the properties of robustness for the closed-loop adaptive system can independently be adjusted to the adaptation rate (Kharisov, 2013). The transitory performance of the closed-loop $\mathcal{L}_1$ adaptive system is quantified for both the system input and output by performance bounds with respect to an $\mathcal{L}_1$ reference system which includes a low-pass filter (Kharisov, 2013).

$\mathcal{L}_1$ adaptive control theory has been successfully verified on various simulation environments and flight control systems. (Gregory, Xargay, Cao, & Hovakimyan, 2010) demonstrates that at Ft. Pickett, VA on 4th June 2010 NASA Langley's AirSTAR GTM twin jet flight tests showed that an $\mathcal{L}_1$ adaptive controller significantly improved the pilot's handling qualities at high angles of attack and reduced their workload. More so, the control law had robust performance with the set of desired dynamics and it was able to track the desired states in the presence of stability degradation.

$\mathcal{L}_1$ Controller and Its Parameters
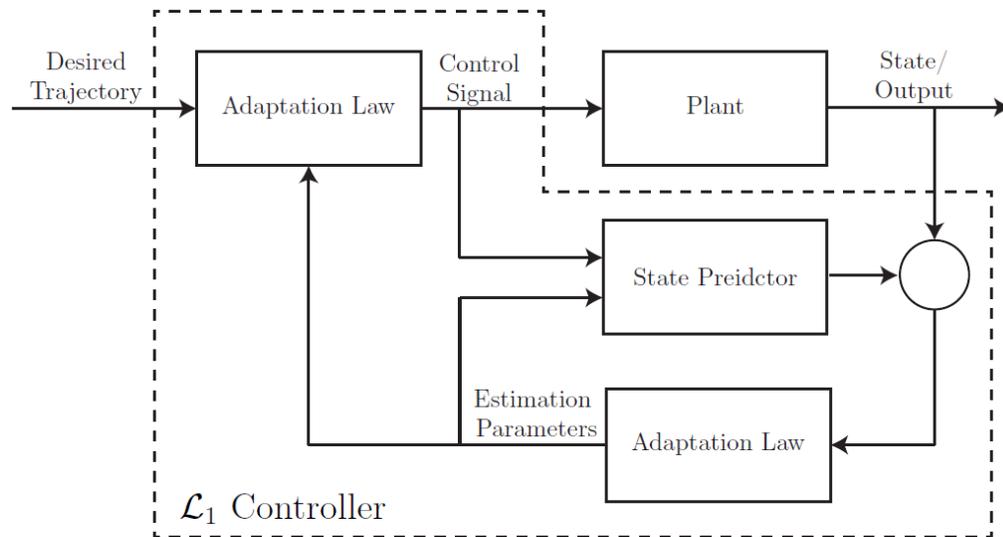
Figure 2 General Structure of $\mathcal{L}_1$ Controller (Mehdi, 2012)

As shown in Figure 2 an $\mathcal{L}_1$ has three components: Adaption Law, State Predictor and Control Law (Hovakimyan & Cao, 2010). The adaption law estimates uncertainties in the plant and updates estimation parameters (also known as controller states). The state

predictor models the plant's desired performance. The control law calculates the controller's output – the control signal and uses the low-pass filter to remove high frequency in the control channel.

The control challenges associated with DAP and the potential of $\mathcal{L}_I$ control theory motivated its implementation in this study, principally in the simulation. This study explores the $\mathcal{L}_I$ adaptive output feedback control architecture to accomplish the tracking objective while guaranteeing robustness and stability in the aim to achieve predetermined sailing conditions.

1.3.4. Wind Sensing Technologies

The nature of the DAP problem requires that in order for the UAS to have full autonomy and sail, the flight computer must have the capability of performing online wind direction and speed. Although this study is not directly related to the development of control laws for DAP, it was performed as an integrative part for a comprehensive test vehicle.

Several methodologies have been investigated in the literature for wind sensing using estimation methods and direct measurement. NASA F-18 High Alpha Research Vehicle implemented and flight tested a nonintrusive high-angle-of-attack flush airdata sensing (FADS) system by installing 9-25 pressure orifices organized in concentric circles on the cone of the vehicle to determine a few parameters including angles of attack and sideslip (Whitmore, 1991).

FADS system is also currently being investigated for small unmanned aircraft systems (sUAS) in (Laurence, Argrow, & Frew, 2016) (Laurence & Argrow, 2017) where during the past 11 years the University of Colorado's Research and Engineering Center for

Unmanned Vehicles (RECUV) has flown sUAS into severe storms such as tornadoes to investigate the capability of sUAS to collect thermodynamic data within the storm. Thus the research requires high-precision wind measurements at a relatively low-cost. Ports for FADS are placed in the inboard of the wings.

Research by (Samy, Postlethwaite, Gu, & Green, 2010) applies neural-networks (NN) with FADS to model the aerodynamic relationship between the air data states and aircraft surface pressure for a mini air vehicle (MAV). (Quindlen & Langelaan, 2013) also applies NN to FADS for UAS sailplane. Neural network algorithms require training and in (Quindlen & Langelaan, 2013) they are trained in the wind tunnel. Or as (Samy, Postlethwaite, Gu, & Green, 2010) concludes that the neurons can be trained against a multi-hole probe. Both studies observe that the NN would require further training in-flight.

A less popular method uses an optical air data system. This sends laser light beams several feet away which measures undisturbed air by the speed and direction of microscopic particles between beams. Famously, it was demonstrated in NASA SR-71 "Blackbird" research aircraft in 1993 (Andersen & Haley).

(Cho, Kang, Park, & Yoo, 2013) and (Rhudy, Larrabee, Chao, Gu, & Napolitano, 2013) implemented wind vanes to complement and/or compare wind estimation methods. In (Rhudy, Larrabee, Chao, Gu, & Napolitano, 2013) two angle of attack vanes and one sideslip vane were attached to potentiometers and flight tested. According to their results the measurements were inaccurate due to susceptibility to wind gust disturbances, sensor noise and noisy data at low airspeed. This hypothesis was echoed in (Cho, Kang, Park, & Yoo, 2013).

Seven-hole Probe

Multi-hole probes (MHP) have long been used in the aerospace field. These probes are an extension on the pitot-tube notion – i.e. the knowing the relative position of each pressure port allows calculation of both a flow magnitude and direction (Crawford, 2011). Three-hole probes are capable of measuring a 2-dimensional flow – i.e. a single flow angle. Five and seven-hole probes are capable of fully measuring a 3-dimensional velocity field – i.e. two flow angles. The two extra holes on the 7-hole probe allow it to measure higher angles of attack. (Bryer, 1971) presents a summary on different types of probes and their calibration.

Literature such as (Zilliac, 1989) describe the calibration of a non-nulling, seven-hole pressure probe. The procedure for calibration depends on the use of differential pressures to define the three components of velocity. 7-hole airdata probes have been shown to have an accuracy of within 1° for mean flow angles and within 1% for mean flow velocity (Crawford, 2011).

Wind Estimation Technique

An alternative approach to directly measuring wind properties is through estimation. There are currently two major wind estimation methodologies for determining the wind speed experienced by an aircraft. The first approach is demonstrated in (Lee, Sevil, Dogan, & Hullender, 2013) (Kumon, Mizumoto, & Iwai, 2005) where information from the aircraft dynamic model is used to predict the effect of wind. The predominant limitation with this wind estimation technique is they require a well-defined mathematical model of the aircraft which is limiting for a UAS where the model has not yet been established. It also introduces additional modeling errors and uncertainties into the system.

The second approach utilizes what is referred to as the "wind triangle relationship". It represents the relationship between wind speed, ground speed and airspeed (Rhudy, Gu, Gross, & Chao, 2017). (McLaren, 2008) study presents a "two-vector method" which uses two successive heading and ground velocity measurements to create triangles for airspeed and wind speed estimation formulated on a constant assumption of wind. In (Arain & Kendoul, 2014) on online estimation on small unmanned rotorcraft (RUAS) is presented. However, the study is limited by the assumption of a known *a priori* wind direction and that the angle of attack and sideslip angle are always zero. (Lefas, 1987) derives a filter called the "velocity bias filter", which is similar to a Kalman filter. It estimates wind using true airspeed, radar measurements and magnetic heading. (Rhudy, Gu, Gross, & Chao, 2017) implements four different nonlinear state-space methods using an Unscented Kalman filter (UKF) as the nonlinear estimator. These methods were then flight tested on a UAS and compared to with wind measurements from a ground weather station. The methods are differentiated by what sensor information is available, as represented in Table 1. This thesis considers formulations from (Rhudy, Gu, Gross, & Chao, 2017) as wind estimation technique.

Table 1 Methods from (Rhudy, Gu, Gross, & Chao, 2017)

	Pitot-static tube	GPS velocity (north and east)	GPS velocity (down)	IMU	Angle of attack and sideslip angle
Method 1	X	X			
Method 2	X	X	X		
Method 3	X	X	X	X	
Method 4	X	X	X	X	X

1.4. Research Objective

The objective of this research effort is to support the proof-of-concept of DAP, through designing novel control laws. These control laws are implemented and evaluated in a simulation environment. As well, a research test-bed is developed using subscale UAS devices of 4m wing span and flying below 500ft to test the control laws.

This thesis document is organized as follows: Chapter 1 presents a literature review of the topics addressed in this thesis. A brief description of the DAP UAS simulation environment is provided in Chapter 2. Chapter 3 presents the architecture of the control laws, as well as simulation results in the form of case studies. Chapter 4 describes the UAS research platform along with results from the flight testing program and wind sensing methodologies. Finally, conclusions and recommendations for future work are provided in Chapter 5.

The research effort presented in this thesis has resulted in the submission for publication:

Nshuti C., Engblom W., Moncayo H., Festa D. (2018). Modeling, Simulation and Flight Testing to Support Proof of a Stratospheric Dual Aircraft Platform Concept. Accepted for presentation at AIAA SciTech Forum, Orlando.

Willems J., Engblom W., Moncayo H., Nshuti C. (2018). Verification, Validation, and Application of Shear Stress Transport Transitional Model to a R/C Aircraft. Accepted for presentation at AIAA SciTech Forum, Orlando.

CHAPTER 2: UAS Simulation Environment

The DAP UAS simulation was developed in MATLAB/Simulink environment to support pilot training, facilitate the development of control laws and provide hardware-in-the-loop (HIL) architecture for further flight testing. In order to simplify the problem, this study replaces the *BOARD* UAS glider by a *TRUCK* model in both the simulation and flight testing. Hence, the dynamics are applied for a glider-truck control system configuration, as shown in Figure 3. For details regarding the establishment of the sailing conditions used for this simulation environment, refer to (Engblom W. , 2014).
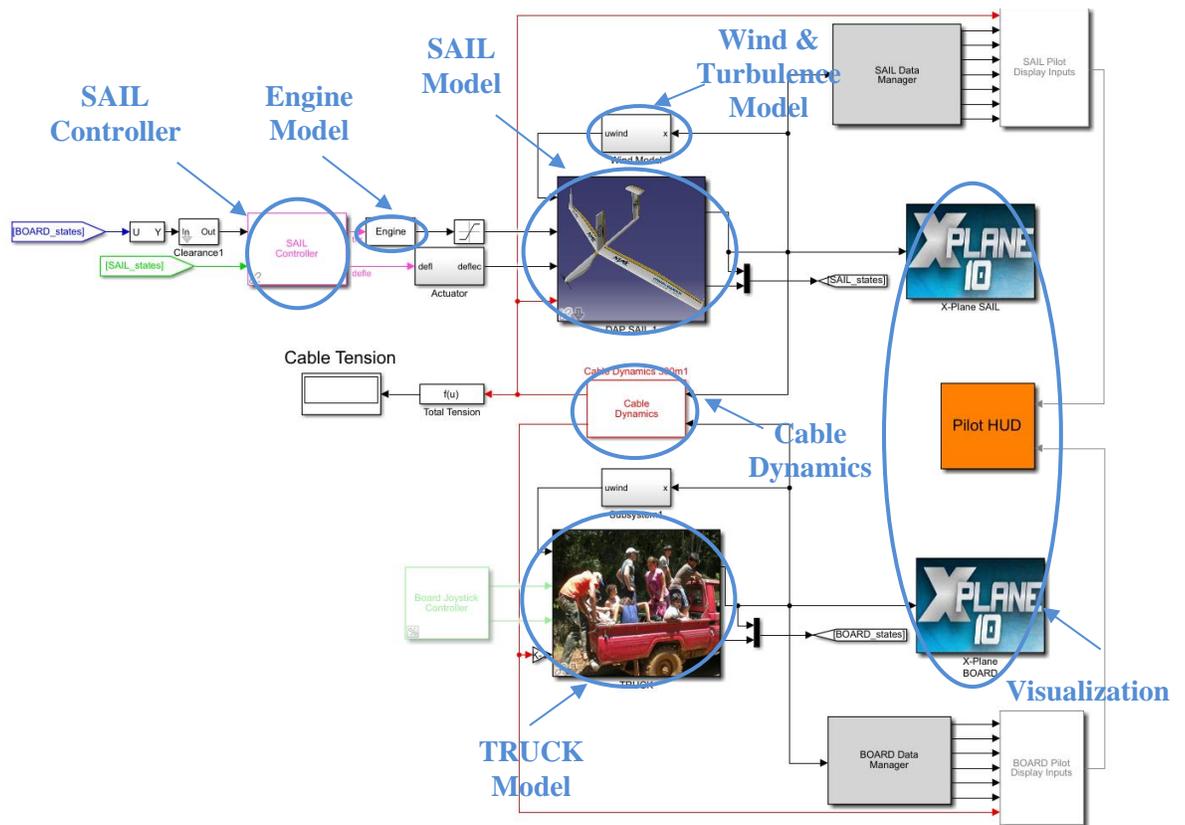
Figure 3 Simulation Environment for DAP (Coulter, Moncayo, & Engblom, 2018a)

The ERAU Flight Simulation Environment provides flexibility and capability to design and test algorithms for DAP flight capabilities. The simulation includes the

following features:

- Non-linear DAP aero model based on VLM-FOIL (details in (Willems, Engblom, Moncayo, & Nshuti, 2018))

- Multi-degree-of-freedom cable dynamics (section 2.2)

- Wind and Turbulence model (section 2.3)

- Actuator model (section 2.4)

- Sail controller (Chapter 3):

  - Formation Flight Controller (FFC)

  - PID controller

  - $\mathcal{L}_1$ adaptive control

- Visualization via X-Plane (section 2.1)

The UAS equations of motion and multi-DOF cable dynamics combined with lookup tables for aerodynamics, are solved using MATLAB/Simulink functions (Engblom W. A., et al., 2016). The simulation is interfaced with X-Plane for a pilot's heads-up display (HUD). This flight software can be used onboard a future flight demonstrator.

2.1. DAP Visualization

For visualization purposes, a plugin for X-Plane was developed. This plugin interfaces the DAP MATLAB/Simulink model with the flight simulator and allows UAS visualization in a high quality virtual environment.

The MATLAB/Simulink model is combined with ERAU FDCRL Plugin for X-Plane which visualizes 3-D motion of the UAS in high quality visual environment demonstration presented in Figure 4. The pilot HUD is interfaced with Flight Gear

software, was implemented at ERAU's FDCRL flight simulator.

Figure 4 ERAU Simulation Environment – X-Plane Interface (left). Pilot-in-the-loop HUD (right).

2.2. Cable Dynamics

A major limitation to sailing performance are the aerodynamic forces on the cable. Because the tension in cable should grow steadily as the aircraft reaches the sailing flight conditions. These forces were modeled using Hoerner's approach to a "cylinder in crossflow" (Engblom W. A., et al., 2016). Thus the dynamics of the cable is modeled as a multi-DOF segments and considers interactions between the two vehicles (Engblom W. A., et al., 2016). The cable is mainly simulated as twenty equal length segmentations. To model the cable dynamics between aircraft, wave speed propagation is determined for the disturbance initiated at one end of the cable and it is dependent on the tension level. High wave speeds are required for the aircraft to "relay" and efficiently operate.

2.3. Wind and Turbulence Model

Wind and turbulence were modeled based on the Dryden wind turbulence model, a mathematical representation accepted by the United States Department of Defense for

some aircraft designs and simulations (Engblom W. A., et al., 2016). The direction of the wind and its magnitude can be set in the simulation by adjusting the "Wind and Turbulence Model", as shown in Figure 3. The turbulence is also adjusted in the same Simulink block. The turbulence has five levels of severity which can be characterized as shown in Table 2. Therefore, a severity of 20 would have semblance to a hurricane.

Table 2 Turbulence Intensity Characterization

Turbulence Severity	Minimum [knots]	Maximum [knots]	Mean [knots]
2	0.104	3.87	1.37
5	0.260	9.72	3.44
10	0.523	19.8	6.97
15	0.789	30.4	10.6
20	1.590	65.3	22.0

2.4. Actuator Model and Configuration

Sailing tethered flight is a highly coupled controls problem. To enter sailing mode, the two gliders must maintain a specific, a near exact attitude as well as the forward, lateral, and vertical spacing in relation to each other. The ailerons, elevators, and rudder must be used to maintain the roll, pitch, and yaw requirements respectively for sailing flight. However, since the lateral, vertical, and forward spacing must also be maintained, a unique solution and aircraft configuration was developed.

Tests performed in flight simulation showed that a fixed "mast" on top the main wing with a maneuverable lateron will enable smoother transitions between *sailing*. These comparison results are presented in Section 3.5. In this context, *sailing* indicates that there is high cable tension (i.e. not slack) while standard cruise implies low cable tension and near level flight. Figure 5 displays the *SAIL* DAP aircraft utilized in flight simulations

including a "mast with lateron", which is an unorthodox feature. For details of the size and specifications of the lateron refer to (Nshuti, Coulter, Festa, Engblom, & Moncayo, 2018).
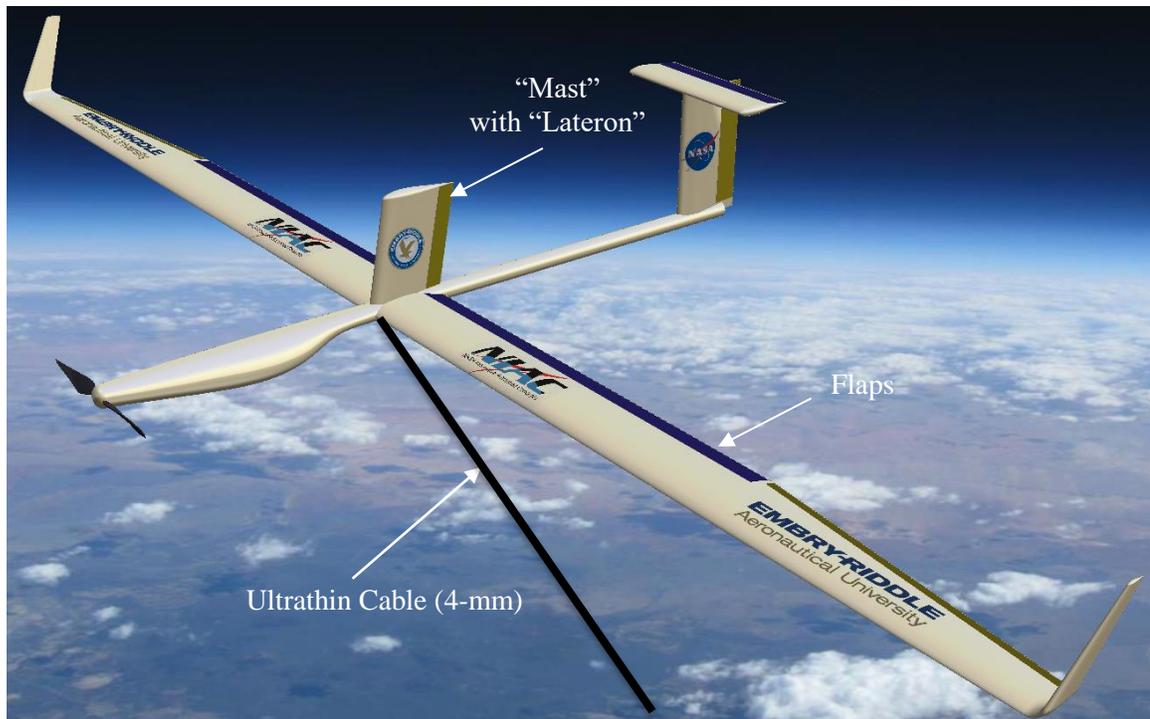
Figure 5 Stratospheric DAP aircraft configuration used for simulation

Another unconventional characteristic of DAP is the function of the flaps. The elevator flight control surface usually controls an aircraft's pitch and therefore the angle of attack. However, the DAP UAS is required to hold altitude and maintain the sailing condition. It was observed in simulation, that there was inadequate amount of elevator authority to accomplish both assignments. Therefore, in order to decouple the sailing condition required for pitch angle but still track the pitch angle required for altitude hold. The flaps are used for altitude hold and can subsequently have both a negative and positive pitching moment. The decoupling of the control law is described in CHAPTER 3.

2.5. Propulsion Study

The gliders do have an electric propulsion system. The propeller blades retract to prevent them from wind-milling when thrust is turned off. In a future study, unconventional system propulsion/turbine system that can extract wind power through varying pitch and twist could be developed for use in the stratosphere. Pipistrel's WATTsUP Prototype is a propeller-driven sport aircraft that has demonstrated this concept.

To initiate a proof-of-concept, for the prototype UAS a propulsion mechanism had to be identified. Three motors were chosen for this investigation: E-flite P25, Hacker A20, Hacker A30-12L, and two electronic speed controllers (ESC) at different amperage were investigated: 70 A and 50 A. Appendix A displays a portion of this investigation with the results of Hacker A30-12L and E-flite P25. Figure 6 shows the thrust stand used for this propulsion investigation, as well as a ground testing stand, nicknamed "iron-bird" was used for testing the UAS in conjunction with the propulsion system before setting up a flight test.
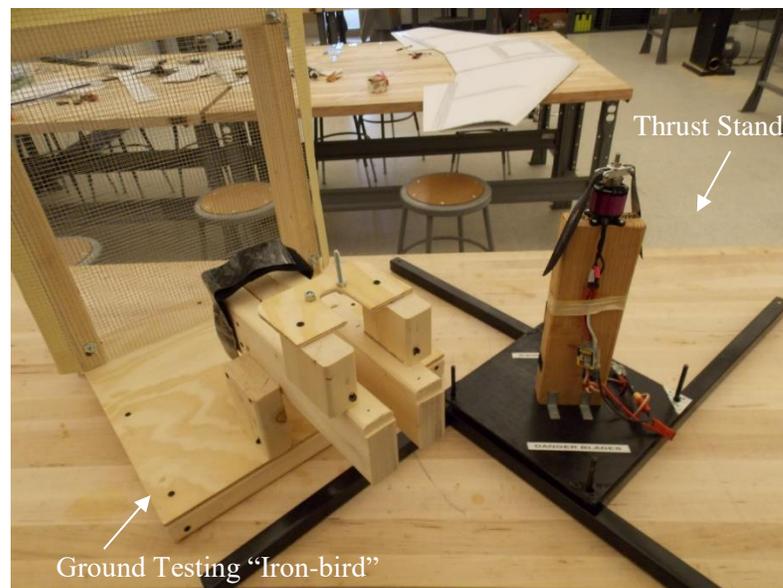
Figure 6 "Iron-bird" for ground testing and thrust stand

It was concluded that a Hacker A30-12L in combination with a 50 A provided sufficient propulsion and minimized engine cuts during flights. Thus the combination is used in subsequent studies.

A dynamic thrust identification was performed to characterize dynamic thrust vs. throttle and airspeed using ERAU's wind tunnel. This involved the propulsion system used in the DAP flight test hardware (described in CHAPTER 4).
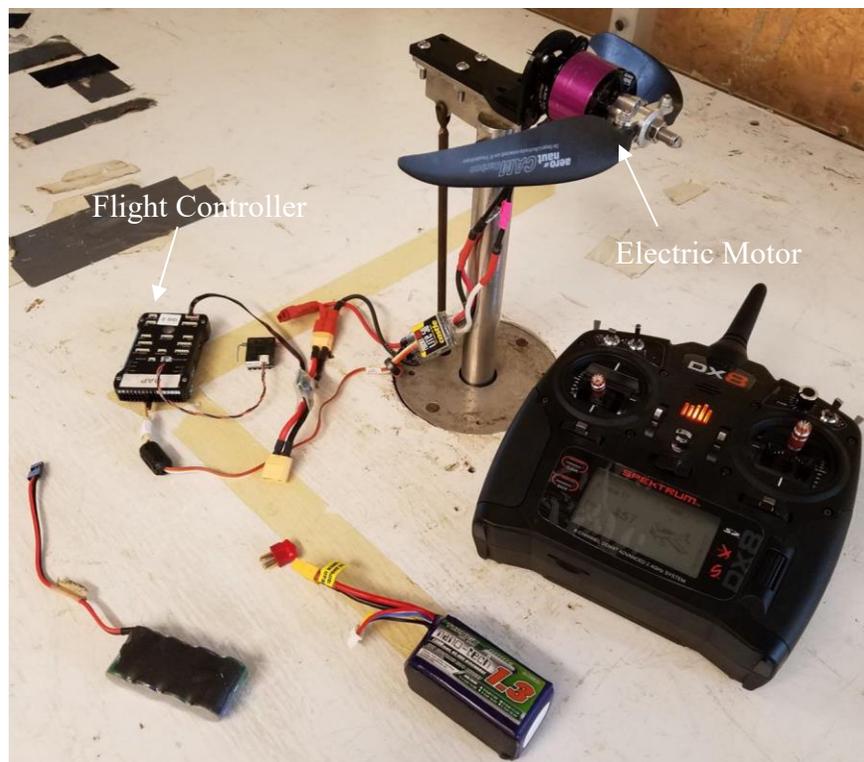
Figure 7 Propulsion Test Hardware Configuration

The test hardware in Figure 7 includes a flight controller that acted as an incremental throttle control in 5% steps. This data will allow for the control subsystem to be refined and tune the cruise condition to the required sailing configuration in a subsequent study.

The results for the propulsion subsystem in the wind tunnel are discussed. Three airspeeds were investigated: 8 m/s, 10 m/s, and 12 m/s. Airspeed was measured using a pitot-static tube and digital pressure indicator attached to the wind tunnel. At each airspeed, the throttle was advanced in 5% increments from 5% up to 100%. To determine the longevity of the main batteries, a sample test was done at 0 m/s. It was found that no performance degradation occurred from 5% up to 70% throttle settings.

The following assumptions were made: 1) ERAU's force balance was functioning properly and providing accurate measurements throughout the duration of the tests. 2) The minor changes (<5%) in air density throughout the testing can be neglected.

Table 3 Thrust Map

	Airspeed		
	8 m/s	10 m/s	12 m/s
Throttle Setting	Thrust (N)		
5%	0.044077	0.090471	-0.181677
10%	0.777222	0.698969	0.336738
15%	1.526279	1.657872	0.942236
20%	2.481146	2.386269	1.695570
25%	3.669767	3.948056	3.009696
30%	5.872451	5.888806	4.229759
35%	7.670615	7.835521	6.372241
40%	9.547777	9.686288	8.158593
45%	11.182499	11.502313	9.816768
50%	13.223281	13.337504	11.370721
55%	15.074752	15.380448	13.478632
60%	16.718749	16.593650	14.503518
65%	17.617166	17.145903	15.429462
70%	17.551094	17.193996	15.368132
75%	17.752413	16.944363	15.580210
80%	18.697698	17.688311	16.785732
85%	18.640252	17.317051	16.363929
90%	18.329143	17.174826	16.520168
95%	17.905710	16.788212	16.022416
100%	17.905710	15.107509	16.022416
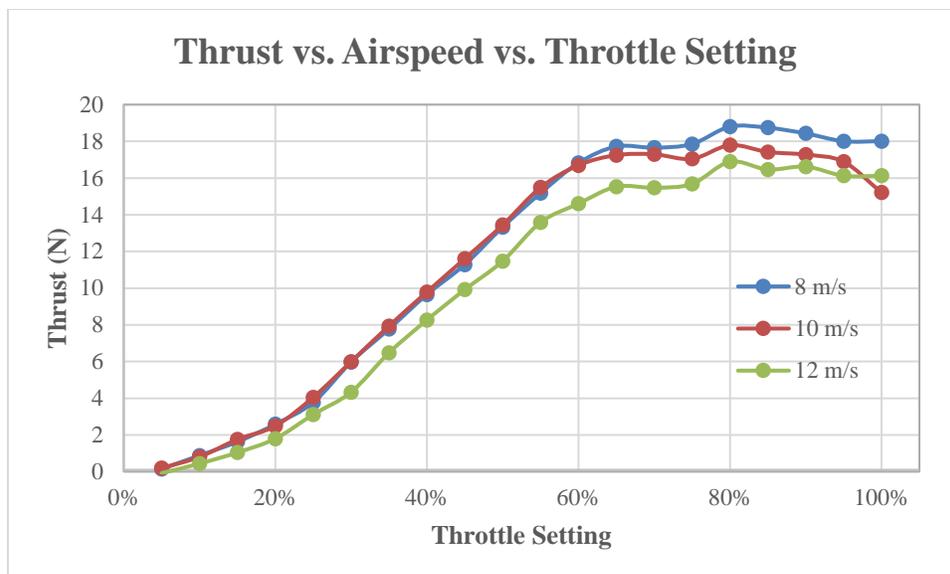
Figure 8 Thrust Map

These results can further be integrated into the simulation model to enhance the thrust model.

CHAPTER 3: Control Laws Architecture

In this thesis, the proposed control laws for autonomous flight are based on inner-outer loop control architecture as shown in Figure 9. There are three main components: formation geometry, outer loop and inner loop, which are subsequently described:
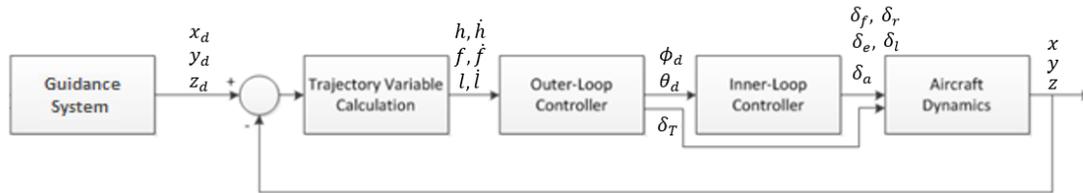
Figure 9 General Architecture of Control Laws

3.1. Trajectory Calculation

A formation flight based controller is implemented on the *SAIL* to track the *BOARD*'s trajectory (i.e. guidance system in Figure 9). The trajectory geometry is based on a Formation Flight Controller (FFC) problem designed based on the analogy of leader-wingman formation. It is developed utilizing the geometry in the reference frame of the follower aircraft and its location in inertial space with respect to the leader. The geometry of the trajectory problem can be separated into two components: a horizontal plane tracking problem and vertical plane tracking problem.

For horizontal, the pre-determined formation geometric parameters are the lateral clearance l_c and forward clearance f_c (see Figure 10). The lateral distance error l and forward distance error f can be calculated from positions and velocities using the following relationships:

$$l = \frac{V_{Vy}(x_V - x) - V_{Vx}(y_V - y)}{V_{Vxy}} - l_c \tag{3.1}$$

$$f = \frac{V_{Vy}(y_V - y) - V_{Vx}(x_V - x)}{V_{Vxy}} - f_c \qquad (3.2)$$

where,

l is the lateral error between the leader and follower

f is the forward error between the leader and follower

h is the vertical error between the leader and follower

V_{Vn} is the velocity of the leader projected along the nth -axis

n_V is the nth -axis position of the leader

n is the nth -axis position of the follower
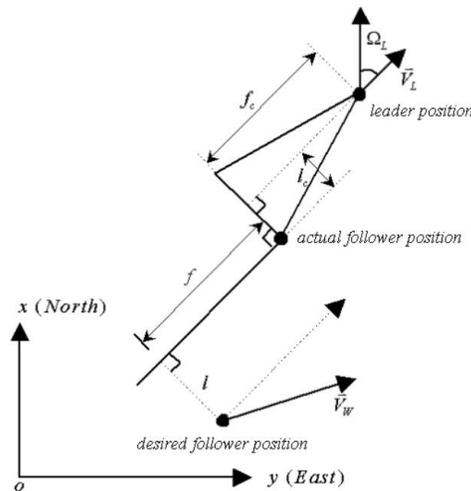
Figure 10 Trajectory Tracking Flight Geometry (Campa, Napolitano, Seanor, & Perhinschi, 2004)

In equations 3.1 and 3.2, $V_{Vxy} = \sqrt{V_{Vx}^2 + V_{Vy}^2}$ is the projection of the leader's velocity onto the $x - y$ plane. Therefore, the wingman's lateral and forward speed are defined as the time derivatives of the lateral and forward distance respectively and are required for the purpose formation control which can be calculated as:

$$\dot{l} = \frac{V_{Vx}V_y - V_{Vy}V_x}{V_{Vxy}} + \Omega_V f \tag{3.3}$$

$$\dot{f} = V_{Vxy} - \frac{V_{Vx}V_x - V_{Vy}V_y}{V_{Vxy}} + \Omega_V l \tag{3.4}$$

where $\Omega_V = \frac{q_V \sin \phi_V + r_V \cos \phi_V}{\cos \phi_V}$ is the trajectory-induced angular velocity in the $x -$

y plane (around the vertical axis). This parameter is considered zero in this study.

Note that positions and velocities for both the leader and follower can be represented along the x and y axes of the earth-fixed reference frame and are measured by the GPS on-board the aircraft (Campa, Napolitano, Seanor, & Perhinschi, 2004). Thus, equation 3.5 represents a transformation matrix that rotates the error to a reference frame orientated as the leader's velocity.

$$\begin{bmatrix} l \\ f \end{bmatrix} = \begin{bmatrix} \sin(\chi_V) & -\cos(\chi_V) \\ \cos(\chi_V) & \sin(\chi_V) \end{bmatrix} \begin{bmatrix} x_V - x \\ y_V - y \end{bmatrix} - \begin{bmatrix} l_c \\ f_c \end{bmatrix} \tag{3.5}$$

where χ_V is the azimuth angle which is given by:

$$\cos(\chi_V) = \frac{V_{Vx}}{\sqrt{V_{Vx}^2 + V_{Vy}^2}} \quad \text{and} \quad \sin(\chi_V) = \frac{V_{Vy}}{\sqrt{V_{Vx}^2 + V_{Vy}^2}} \tag{3.6}$$

For the vertical geometry, the vertical distance error h, can be simply calculated as:

$$h = z_V - z \tag{3.7}$$

where the time derivative is given by:

$$\dot{h} = V_{zV} - V_z \tag{3.8}$$

3.2. Outer Loop Controller

The outer loop controller relates the formation tracking variables to attitude and throttle commands, that is the compensation for lateral, forward and vertical errors to produce bank angle, throttle and pitch angle, respectively using the following differential equations:

$$\phi_d = K_{\dot{l}}\dot{l} + K_l l \tag{3.9}$$

$$\delta_T = K_{\dot{f}}\dot{f} + K_f f \tag{3.10}$$

$$\theta_d = K_{\dot{h}}\dot{h} + K_h h \tag{3.11}$$

3.3. Inner Loop Controller

In order to achieve the commanded bank angle and pitch angle produced by the outer loop, the inner controller generates control surface deflections required given by ailerons, elevator, flap, rudder and lateron commands (see Figure 11). As well as track sailing conditions which were previously generated by a sail optimization algorithm described in (Engblom W. , 2014). For development of control laws in the inner loop, two approaches were involved in this study: a linear controller (i.e. PID) and an adaptive controller ($\mathcal{Z}_l$).
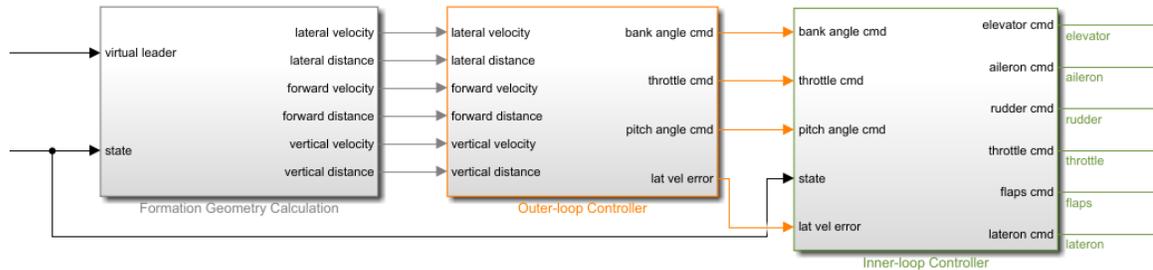
Figure 11 Control System

3.3.1. Proportional Integral Derivative Controller

Proportional Integral Derivative (PID) controller is implemented to achieve the desired reference angles and to counter the effects of high rates. The longitudinal controller generates flap deflection tracks a desired pitch angle as commanded by the outer controller (as shown in equation 3.12 discrete form):

$$\delta_f = \left(k_{P\theta} + \frac{k_{I\theta}}{z-1} + k_{D\theta}\frac{z-1}{z} \right)(\theta_d - \theta) \tag{3.12}$$

while the elevator deflection equation uses pitch rate for stabilization and tracks a pre-determined sail/board pitch angle:

$$\delta_e = \left(k_{P\theta} + \frac{k_{I\theta}}{z-1} + k_{D\theta}\frac{z-1}{z}\right)(\theta_{sail} - \theta) - k_{Pq}q \qquad (3.13)$$

the lateral controller generates aileron and rudder deflections:

$$\delta_a = \left(k_{Pa\phi} + \frac{k_{Ia\phi}}{z-1} + k_{Da\phi}\frac{z-1}{z}\right)(\phi_{sail} - \phi) - k_{Pap}p - k_{Par}r \qquad (3.14)$$

the rudder deflection equation uses a pre-determined sail/board yaw angle and yaw rate:

$$\delta_r = \left(k_{Pr\psi} + \frac{k_{Ir\phi}}{z-1} + k_{Dr\psi}\frac{z-1}{z}\right)(\psi_{sail} - \psi) - k_{Prp}p - k_{Prr}r \qquad (3.15)$$

To obtain the lateron deflection command PID control is implemented on the lateral velocity error.

$$\delta_l = \left(k_{Pl\phi} + \frac{k_{Il\phi}}{z-1} + k_{Dl\phi}\frac{z-1}{z}\right)(l) - k_{Plp}p - k_{Plr}r \qquad (3.16)$$

Where,

δ_n is the nth control surface: flap, aileron and rudder.

k_{Pm} is the mth proportional gain.

k_{Im} is the mth integral gain.

k_{Dm} is the mth derivative gain.

θ, ϕ, ψ Euler angles, subscript *d* and *sail* indicates the desired state and sail condition, respectively.

3.3.2. $\mathcal{L}_1$ Adaptive Output Feedback Controller

This section presents the $\mathcal{L}_1$ adaptive output feedback controller and its application to DAP. The $\mathcal{L}_1$ adaptive control architecture was first presented in (Cao & Hovakimyan, 2007a) using a state feedback approach for systems in the presence of constant unknown

parameters. (Cao & Hovakimyan, 2008a) derived the guaranteed time-delay margin of $\mathcal{L}_1$ adaptive control architecture. Later the scheme was extended to output feedback for a class of reference systems with strictly positive real (SPR) transfer function (Cao & Hovakimyan, 2008b). In (Cao & Hovakimyan, 2007b) and (Cao & Hovakimyan, 2007c) both report an expansion to nonlinear time-varying systems in the presence of additive and multiplicative un-modeled dynamics. An output feedback extension is presented in (Cao & Hovakimyan, 2009) for systems of unknown relative dimension in the presence of time-varying uncertainties without imposing an SPR-type requirement on the rate of their variation. (Cao & Hovakimyan, 2009) was also first to introduce a fast estimation technique based on a piecewise continuous adaptive law. It is accompanied with a low-pass-filtered control signal that permits the attainment of arbitrary close tracking of the output and input signals of the reference system. It is this particular architecture that is employed in this study to address the control challenge of DAP. Because the piecewise-constant adaptive law allows the obtainment of performance bounds between the $\mathcal{L}_1$ reference system and the closed-loop $\mathcal{L}_1$ adaptive system. Consequently, these bounds can be considered arbitrarily small by decreasing the sampling rate of the adaptation law, such that it can be set to the available sampling rate of the central processing unit (CPU). The $\mathcal{L}_1$ adaptive output feedback control architecture is presented in Figure 12 and a description is given based on formulations found in (Hovakimyan & Cao, 2010).

Problem Formulation

Consider the following single-input single-output (SISO) system:

$$y(s) = A(s)u(s) + d(s) \tag{3.17}$$

where $u(t) \in \mathbb{R}$ is the input; $y(t) \in \mathbb{R}$ is the system output; $A(s)$ is a strictly-proper unknown transfer function of unknown relative degree n_r, for which only a known lower bound $1 < d_r \leq n_r$ is available; $d(s)$ is the Laplace transform of the time-varying uncertainties and disturbances $d(t) = f(t, y(t))$, while $f : \mathbb{R} \times \mathbb{R} \to \mathbb{R}$ is an unknown map, subject to the following assumption:

Assumption 3.1 (Global Lipschitz continuity and boundedness). There exist constants $L > 0$ and $L_0 > 0$ such that

$$|f(t, y_1) - f(t, y_2)| \leq L|y_1 - y_2|$$

$$|f(t, y)| \leq L|y| + L_0$$

hold uniformly in $t \geq 0$, where the numbers L and L_0 can be arbitrarily large.

Let $r(t) \in \mathbb{R}$ be a given bounded continuous reference input signal. The control objective is to design an adaptive output-feedback controller $u(t)$ such that the system output $y(t)$ tracks the reference input $r(t)$ following a desired reference model $M(s)$, where $M(s)$ is a minimum phase stable transfer function of relative degree $d_r > 1$.

$$y_{id}(s) = M(s)r(s) \tag{3.18}$$

Definitions and $\mathcal{L}_l$-norm Stability Conditions

We start by rewriting the system in 3.17 as:

$$y(s) = M(s)(u(s) + \sigma(s)), \quad y(0) = 0 \tag{3.19}$$

$$\sigma(s) = \frac{(A(s) - M(s))u(s) + A(s)d(s)}{M(s)} \tag{3.20}$$

Let $(A_m \in \mathbb{R}^{N \times N}, b_m \in \mathbb{R}^N, c_m^T \in \mathbb{R}^N)$ be a minimal realization of $M(s)$. Hence, (A_m, b_m, c_m^T) is controllable and observable. Thus the system in 3.19 can be written as:

$$\dot{x}(t) = A_m x(t) + b_m(u(t) + \sigma(t))$$

$$y(t) = c_m^T x(t), \quad x(0) = x_0 = 0 \tag{3.21}$$

The design of the $\mathcal{L}_1$ adaptive controller proceeds by considering a stable low-pass filter $C(s)$ of relative degree greater or equal to d_r, with unit dc-gain $C(0) = 1$. Further the selection of $C(s)$ and $M(s)$ must ensure that

$$H(s) \triangleq \frac{A(s)M(s)}{C(s)A(s)+(1-C(s))M(s)} \tag{3.22}$$

is stable, and the following $\mathcal{L}_1$-norm condition holds:

$$\|G(s)\|_{\mathcal{L}_1} L < 1 \tag{3.23}$$

where $G(s) \triangleq H(s)(1 - C(s))$.

Further, since A_m is Hurwitz, there exists $P = P^T > 0$ that satisfies the algebraic Lyapunov equation

$$A_m^T P + PA_m = -Q, \text{ for arbitrary } Q = Q^T > 0.$$

From the properties of P, it follows that there exists nonsingular $\sqrt{P}$ such that

$$P = (\sqrt{P})^T \sqrt{P}.$$

Given the vector $c_m^T(\sqrt{P})^{-1}$, let $D \in \mathbb{R}^{(n-1)\times n}$ be a matrix that contains the null-space of $c_m^T(\sqrt{P})^{-1}$, i.e.,

$$D(c_m^T(\sqrt{P})^{-1})^T = 0 \tag{3.24}$$

and further let

$$\Lambda \triangleq \begin{bmatrix} c_m^T \\ D\sqrt{P} \end{bmatrix} \tag{3.25}$$

From the definition of the null space, it follows that

$$\Lambda (\sqrt{P})^{-1} \triangleq \begin{bmatrix} c_m^T(\sqrt{P})^{-1} \\ D \end{bmatrix} \tag{3.26}$$

is full rank, and hence Λ^{-1} exists.

Define $T_s \in \mathbb{R}^+$ as an arbitrary positive constant, which can be associated with the sampling rate of the available CPU. Further, let $\phi(T_s) \in \mathbb{R}^{n \times n}$ be given by

$$\phi(T_s) \triangleq \int_0^{T_s} e^{\wedge A_m \wedge^{-1}(T_s - \tau)} \wedge d\tau \qquad (3.27)$$

Next, let

$$H_0(s) \triangleq \frac{A(s)}{C(s)A(s) + (1 - C(s))M(s)}, \qquad H_1(s) \triangleq \frac{\big(A(s) - M(s)\big)F(s)}{C(s)A(s) + \big(1 - C(s)\big)M(s)}$$

$$H_2(s) \triangleq \frac{H(s)C(s)}{M(s)}, \qquad H_3(s) \triangleq \frac{M(s)C(s)}{C(s)A(s) + (1 - C(s))M(s)} \qquad (3.28)$$

Also, let

$$\Delta \triangleq \|H_1(s)\|_{\mathcal{L}_1} \|r\|_{\mathcal{L}_\infty} + \|H_0(s)\|_{\mathcal{L}_1}(L\rho_r + L_0)$$

$$+ \left(\left\| \frac{H_1(s)}{M(s)} \right\| + \|H_0(s)\|_{\mathcal{L}_1} \frac{\|H_2(s)\|_{\mathcal{L}_1}}{1 - \|G(s)\|_{\mathcal{L}_1}L} L \right) \bar{\gamma}_0 \qquad (3.29)$$

where $\bar{\gamma}_0 \in \mathbb{R}^+$ is an arbitrary constant.

Let

$$1_1^T e^{\wedge A_m \wedge^{-1}t} = [\eta_1(t), \eta_2^T(t)] \qquad (3.30)$$

where $\mathbf{1}_1 = [1, 0, \ldots, 0]^T \in \mathbb{R}^n$, $\eta_1(t) \in \mathbb{R}$ and $\eta_2(t) \in \mathbb{R}^{n-1}$ contain the first and the 2-to-n elements of the row vector $1_1^T e^{\wedge A_m \wedge^{-1}t}$. Then define

$$\kappa(T_s) \triangleq \int_0^{T_s} \left| \mathbf{1}_1^T \wedge e^{\wedge A_m \wedge^{-1}(T_s - \tau)} b_m \right| d\tau \qquad (3.31)$$

Also, let $\varsigma(T_s)$ be defined as

$$\varsigma(T_s) \triangleq \|\eta_2(T_s)\| \sqrt{\frac{\alpha}{\lambda_{max}(P_2)}} + \kappa(T_s)\Delta \qquad (3.32)$$

$$\alpha \triangleq \lambda_{max}(\wedge^{-T} P \wedge^{-1}) \left(\frac{2\Delta \|\wedge^{-T} P b_m\|}{\lambda_{min}(\wedge^{-T} Q \wedge^{-1})} \right)^2 \qquad (3.33)$$

Next, the following functions are introduced

$$\beta_1(T_s) \triangleq \max_{t \in |0, \ T_s|} |\eta_1(t)|, \qquad\qquad \beta_2(T_s) \triangleq \max_{t \in |0, \ T_s|} \|\eta_2(t)\| \qquad (3.34)$$

and also

$$\beta_3(T_s) \triangleq \max_{t \in |0, \ T_s|} \eta_3(t), \qquad\qquad \beta_4(T_s) \triangleq \max_{t \in |0, \ T_s|} \eta_4(t) \qquad (3.35)$$

where

$$\eta_3(t) \triangleq \int_0^t \left| \mathbf{1}_1^T e^{\wedge A_m \wedge^{-1}(t-\tau)} \wedge \varphi^{-1}(T_s) e^{\wedge A_m \wedge^{-1} T_s} \mathbf{1}_1 \right| d\tau \qquad (3.36)$$

$$\eta_4(t) \triangleq \int_0^{T_s} \left| \mathbf{1}_1^T e^{\wedge A_m \wedge^{-1}(T_s-\tau)} \wedge b_m \right| d\tau \qquad (3.37)$$

The following lemma introduces a positive definite matrix P_2 and a positive constant p_1, which can be computed from the detailed proof in (Hovakimyan & Cao, 2010).

Lemma 3.1. For arbitrary $\xi \triangleq [y \ z^T]^T \in \mathbb{R}^n$, where $z \in \mathbb{R}^{n-1}$, there exist $p_1 \in \mathbb{R}^+$ and positive definite $P_2 \in \mathbb{R}^{(n-1) \times (n-1)}$ such that

$$\xi^T (\wedge^{-1})^T P \wedge^{-1} \xi = p_1 y^2 + z^T P_2 z \qquad (3.38)$$

Finally, define

$$\gamma_0(T_s) \triangleq \beta_1(T_s)\varsigma(T_s) + \beta_2(T_s)\sqrt{\frac{\alpha}{\lambda_{max}(P_2)}} + \beta_3(T_s)\varsigma(T_s) + \beta_4(T_s)\Delta \qquad (3.39)$$

$\mathcal{L}_1$ Adaptive Control Architecture

The $\mathcal{L}_1$ adaptive controller consists of an output predictor, an adaptation law and the control law, which includes a low-pass filter $C(s)$ that combined with the choice of $M(s)$ needs to satisfy the $\mathcal{L}_1$-norm stability condition (3.23). The elements of $\mathcal{L}_1$ adaptive controller are introduced next.

Output Predictor

We consider the following output-predictor:

$$\dot{\hat{x}}(t) = A_m\hat{x}(t) + b_m u(t) + \hat{\sigma}(t), \quad \hat{x}(0) = 0$$

$$\hat{y}(t) = c_m^T\hat{x}(t) \tag{3.40}$$

where $\hat{\sigma}(t) \in \mathbb{R}^n$ is the vector of adaptive parameters. Notice that while $\sigma(t) \in \mathbb{R}$

in (3.21) is matched, the uncertainty estimation $\hat{\sigma}(t) \in \mathbb{R}^n$ in (3.40) is unmatched.
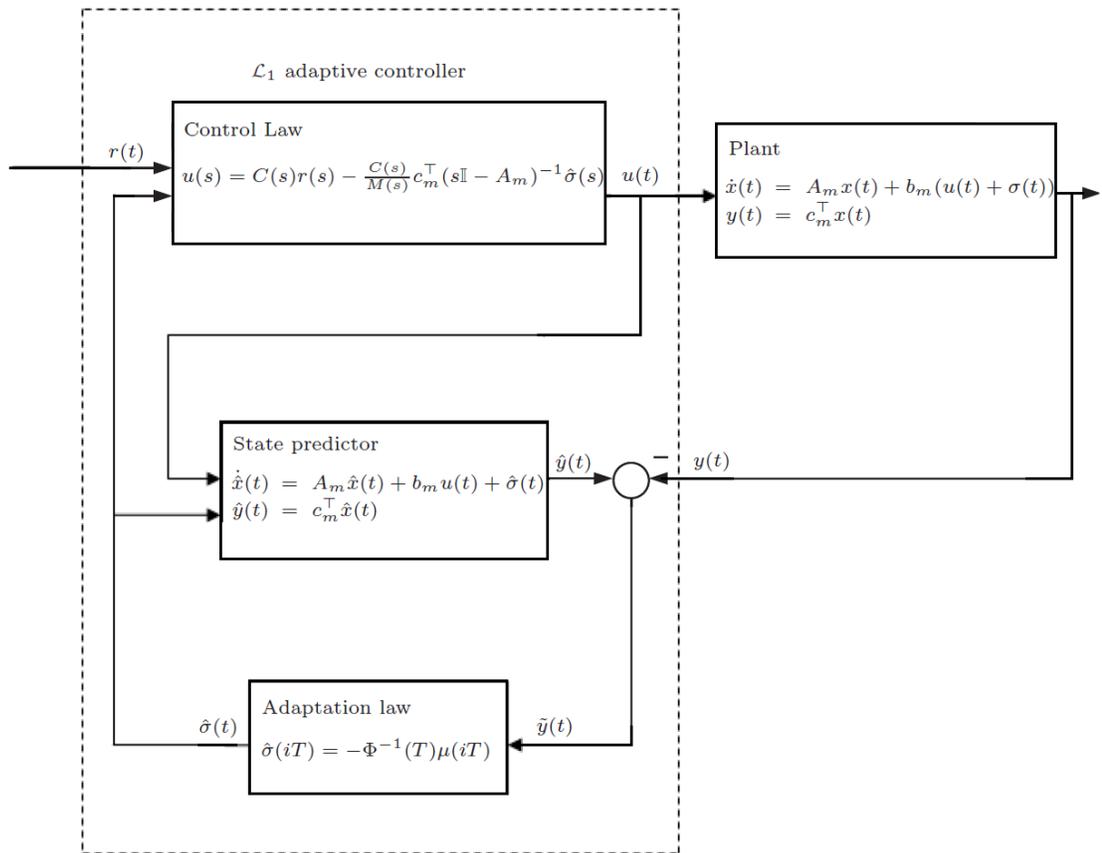
Figure 12 Block diagram of the closed-loop $\mathcal{L}_1$ adaptive controller

Adaptation Laws

Letting $\tilde{y}(t) \triangleq \hat{y}(t) - y(t)$, the update law for $\hat{\sigma}(t)$ is given by

$$\hat{\sigma}(t) = \hat{\sigma}(iT_s), \quad t \in [iT_s, (i+1)T_s)$$

$$\hat{\sigma}(iT_s) = -\phi^{-1}(T_s)\mu(iT_s), \quad i = 0, 1, 2, \dots \tag{3.41}$$

where $\phi(T_s)$ was defined in (3.27) and

$$\mu(iT_s) = \phi^{-1}(T_s)e^{\wedge A_m \wedge^{-1}T_s}\mathbf{1}_1 = (e^{A_m T_s} - \mathbb{I})^{-1}A_m e^{A_m T_s}\wedge^{-1}\mathbf{1}_1 \tag{3.42}$$

Control Law

The control signal is defined as follows:

$$u(s) = C(s)r(s) - \frac{C(s)}{c_m^T(s\mathbb{I}-A_m)^{-1}b_m} c_m^T(s\mathbb{I} - A_m)^{-1}\hat{\sigma}(s) \qquad (3.43)$$

where $C(s)$ was first introduced in (3.22). The $\mathcal{L}_1$ adaptive controller consists of (3.40), (3.41) and (3.42), subject to the $\mathcal{L}_1$-norm condition in (3.23). The block diagram of the closed-loop $\mathcal{L}_1$ adaptive control system is given in Figure 12.

Theorem 3.1

$$\lim_{T \to 0}\left(\|\tilde{y}\|_{\mathcal{L}_\infty}\right) = 0$$

$$\lim_{T \to 0}\left(\|y - y_{ref}\|_{\mathcal{L}_\infty}\right) = 0$$

$$\lim_{T \to 0}\left(\|u - u_{ref}\|_{\mathcal{L}_\infty}\right) = 0$$

The result in this theorem follows directly from [Theorem 1 (Cao & Hovakimyan, 2008c)] and [Lemma 4.2.3 (Hovakimyan & Cao, 2010)].

3.3.3. $\mathcal{L}_1$ Adaptive Control Law for DAP

In order to achieve the control objective for DAP, we need to design an adaptive output feedback controller $u(t)$ such that in the presence of disturbances and uncertainties the system output $y(t)$ tracks the reference input $r(t)$ with satisfactory performance. This can be done by choosing a minimum-phase, strictly proper and stable transfer function $M(s)$ and designing an adaptive control law to achieve $y(s) \approx M(s)r(s)$. The first step is to guarantee stability of the closed-loop system. Because Theorem 1 infers that the output of the closed-loop system tracks that of the closed-loop reference system arbitrarily strictly

for all $t > 0$. Therefore the first step in designing an $\mathcal{L}_1$ adaptive output feedback controller is to define $C(s)$ and $M(s)$ that satisfy the conditions given in equation (3.22) and (3.23).

Note that longitudinal and lateral-dynamics are assumed to be decoupled in this study. Given a transfer function:

$$M_n(s) = \frac{\omega_n}{s^2 + 2\zeta_n\omega_n s + \omega_n^2} \tag{3.44}$$

where ω_n is the natural frequency and ζ_n damping ratio, i.e. subscript n is subjective to the state. Given the transfer function in (3.44) the following equations can be derived:

$$\frac{Output(s)}{Input(s)} = \frac{Y(s)}{U(s)} = \frac{\omega_n}{s^2 + 2\zeta_n\omega_n s + \omega_n^2} \tag{3.45}$$

$$\frac{Y(s)/\omega_n}{U(s)} = \frac{1}{s^2 + 2\zeta_n\omega_n s + \omega_n^2} \tag{3.46}$$

If $\frac{Y(s)}{\omega_n} = X(s)$ and $y(t) = \omega_n^2 x(t)$ then:

$$\frac{X(s)}{U(s)} = \frac{1}{s^2 + 2\zeta_n\omega_n s + \omega_n^2} \tag{3.47}$$

thus,

$$X(s)[s^2 + 2\zeta_n\omega_n s + \omega_n^2] = U(s) \tag{3.48}$$

Taking the inverse Laplace, generates:

$$\ddot{x}(t) + 2\zeta_n\omega_n \dot{x}(t) + x(t)\omega_n^2 = u(t) \tag{3.49}$$

This provides the state space equation as:

$x_1 = x$

$\dot{x}_1 = x_2$

$x_2 = \dot{x} = \dot{x}_1$

$$\dot{x}_2 = \ddot{x} = u(t) - 2\zeta_n\omega_n x_2 - x_1\omega_n^2$$

$$\begin{bmatrix} \dot{x}_1 \\ \dot{x}_2 \end{bmatrix} = \begin{bmatrix} 0 & 1 \\ -\omega_n^2 & -2\zeta_n\omega_n \end{bmatrix} \begin{bmatrix} x_1 \\ x_2 \end{bmatrix} + \begin{bmatrix} 0 \\ 1 \end{bmatrix} u(t)$$

and

$$y(t) = \omega_n^2 x(t) = \omega_n^2 x_1(t) = [\omega_n^2 \quad 0] \begin{bmatrix} x_1(t) \\ x_2(t) \end{bmatrix}$$

$$y(t) = [\omega_n^2 \quad 0] \begin{bmatrix} x_1 \\ x_2 \end{bmatrix}$$

Therefore;

$$C = [\omega_n^2 \quad 0]$$

The **low-pass filter** can be expressed as:

$$C_n(s) = \frac{\omega_{lp}^2}{s^2 + 2\zeta_{lp}\omega_{lp}s + \omega_{lp}^2} \tag{3.50}$$

where ω_{lp} and ζ_{lp} are the natural frequency and damping ratio of the filter, respectively.

The **sample time** was set to

$$T = \frac{1}{600} s$$

3.4. Performance Analysis

In order to assess the robustness of the designed adaptive controller and conventional PID controller, several case studies were investigated at nominal sailing conditions and different flight scenarios. The performance metrics used are inclusive of the sailing and formation flight tracking, control activity and actuation workload. In this context, sailing is achieved when there is no propulsion while holding altitude and ground speed, thus cruising. Additionally, sailing is demonstrated when the UAS is ahead of the

Truck (in x-direction), maintaining a lateral spacing between itself and the Truck, and holding specific distance above the Truck (which is the same as cable length). These combinations will ensure a taut cable. The sailing conditions established for the following case studies were retrieved from the sailing algorithm at a wind profile of 6 knots and 90°. These conditions are provided in Appendix B.

The total performance index (PI) is based on the ability to maintain UAS sailing conditions with little to no thrust. Therefore, the performance of the controller can be defined by two main criteria: the first criterion is based on the UAS' ability to maintain formation flight conditions. The second criterion, assesses the controller's ability to maintain sailing conditions with minimum control surface actuation and minimal to no saturation. These can be formulated as in (Wilburn, Perhinschi, Moncayo, Karas, & Wilburn, 2013) using trajectory tracking indices and control activity indices.

3.4.1. Trajectory Tracking Indices

The *SAIL* UAS should track the *BOARD* (i.e. truck in this study) with as little error as possible. This performance is evaluated by the maximum and mean absolute error, and standard deviation of the tracking error in the *XY*-plane along the Z direction in 3D physical space. Thus there is a total of nine indices. The beginning 3 tracking errors are defined as:

XY-plane tracking error:

$$e_{XY}(t) = \sqrt{[x_c(t) - x(t)]^2 + [y_c(t) - y(t)]^2} \tag{3.51}$$

vertical Z direction tracking error:

$$e_Z(t) = |z_c(t) - z(t)| \tag{3.52}$$

combination of XYZ tracking error:

$$e_{XYZ}(t) = \sqrt{[x_c(t) - x(t)]^2 + [y_c(t) - y(t)]^2 + [z_c(t) - z(t)]^2} \qquad (3.53)$$

where x, y and z are the actual positions of the *SAIL* UAS while the subscript c are the commanded positions from the trajectory or *BOARD* UAS. For a pre-determined time or total simulation time T, the 9 trajectory tracking-related indices are defined as:

Average tracking error:

$$\bar{e}_{XY} = mean(|e_{XY}(t)|) \qquad (3.54)$$

$$\bar{e}_Z = mean(|e_Z(t)|) \qquad (3.55)$$

$$\bar{e}_{XYZ} = mean(|e_{XYZ}(t)|) \qquad (3.56)$$

Maximum tracking error:

$$e_{maxXY} = max(|e_{XY}(t)|) \qquad (3.57)$$

$$e_{maxZ} = max(|e_Z(t)|) \qquad (3.58)$$

$$e_{maxXYZ} = max(|e_{XYZ}(t)|) \qquad (3.59)$$

Standard deviation of the tracking error:

$$\hat{e}_{XY} = STD(e_{XY}(t)) \qquad (3.60)$$

$$\hat{e}_Z = STD(e_Z(t)) \qquad (3.61)$$

$$\hat{e}_{XYZ} = STD(e_{XYZ}(t)) \qquad (3.62)$$

The trajectory tracking specific performance vector, PV_{TT} is defined as:

$$PV_{TT} = [tt_i | i = 1,2...,9] = [\bar{e}_{XY}\bar{e}_Z\bar{e}_{XYZ}e_{maxXY}e_{maxZ}e_{maxXYZ}\hat{e}_{XY}\hat{e}_Z\hat{e}_{XYZ}]^T \qquad (3.63)$$

3.4.2. Control Activity Indices

The control action indices evaluate performance in terms of the controller's capacity to maintain the trajectory and sailing condition with minimum control surface effort and minimum to no saturation of the control surfaces. With respect to these desired

behaviors, two parameters are required: integral of the absolute value of the rate of change of actuator deflection and percentage of actuator saturation. Since there are 6 actuators, there is are indices: flaps δ_f, elevator δ_e, ailerons δ_a, rudder δ_r, lateron δ_l and throttle δ_t . The control activity is defined as in (Wilburn, Perhinschi, Moncayo, Karas, & Wilburn, 2013):

$$I\dot{\delta}_f = \frac{1}{T}\int_0^T |\dot{\delta}_f(t)|\, dt \tag{3.64}$$

$$I\dot{\delta}_e = \frac{1}{T}\int_0^T |\dot{\delta}_e(t)|\, dt \tag{3.65}$$

$$I\dot{\delta}_a = \frac{1}{T}\int_0^T |\dot{\delta}_a(t)|\, dt \tag{3.66}$$

$$I\dot{\delta}_r = \frac{1}{T}\int_0^T |\dot{\delta}_r(t)|\, dt \tag{3.67}$$

$$I\dot{\delta}_l = \frac{1}{T}\int_0^T |\dot{\delta}_l(t)|\, dt \tag{3.68}$$

$$I\dot{\delta}_t = \frac{1}{T}\int_0^T |\dot{\delta}_t(t)|\, dt \tag{3.69}$$

The flap saturation index with symmetry extreme deflections:

$$S_{\delta_f} = \frac{100}{T}\int_0^T \tilde{\delta}_f(t)\, dt \tag{3.70}$$

where

$$\tilde{\delta}_f(t) = \begin{cases} 0 & for\ \delta_f < \delta_{f\ max} \\ 1 & for\ \delta_f \geq \delta_{f\ max} \end{cases} \tag{3.71}$$

For the elevator saturation indices assume non-symmetric negative and positive extreme deflections can be defined as:

$$S_{\delta_e} = \frac{100}{T}\int_0^T (\tilde{\delta}_{e1}(t) + \tilde{\delta}_{e2}(t))dt \tag{3.72}$$

where

$$\tilde{\delta}_{e1}(t) = \begin{cases} 0 & for\ \delta_e < \delta_{e\ max} \\ 1 & for\ \delta_e \geq \delta_{e\ max} \end{cases} \quad and \quad \tilde{\delta}_{e2}(t) = \begin{cases} 0 & for\ \delta_e > \delta_{e\ min} \\ 1 & for\ \delta_e \leq \delta_{e\ min} \end{cases} \tag{3.73}$$

The aileron saturation index with symmetry extreme deflections:

$$S_{\delta_a} = \frac{100}{T} \int_0^T \tilde{\delta}_a(t)\, dt \qquad (3.74)$$

where

$$\tilde{\delta}_a(t) = \begin{cases} 0 & for\ \delta_a < \delta_{a\,max} \\ 1 & for\ \delta_a \geq \delta_{a\,max} \end{cases} \qquad (3.75)$$

The rudder saturation index:

$$S_{\delta_r} = \frac{100}{T} \int_0^T \tilde{\delta}_r(t)\, dt \qquad (3.76)$$

where

$$\tilde{\delta}_r(t) = \begin{cases} 0 & for\ \delta_r < \delta_{r\,max} \\ 1 & for\ \delta_r \geq \delta_{r\,max} \end{cases} \qquad (3.77)$$

The lateron saturation index:

$$S_{\delta_l} = \frac{100}{T} \int_0^T \tilde{\delta}_l(t)\, dt \qquad (3.78)$$

where

$$\tilde{\delta}_l(t) = \begin{cases} 0 & for\ \delta_l < \delta_{l\,max} \\ 1 & for\ \delta_l \geq \delta_{l\,max} \end{cases} \qquad (3.79)$$

The throttle saturation index:

$$S_{\delta_t} = \frac{100}{T} \int_0^T \tilde{\delta}_t(t)\, dt \qquad (3.80)$$

where

$$\tilde{\delta}_t(t) = \begin{cases} 0 & for\ \delta_t < \delta_{t\,max} \\ 1 & for\ \delta_t \geq \delta_{t\,max} \end{cases} \qquad (3.81)$$

The trajectory tracking specific performance vector, PV_{TT} is defined as:

$$PV_{CA} = [ca_i | i = 1,2\ldots,12] = [I\dot{\delta}_f I\dot{\delta}_e I\dot{\delta}_a I\dot{\delta}_r I\dot{\delta}_l I\dot{\delta}_t S_{\delta_f} S_{\delta_e} S_{\delta_a} S_{\delta_r} S_{\delta_l} S_{\delta_t}]^T \qquad (3.82)$$

Finally, a global sailing PI_{SAIL} can be defined as weighted sum of the tracking

trajectory PI_{TT} and control activity PI_{CA}:

$$PI_{TT} = w_{TT} \cdot PV_{TT} \qquad (3.83)$$

$$PI_{CA} = w_{CA} \cdot PV_{CA} \qquad (3.84)$$

$$PI_{SAIL} = \bar{w}_{TT} \cdot PV_{TT} + \bar{w}_{CA} \cdot PV_{CA} + \bar{w}_T \cdot PV_T \qquad (3.85)$$

where w_{TT}, w_{CA}, $\bar{w}_{TT}$, and $\bar{w}_{CA}$ are normalization and desirability weights. While w_T and PV_T represent the thrust contribution. The weights are assigned to each parameter based on subjective and relative importance upon each metric. Each component is normalized, with 0 corresponding to perfect performance. Also note that if or when the cable breaks, it penalizes the controller 10% for every second because in the study values of the PI_{SAIL} and PI_{CA} are accumulation indices over time.

A more detailed description of these metrics are provided in (Coulter, Moncayo, & Engblom, 2018b).

3.5. Case Study 1: Simulation with Lateron Control Surface

In order to demonstrate the benefit of adding a lateron as an unorthodox control surface simulation tests were performed and the effect on tracking and sailing performance analyzed with and without lateron.

The following plots in Figure 13 with no Lateron (left) and with the Lateron (right), present the value of implementing the control surface. Without the lateron, it has to overcome a large roll moment of inertia and it is unable to sail in ideal conditions. The lateron enables a faster lateral (y-direction) force response than the orthodox method of rolling an aircraft. These results support a previous hypothesis in (Engblom W. A., et al., 2016).

Figure 13 presents the results of the sailing performance when the UAS system

does not have lateron (in the left-sided plots). It is clear that the UAS must overcome a large rolling moment using available control surfaces to maintain sailing. As aileron actuator must deflect to maintain y-space separation and roll sailing condition at the same time, the control system is not able to guarantee a good sailing performance. Notice that with no lateron, the amount of thrust required in order to maintain sailing conditions. This conclusion is also reflected in the total performance index, which was run for both cases:

For no lateron $PI_{SAIL} = 0.6982$, while with lateron $PI_{SAIL} = 0.2339$.
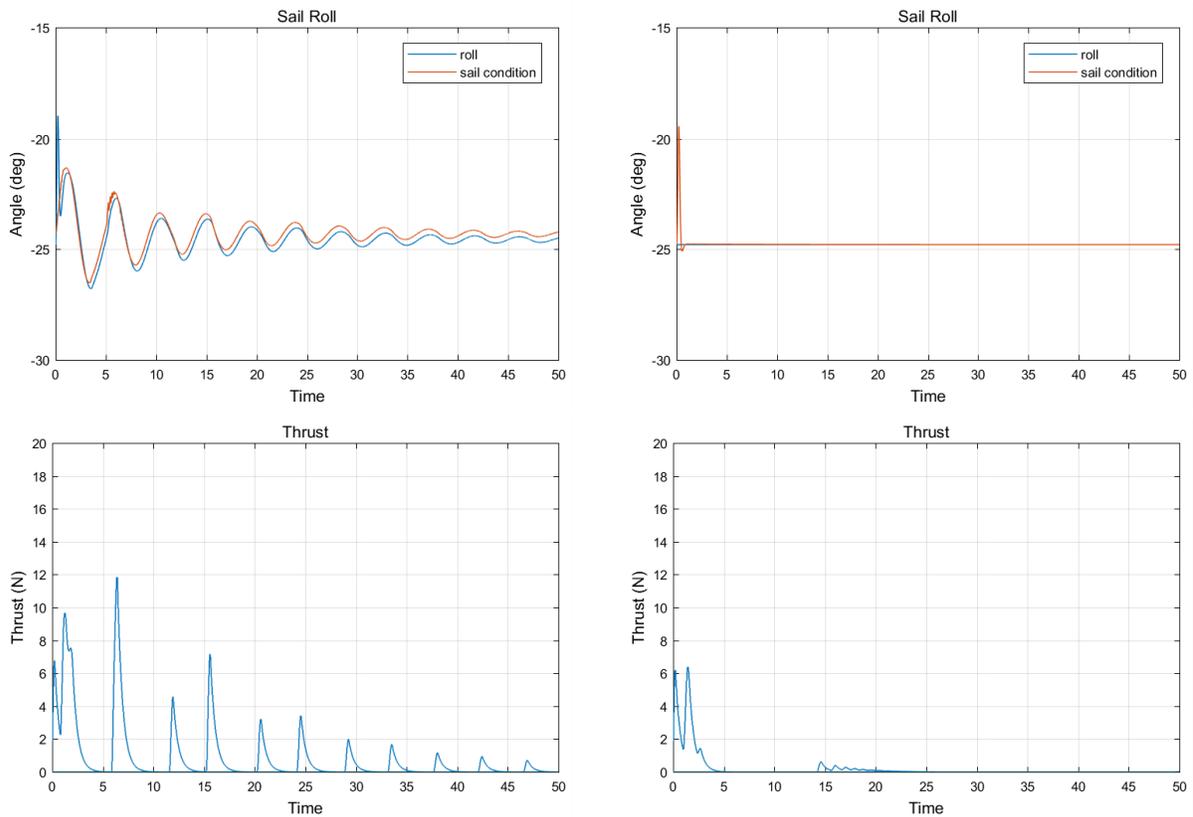
Figure 13 No Lateron (left) and Lateron edition (right)

3.6. Case Study 2: Comparison of $\mathcal{Z}_1$ and PID under Turbulence Conditions

This case study is an investigation of the controller robustness under low to high

turbulence levels as discussed in Section 2.3. In this case the performance is analyzed under aforementioned levels as well as during long segments of turbulent flights. This analysis considers whether the UAS platforms are able to sail, how well they can track the sailing conditions without breaking formation and if not, how long they can stay connected. It should be recalled that a turbulence of level 20, is characterized as a hurricane force. Although it is unlikely that DAP would have to experience sustained turbulence for extended periods of time such as 100 seconds, it is a good comparison of controller robustness. It is important to note that in this case the SAIL aircraft does not start at ideal initial sailing conditions. Table 4 shows the initial conditions used for these tests.

Table 4 Initial Condition of Case #2

State	Initial Condition (°)
Angle of attack	0
Sideslip angle	0
Yaw angle	20
Pitch angle	0
Roll angle	0
Turn-off Thrust	*5sec*

Table 5 Performance Index under Different Turbulence Intensities

| Turbulence Intensity | $\mathcal{L}_1$ | | PID | |
	PI_{SAIL}	PI_{CA}	PI_{SAIL}	PI_{CA}
0	0.2311	0.05209	0.2401	0.05090
2.5	2.4810	0.01106	4.3333	0.67434
5	2.4940	0.24840	4.4108	0.66937
15	3.8008	0.89992	7.0388	1.59445
20	3.7560	0.98816	3.8849	1.61949
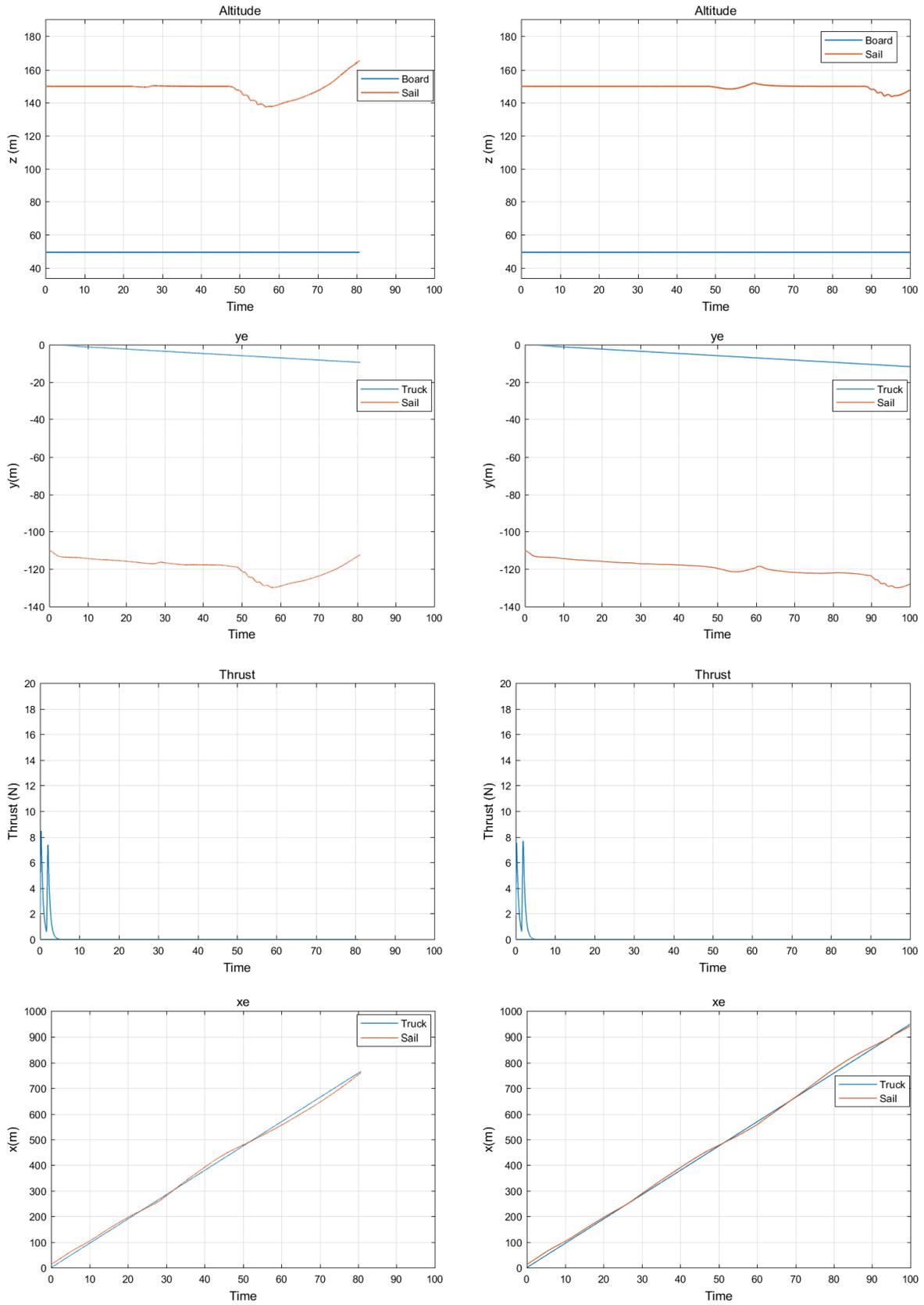
Figure 14 Positions and Thrust for PID (left) vs. $\mathcal{Z}_1$ (right) controllers at level turbulence 5 for 100s
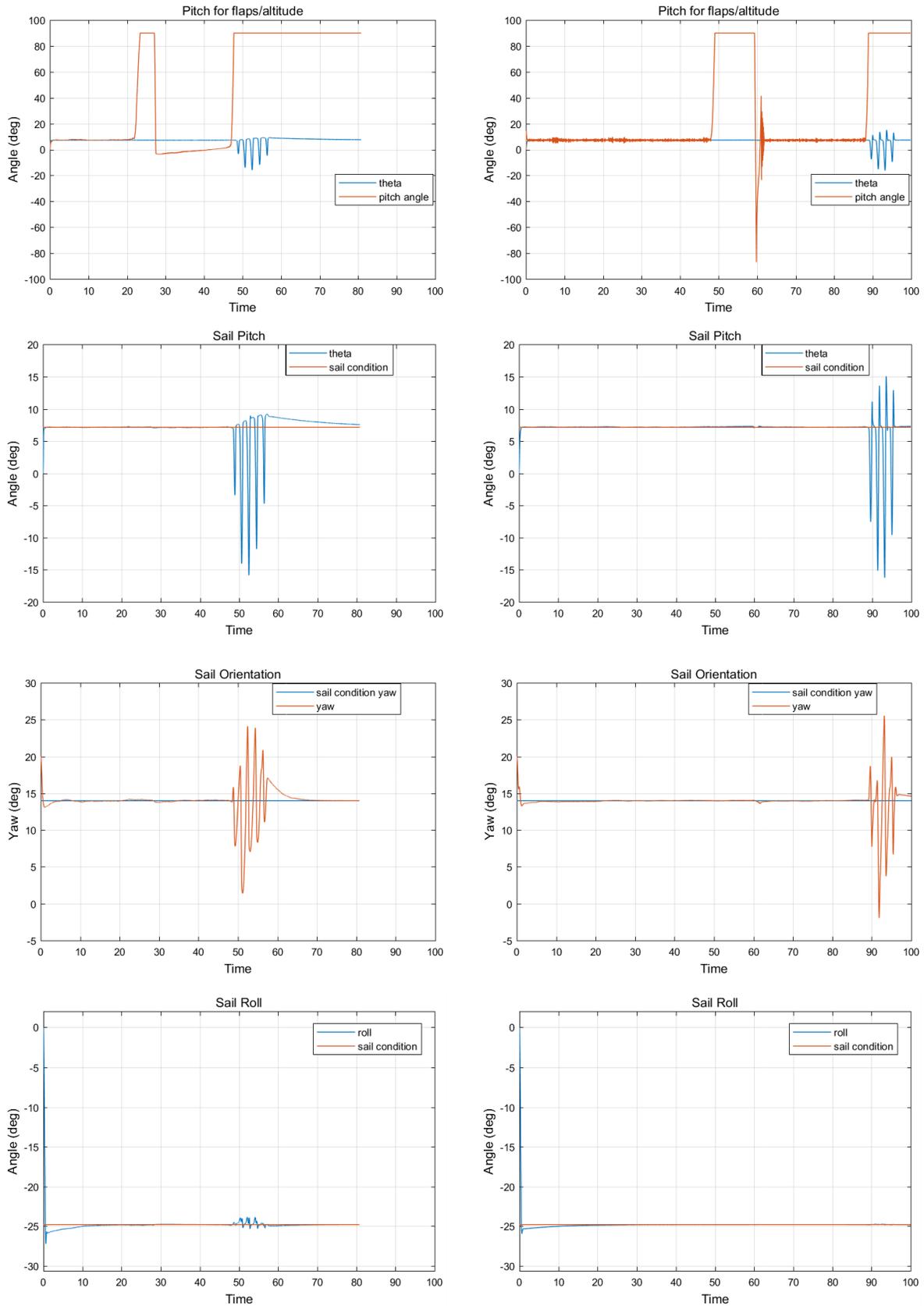
Figure 15 Control activity for PID (left) vs. $\mathcal{Z}_1$ (right) controllers at level turbulence 5 for 100s

Table 5 shows that at turbulence intensity of 2.5, which corresponds to approximately a wind force of 2.25 m/s (~5 mph gusts), PID controller has a sail performance of around 75% worse than $\mathcal{L}_1$.

Plots in Figure 14 demonstrate the behavior of formation flight distances and thrust for PID and $\mathcal{L}_1$ controllers at a moderately low level of 5. Specifically, the cable breaks at 80 seconds with PID controller in this case, which may be due to overwhelming stresses once the thrust turns off and altitude drops significantly while the sail exceeds its lateral spacing (y-direction) and it loses its position ahead of the truck (x-direction). Consequently, the controller attempts to quickly recover its positioning in all 3-axes and applies a strain to the cable. Therefore, with the PID controller the mission comes to a premature end at low levels of turbulence. These results are similar to those at a turbulence intensity of 2.5.

For $\mathcal{L}_1$ adaptive controller case under turbulence level of 5, as presented in Figure 14 that unlike the PID which demonstrates failure to sail around 50 seconds, the adaptive controller maintained sailing flight up to 90 seconds before degradation and without breaking the cable within 100 seconds.

Results in Table 5 also show that as the turbulence intensity increases so does the control action index for both controllers. This is expected and it is due to the increased demand on the control surfaces to maintain the sailing target conditions. As shown in Figure 15 flaps saturate for both controllers in their attempt to track the pitch angle and maintain the required altitude from the truck's trajectory.

For an extreme level turbulence of 15 compared to $\mathcal{L}_1$ adaptive controller, the PID controller presents a significantly worse performance i.e. approximately 85% and 77% for

both PI_{SAIL} and PI_{CA}, respectively. But at a severe turbulence level of 20 both controllers have similar sail performance, $\mathcal{L}_1$ adaptive controller is only ~3.4% better. Whereas, the PI_{CA} for $\mathcal{L}_1$ adaptive controller has an improved performance of about 64% over PID.
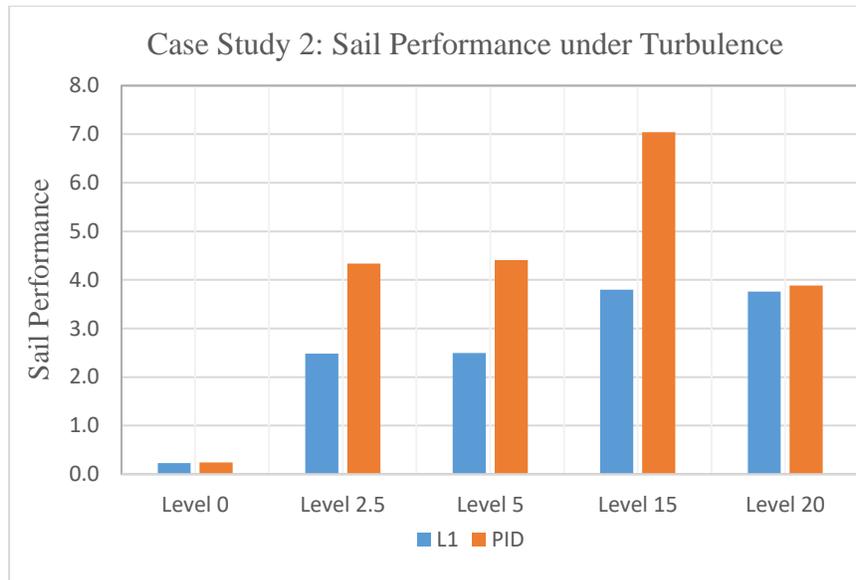
Figure 16 Comparison of Sail Performance for $\mathcal{L}_1$ vs PID during different levels of turbulence
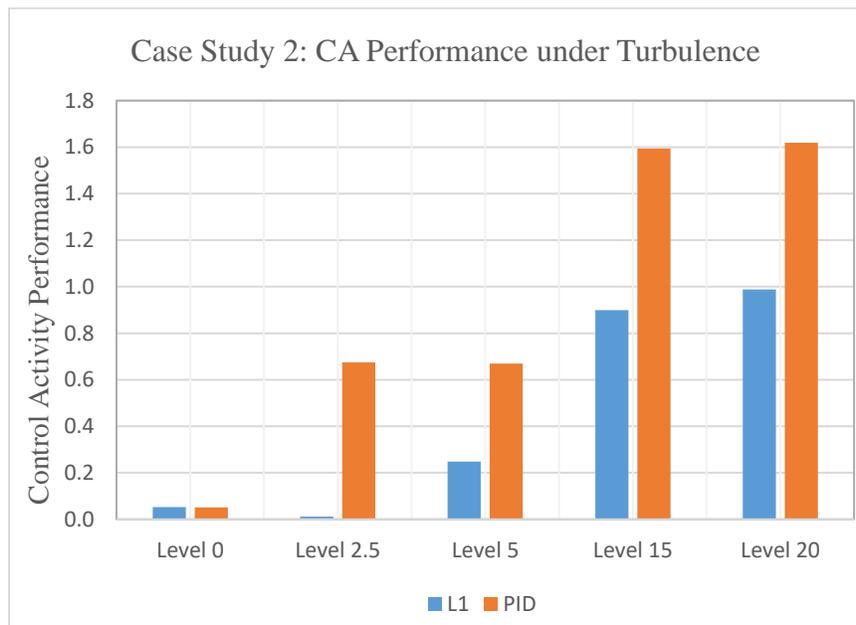
Figure 17 Comparison of Control Activity Performance for $\mathcal{L}_1$ vs PID during different levels of turbulence

Figure 16 and 17 summarize the performance evaluations for sailing and minimum control surface effort for both controllers at different turbulence intensities. It can be noted that at 0 turbulence of the set initial conditions PID is slightly better for both metrics but the difference is negligible. However, for all tested turbulence levels from low to severe, the $\mathcal{L}_1$ adaptive output feedback controller performs evidently better than the PID conventional controller demonstrating its robustness under challenging environments.

3.7. Case Study 3: Comparison of $\mathcal{L}_1$ and PID at different Initial Conditions

This case analyzes the control performance under the influence of different initial conditions, but maintaining the same target sailing conditions. Ideal conditions are based on wind speed and direction which determine the orientation of the UAS. Table 6 shows the conditions investigated.

Table 6 Initial Conditions Evaluated

State	Ideal Conditions (°)	Conditions 1	Conditions 2	Conditions 3	Conditions 4
Angle of attack	7.9	0	0	0	0
Sideslip angle	0	0	0	0	0
Yaw angle	13.98	20	0	0	20
Pitch angle	7.18	0	0	0	0
Roll angle	-24.789	0	0	0	0
Turn-off Thrust	*On*	*On*	*On*	*Cut at 5sec*	*Cut at 5sec*

Table 7 Performance Metrics for Controllers at Various Initial Conditions

Initial Conditions	PI_{SAIL}		PI_{CA}	
	$\mathcal{L}_1$	PID	$\mathcal{L}_1$	PID
Ideal Conditions	0.2339	0.2122	0.03152	0.03148
Conditions 1	0.2579	0.2731	0.03188	0.03166
Conditions 2	0.4474	0.4455	0.02503	0.02470
Conditions 3	0.4142	3.3134	0.26840	0.51173
Conditions 4	0.2302	0.2386	0.03110	0.03008

Table 7 shows that both $\mathcal{Z}_1$ and PID controllers have relatively similar sail performance metrics for Condition 1 and 4, with $\mathcal{Z}_1$ controller presenting slightly better indices as illustrated in Table 8. For Condition 2, the PID controller has a 0.43% improved sailing performance. While for Condition 3, $\mathcal{Z}_1$ controller presents significantly improved sailing performance i.e. 8 times better than PID controller. The PID controller deterioration in performance is because the cable breaks at 44 seconds, indicating that for certain initial conditions the PID controller may have low tolerance, and for this sailing configuration it cannot withstand being set at zero initial conditions and the thrust getting cut-off after 5 seconds.

Table 8 Difference Between PID with respect to $\mathcal{Z}_1$ for Sail Performance

Initial Conditions	Difference Between PID and $\mathcal{Z}_1$
Conditions 1	0.0152
Conditions 2	-0.0019
Conditions 3	2.8992
Conditions 4	0.0084

Table 7 also shows that the PID controller presents better demand from the control surfaces for Condition 1, 2 and 4. However, the difference to $\mathcal{Z}_1$ controller is minimal <2% for all 3 cases. In Condition 3 the PID controller fails to attain and maintain its sailing targets which affects the demand on its control activity making it perform 90.7% worse than the $\mathcal{Z}_1$ controller.

Figure 18 and 19 summarize the performance evaluations for sailing and minimum control surface effort for both controllers at non-nominal initial conditions while maintaining the same target sailing conditions.
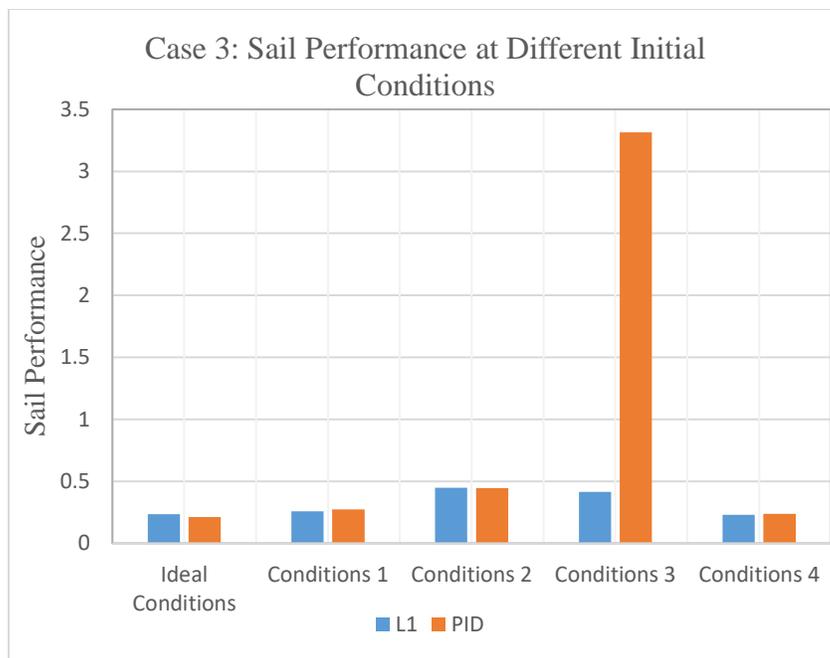
Figure 18 Comparison of Sail Performance for $\mathcal{Z}_1$ vs PID at different initial conditions
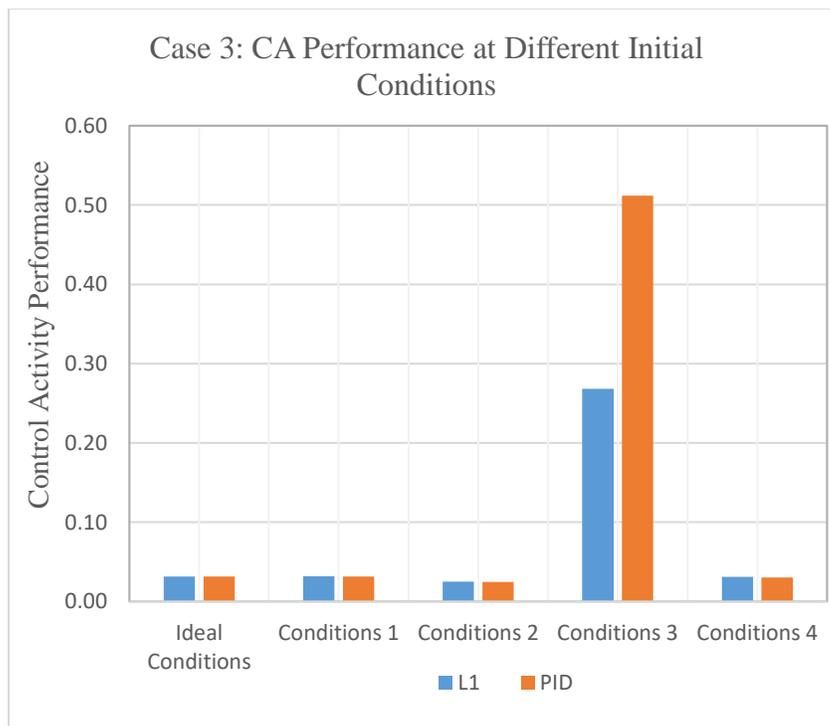
Figure 19 Comparison of Control Activity Performance for $\mathcal{Z}_1$ vs PID at different initial conditions

$\mathcal{Z}_1$ adaptive controller and PID controller had relatively similar indices for both PI_{SAIL} and PI_{CA} except Condition 3; where $\mathcal{Z}_1$ adaptive output feedback controller significantly outperformed the PID conventional controller, indicating the PID controller potentially has a lower tolerance when starting at non-ideal conditions.

3.8. Case Study 4: Changing Wind Direction

This case study, compares the robustness of both controllers under constantly changing wind direction while maintaining the same target sailing conditions. For this case, the simulation begins at nominal sailing conditions except that a sinusoidal of +/-10° is permitted in the direction of wind. Table 9 shows that PID controller has an improved sailing performance of about 3.9% over $\mathcal{Z}_1$ adaptive controller. This is also true for the control activity performance except that the difference is 0.00009, which is almost negligible in this case.

Table 9 Performance Metrics for Controllers with Changing Wind Direction

Controller	PI_{SAIL}	PI_{CA}
$\mathcal{Z}_1$	0.3354	0.02120
PID	0.3224	0.02111

Figure 20 shows that both controllers demand very little thrust especially when the wind direction is shifting further from the pre-determined sailing conditions. However, after the initial thrust effort, its contribution is less than 1.2 N for both controllers. The plots also show that the sailing performance captured in each time-step is relatively the same. Finally, although there is an initial disturbance in control activity for $\mathcal{Z}_1$ controller it quickly updates and produces a similar plot compared to PID. These are parallel evaluations to the accumulated metrics shown in Table 9.
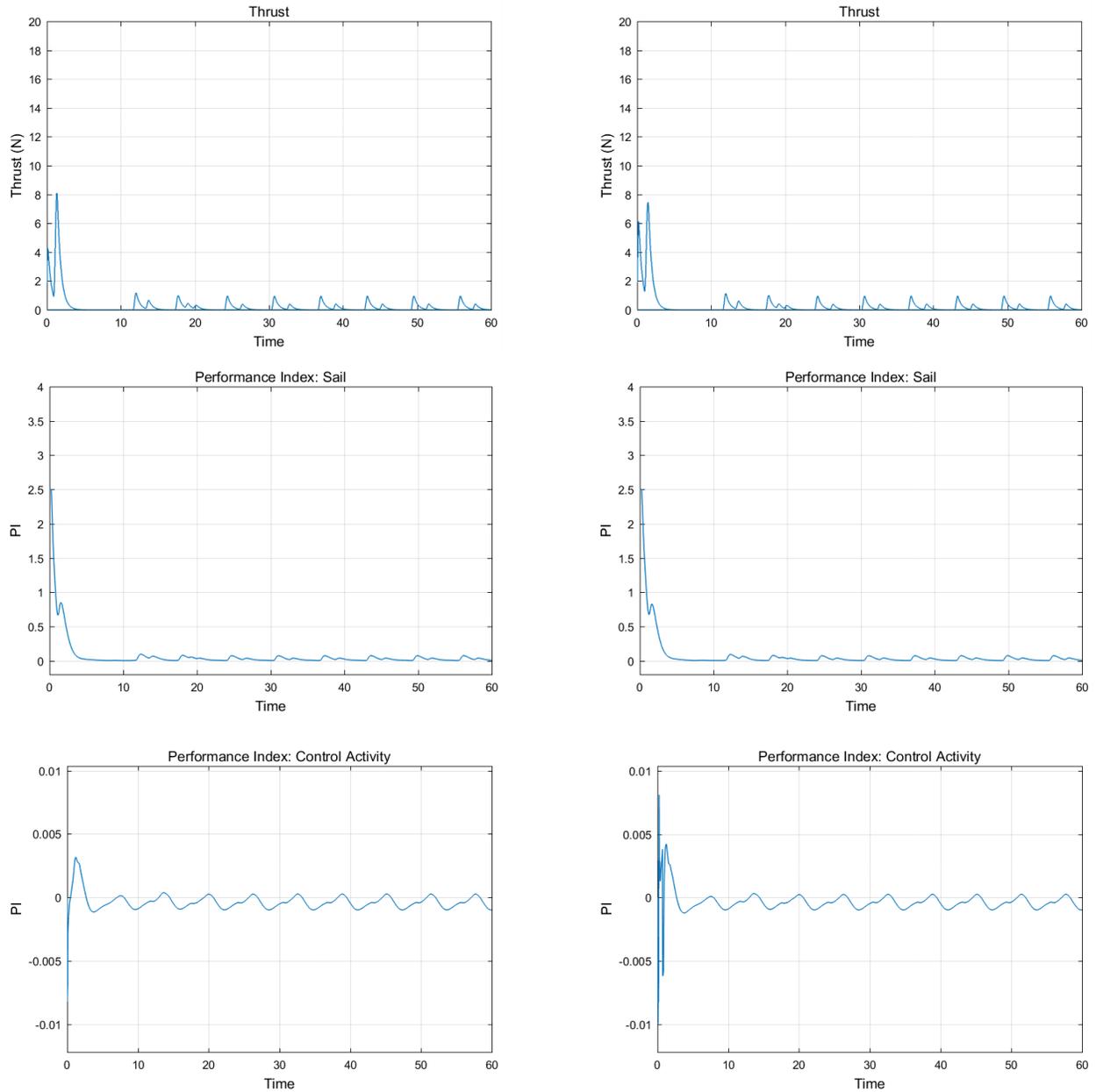
Figure 20 PID (left) vs. $\mathcal{Z}_1$ (right) controllers for constantly changing wind direction

3.9. Case Study 5: Changing Wind Speeds

In this case, wind speed is doubled, i.e. +6 knots higher than the expected wind at ideal conditions. The additional wind speed is sustained for 1min.

Table 10 shows that $\mathcal{Z}_1$ controller has 12% better sail performance than the PID

controller. Although they both have the same index for control activity, which indicates that $\mathcal{Z}_1$ controller gets the improved performance by either efficiently tracking the truck's trajectory and/or minimizing the demand for thrust.

Table 10 Performance Metrics for Controllers with Changing Wind Speed

Controller	PI_{SAIL}	PI_{CA}
$\mathcal{Z}_1$	1.84	0.581
PID	2.06	0.581
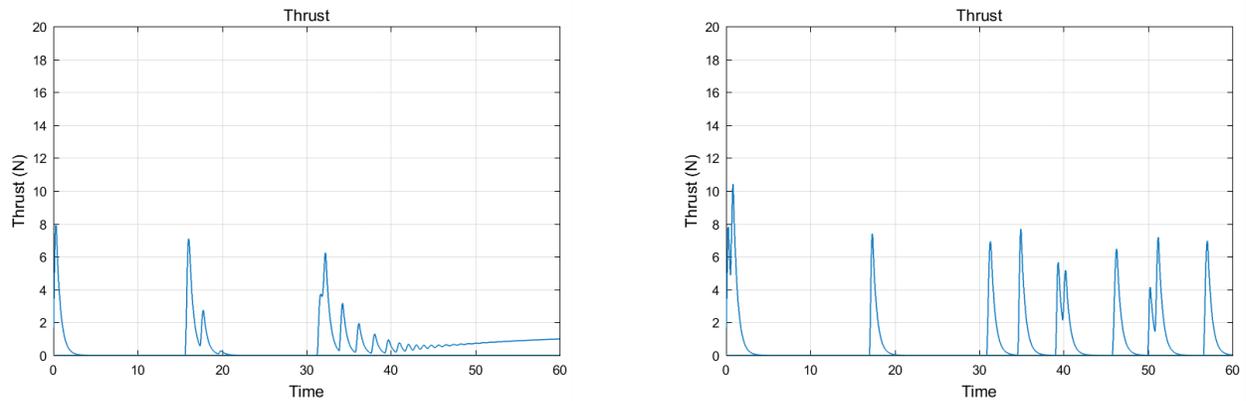
Figure 21 Thrust plots for PID (left) vs. $\mathcal{Z}_1$ (right) controllers with +6 knots additional wind

Figure 21 shows that both controllers do not sail because they are constantly demanding thrust. For instance, $\mathcal{Z}_1$ controller demands thrust when needed then zeros-off while PID controller seems to harbor a growing desire for more thrust after 40 seconds. Therefore, an additional analysis was performed but cutting off the thrust at 5 seconds and the results are presented in Table 11.

Table 11 Performance Metrics for Controllers with Changing Wind Speed, Thrust Cut at 5 sec

Controller	PI_{SAIL}	PV_{CA}
$\mathcal{Z}_1$	0.6385	0.6182
PID	4.2818	1.2172

In this case, the PID controller's performance drastically falls. This is because the

cable breaks at 36.5 seconds as shown in Figure 22. Therefore, in this circumstance $\mathcal{Z}_1$

controller's sail performance is almost 7 times better than the PID and presents almost

twice the improved control activity performance. Figure 22 also shows that although the

SAIL UAS loses its position ahead of the truck, $\mathcal{Z}_1$ controller is able to keep on recovering.
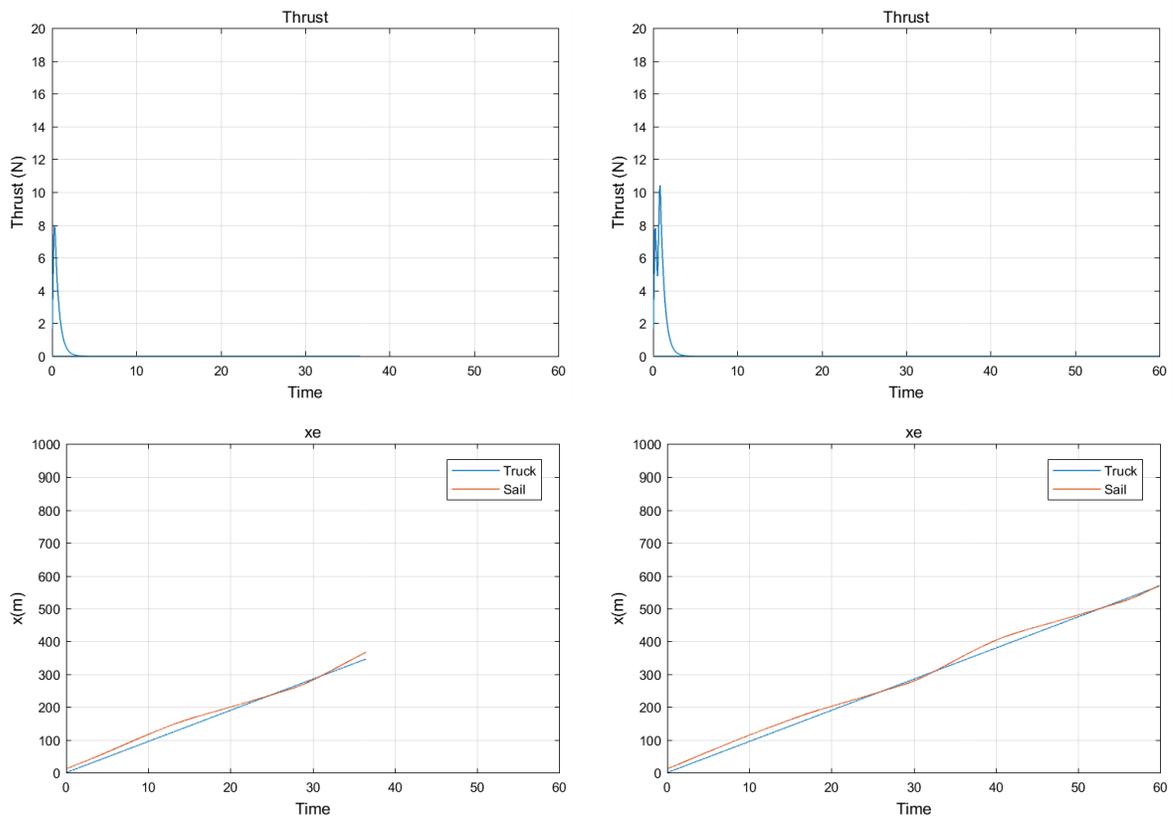
Figure 22 Thrust and forward distance plots for PID (left) vs. $\mathcal{Z}_1$ (right) controllers with +6 knots, thrust cut-off at 5 seconds.

Figure 23 and 24 summarize the comparisons when wind speed is doubled without

adjusting the sailing target conditions to match the new wind speed within 60 seconds. $\mathcal{Z}_1$

controller generally has better performance for this case, in both the sailing and control

activity effort. However, both controllers consistently necessitate thrust of >6 N, therefore

a follow-up test was performed with the thrust turning off at 5 seconds. The performance

of the PID controller rapidly deteriorated because the cable broke. Note, that it was observed in Figure 23 that the sail performance of the $\mathcal{L}_1$ adaptive controller is better at cut-off thrust than with thrust.
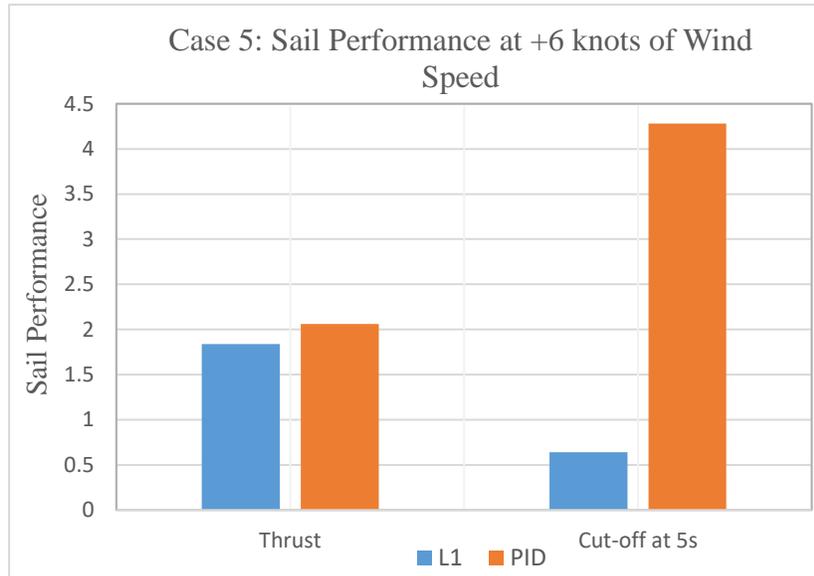
Figure 23 Comparison of Sail Performance for $\mathcal{L}_1$ vs PID at +6 knots of wind with and without thrust
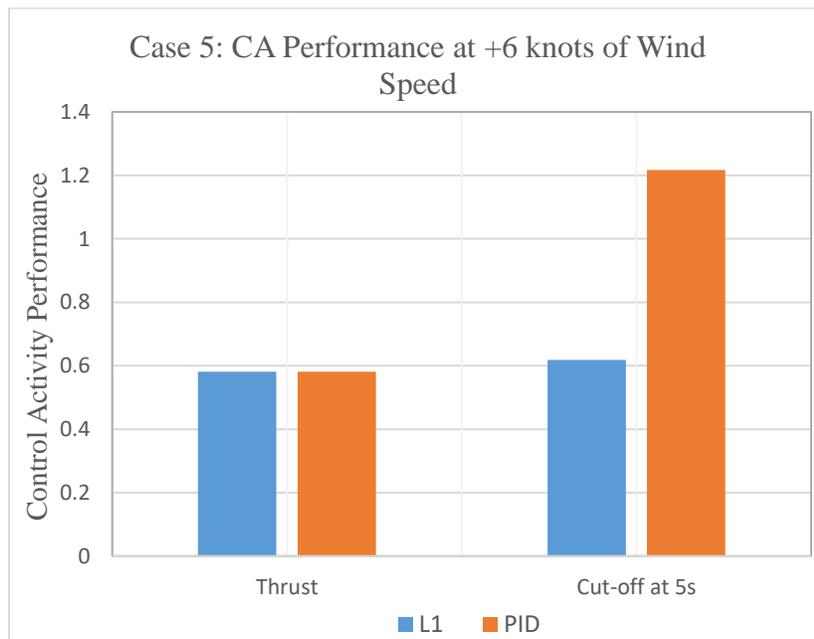
Figure 24 Comparison of Control Activity Performance for $\mathcal{L}_1$ vs PID at +6 knots of wind with and without thrust

CHAPTER 4: DAP UAS Research Test-Bed

This section briefly describes the glider UAS flight test-bed used to validate the performance of the control laws. The chosen airframe of the DAP research platform is the commercial MAXA Pro 4m powered gliders distributed by Kennedy Composites based in Texas. These UAS' were modified to use an externally mounted motor-propeller with adequate power (~500 W) to ascend to target altitudes within a minute. Other modifications include structural changes to place avionics, cable release mechanism and for structural integrity. The gross weight of a glider with all components is currently around 2.75 kg (or ~6 lb). Figure 25 shows the MAXA Pro 4m glider's airframe at Daytona Beach RC Club.

Figure 25 MAXA Pro 4m Glider (photo taken at Daytona Beach RC Club)

4.1. Airframe and Propulsion

The UAS requires a microcontroller, also known as an onboard computer, in order to test algorithms for autonomous flight and to record in-flight data essential to proving the DAP concept. For the purposes of this thesis a "Pixhawk Autopilot" board is used. This low-cost and compatible board has series of digital and analog sensors that provide states

which are used by controllers and stable flight. A number of sensors are interfaced with the flight computer for measuring and estimating different flight parameters including vehicle position, angular rates, accelerations, velocity, attitude, wind direction. The sensor suit includes a uBlox LEA-6H high performance GPS, a PX4 digital airspeed, a ST Micro L3GD20H 16-bit gyroscope, a ST Micro LSM303D 14-bit accelerometer / magnetometer, an Invensense MPU 6000 3-axis accelerometer/gyroscope, MEAS MS5611 barometer.

MAXA Pro 4m

The main dimensions and properties of this vehicle used during flight testing are presented in Table 12:

Table 12 General Specifications for the MAXA Pro 4m

Specification	Aircraft *SAIL*
Wing Platform Area	8.8 ft^2 (0.82 m^2)
Total Mass	5.5 lb (2.5kg)
Wing Span	13.1 ft (4m)
Aspect Ratio	19
Airfoil Section	Proprietary
Not-to-exceed Speed	30 mph (28 knots)

Hacker A30 12L Motor V3

The electric AC brushless motor chosen was to develop 1000 RPM/V [Kv]. Its overall dimensions 37.2 x 39 mm with a shaft of 5 mm and weight 143 g. Its maximum current is 35A and a maximum power 500W.

Figure 26 Hacker Brushless Motor

Electronic Speed Controller (ESC)

Castle Creations Phoenix Edge Lite, 34V 50-Amp ESC with 5-Amp BEC. This ESC can be used with 2-8 cell LiPo batteries. It weighs 56 g with wires and dimensions of 1.0 x 2.0". For this project, stick programming was used to add a 'Hard Brake – No Delay', to prevent the prop from wind-milling when the throttle is off for gliding.

Figure 27 Castle 50 Amp ESC

Folding Propellers

It is featured with Aeronaut Cam-Carbon folding propeller blades. These are designed through CAM technology. There are very thin and provide high efficiency with low power absorption from the electric motor. Dimensions: 12.0 x 6.5", maximum RPM

[1/min] is 13000.

Figure 28 Aeronaut Cam-Carbon Folding Prop

Multiplex Spinner

A Multiplex Folding Prop Spinner was designed in CATIA then 3D printed at ERAU. Paired with a 3in shaft that replaced the original 5mm shaft in the motor.
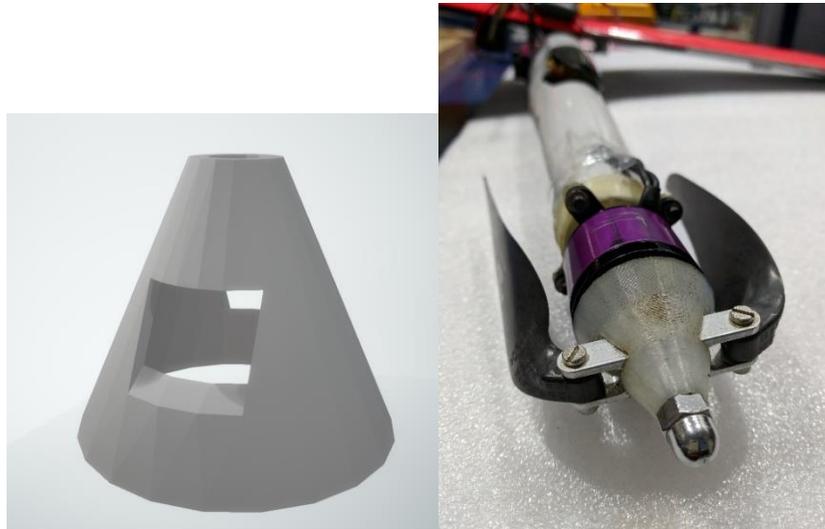
Figure 29 Multiplex Folding Prop: 3D model (left), final part (right)

4S LiPo Battery

This LiPo battery supplies power to the motor alone. The Turnigy Nano-Tech with 4 cells and a nominal voltage of 14.8V. The discharge rated at 1300mAh and its overall dimensions: 73 x 31 x 35 mm and weighs 208 g.

Figure 30 4S LiPo battery

3DR Power Module

The LiPo battery is connected via a 3DR power module to regulate any power that can be used as a backup for sensors (not servos) in case the receiver pack fails during flight.

4.2. Cable

A variety of cable materials were investigated and used including nylon, dyneema and nylon-dyneema hybrid with diameters of less than 1mm and maximum length of 200m. The required rating to ensure safety during all aerodynamic forces that the gliders may produce is typically a max. 7lbs while sailing. However, transient shock loads can exceed the limit therefore all cables were rated for 50lb tension force.

Table 13 Cable Specifications

Material	Dyneema
Cable Length (max)	656 ft (200 m)
Cable Diameter	0.039 in (1-mm)
Cable Tension Safety Factor	3.0
Break Strength	300 lbf (1335 N)

4.3. Avionic Systems

The onboard flight computer and sensors were integrated within the airplane

with the hardware architecture as shown in Figure 31. This section describes the flight management hardware and sensors.
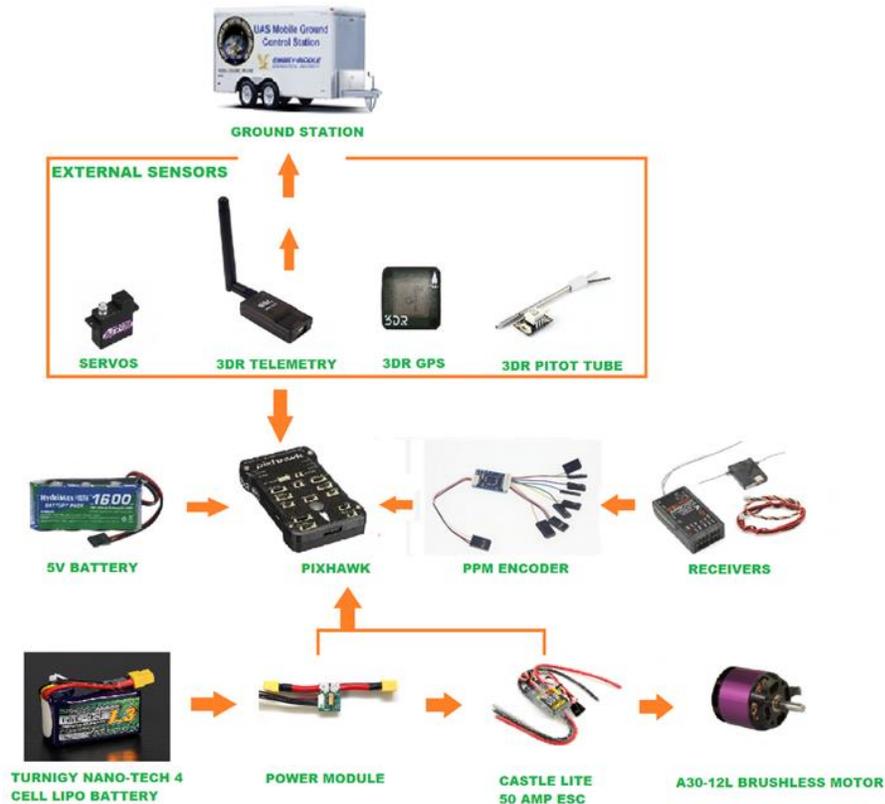
Figure 31 Hardware Interface Scheme of the Prototype Autopilot.

Pixhawk Autopilot

The primary flight computer that is used on board the DAP is the PixHawk v2 (PX4). This autopilot board is designed by an open-source hardware development team from The Computer Vision and Geometry Lab of ETH Zurich in association with 3D Robotics and ArduPilot Group.

PX4 is a commercial platform that has an ARM Cortex M4 with a principal clock of 168MHz. The processor runs Nuttx real-time operative system which contains drivers for on-board sensors such as accelerometers, gyroscopes, barometer, and magnetometer and global positioning system (GPS). In addition to the on-board sensors, the OBC has a

microSD slot, ADC, DSM interface for RC receiver antenna, and communication buses such as UART, SPI, CAN and I2C and a 2MB flash for data logging. As well as 14 PWM/servo outputs.

Figure 32 Pixhawk Autopilot Board

InvenSense MPU 6000 Inertial Sensor

The MPU 6000 is a 6-axis motion tracking device. It features a combination of 3-axis gyroscope and a 3-axis accelerometer inside a 4 x 4 x 0.9 mm QFN footprint and it communicates through a serial interface in an I^2C protocol.

Figure 33 MPU 6000

ST Micro LSM303D

The LSM303D is a 14-bit ultra-compact compass that features 3D digital linear acceleration sensor and a 3D digital magnetic sensor. It includes an I^2C/SPI serial interface, the former supports standard and fast mode (100 Hz and 400 Hz) and the latter a standard interface.

ST Micro L3GD20H

The L3GD20H is a 16-bit MEMS motion sensor: 3-axis digital output gyroscope. This is a low-power angular rate sensor. It uses a sensing element and an IC interface capable to provide angular rate to the external would through I^{2}C/SPI digital interface. It also has a full scale of +/- 245, +/- 500, +/- 2000 degrees per second and is able measure rates at different bandwidths.

UBLOX LEA-6H GPS Receiver Module

This GPS module has an in-built Antenna with 2.5 m accuracy. It also includes HMC5883L digital compass. The module can conveniently be mounted away from sources of interference such as the motor. It has a 5 Hz update rate and a low noise 3.3 V regulator. The dimensions are 38 x 38 x 8.5 mm and weight 16.8 g.

Figure 34 3DR GPS with compass module

3DR Telemetry

The 915 MHz (American) Telemetry Radio Set. The data-link is used to communicate to the ground control station to vehicle wirelessly, allowing for a view of in-flight data. These radios have -117dBm receiving sensitivity and use Frequency Hopping Spread Spectrum (FHSS). The dimensions are 25.5 x 53 x 11 mm (without antenna) and weigh 11.5 g (without antenna).

Figure 35 3DR Telemetry

3DR Pitot-Static Tube

The 3DR Pitot-Static tube paired with Measurement Specialties 4525DO sensor. This digital airspeed sensor has a 1 psi measurement range (approximately 100 m/s). The data is delivered at 14-bits from a 24-bit delta-sigma analog-digital-converter (ADC) at a resolution of 0.84Pa. It also measures temperature which allows the MS5611 static pressure sensor on Pixhawk to calculate true airspeed from indicated airspeed. Kit dimensions: 120 x 16 x 78 mm, and weighs 18 g. In order to integrate and bond pitot-static tube to the aircraft's leading edge a case was designed in CATIA then 3D printed at ERAU.
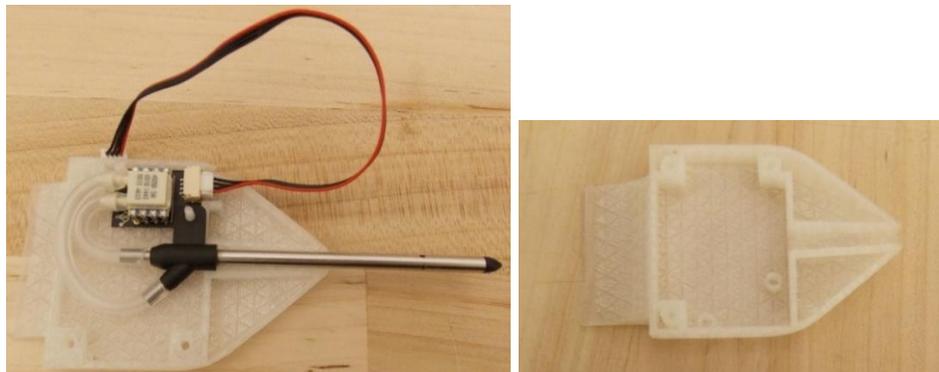
Figure 36 Pitot-Static Tube and Pressure Sensor

Spektrum Carbon Fuselage Receiver

The AR9320T 9-Channel Carbon Fuse Integrated Telemetry Receiver by Spektrum

RC is 2.4 GHz system. This receiver (RX) is capable of 11ms frame rates. It reduces RF limitations due to the material of the glider fuselage. In order to increase redundancy an additional satellite is connected to the RX. Dimensions: 48.5 x 28.3 x 20.9 mm and weighs 17.83 g.
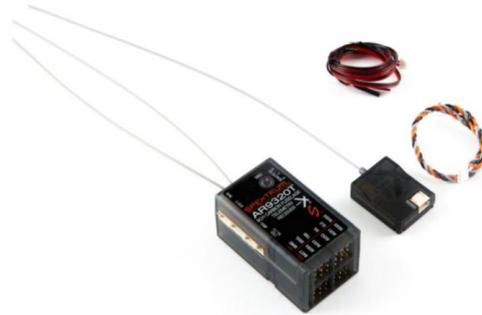
Figure 37 AR9320T 9 Channel Carbon Fuse Telemetry Receiver

Spektrum DX8 Transmitter

DX8 8-Channel DSMX Transmitter Gen 2, Mode 2 by Spektrum RC 2.4 GHz remote control. This is used for manual pilot control and used to switch to autonomous flight. All 8 channels are used, 5 control surfaces: ailerons, elevator, throttle, rudder and flaps. The other three channels: emergency motor kill, cable release and switch to transition into autonomous flight.

Figure 38 Spektrum DX8 Transmitter (TX)

PPM Encoder

Translates 8 PWM (pulse width modulation) signals into one PPM (pulse position modulation) signal, allowing you to connect a PWM receiver to the PX4 over one wire.

MKS DS6100 -MG Digital Servo

The MKS DS6100 use + PWM with an operating voltage of 4.8 – 5.0 V with a dead band of 0.001 ms. Dimensions 22.5 x 10 x 23.5 mm and weigh 9.5 g. There are 7 servos onboard the aircraft.

Figure 39 DS6100 Servo

NiMH 4.8V 1600mAh Rechargeable Battery

A HydriMax NiMH 4.8V 1600mAh Rechargeable Battery Pack with a maximum discharging rate of 12 A. This supplies power to the PX4 autopilot, sensors and servos. Its overall dimensions: 60 x 34 x 17 mm and weighs 85 g.
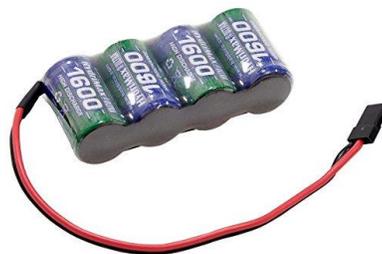
Figure 40 NiMH 4.8V 1.6A

4.4. Flight Testing Software

The software environment used is the Mathworks® Pixhawk Pilot Support Package (PSP). It generates ANSI/ISO C from Simulink® models explicitly created for Pixhawk FMUv2 (Flight Management Unit). This interface allows for the customization algorithms that leverage onboard sensor data and supplementary calculations at runtime. Once the flight control system (FCS) has been successfully modeled, simulated and verified, the Pixhawk Target can be used to deploy the control system onto the PX4 hardware.

The Pixhawk PSP was used in combination with Pixhawk Firmware that was enhanced at the ERAU's Flight Dynamics and Control Research Lab (FDCRL).

The Pixhawk PSP firmware relies on a publisher-subscriber communication architecture for Inter-Process communication on the PX4. The libraries allow the user to interact with GPS, IMU, light emitting diode (LED) and PWM outputs for serial RX/TX communication, as well as the data exchange through micro-Object-Request-Broker application (uORB) topics. Topic information is exchanged in defined known "C" structures. The uORB topics used here are for airspeed and wind estimation.

The additional FDCRL firmware applies Extended Kalman Filter (EKF) to sensor data from the PSP libraries. In addition, it is capable of logging and recording flight data from sensors, actuators and any control signal developed in the Simulink environment. This is particularly useful when analyzing post-flight data which can lead to redesigning or tuning algorithms. Figure 42 shows the target blocks implemented (Pilot Engineering Group, 2015).
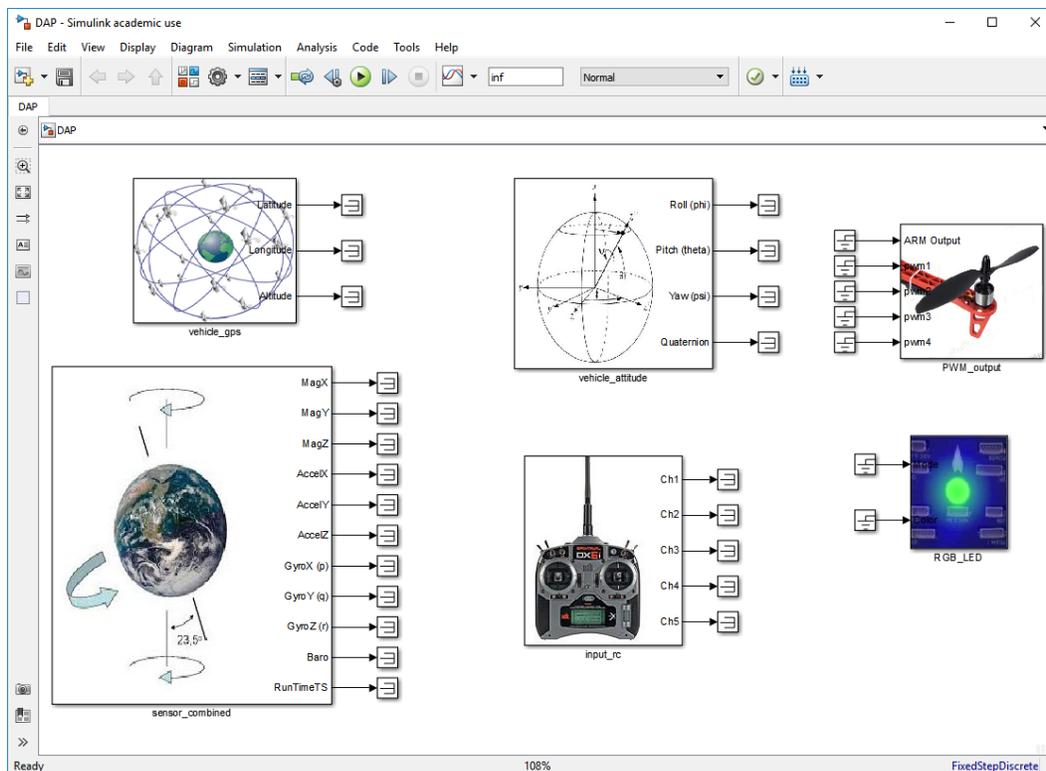
Figure 41 Sample blocks from Pixhawk Support Package

4.5. Ground Control Station

Fight operations utilize the ERAU Mobile UAS Ground Control Station (GCS) which is an enclosed trailer that houses all necessary equipment for communication with the aircraft and observing flight data in real-time. The fundamental tasks of the ground station are to provide the following abilities: receive, process, and record telemetry data from the aircraft and display flight information to the flight test coordinator. For example, KSC Tower 313 wind profile measurements are also being accessed wirelessly from this station, in order to investigate the wind estimation capabilities on the flight computer. Data communication between aircraft and the ground station is via a duplex serial data link using an RF transceiver operating at 900 MHz, (previously shown in Figure 31). The data link connects to Mission Planner.

Ground Weather Station

The GCS hosts a weather station that is used to collect validation data for wind estimation. Peet Bros. equipment was used which includes (shown in Figure 41):

- ULTIMETER 2100 Keyboard/Display Unit,

- ULTIMETER PRO Anemometer/Wind Vane (w/40' cable),

- Outdoor Temperature Sensor (w/25' cable)
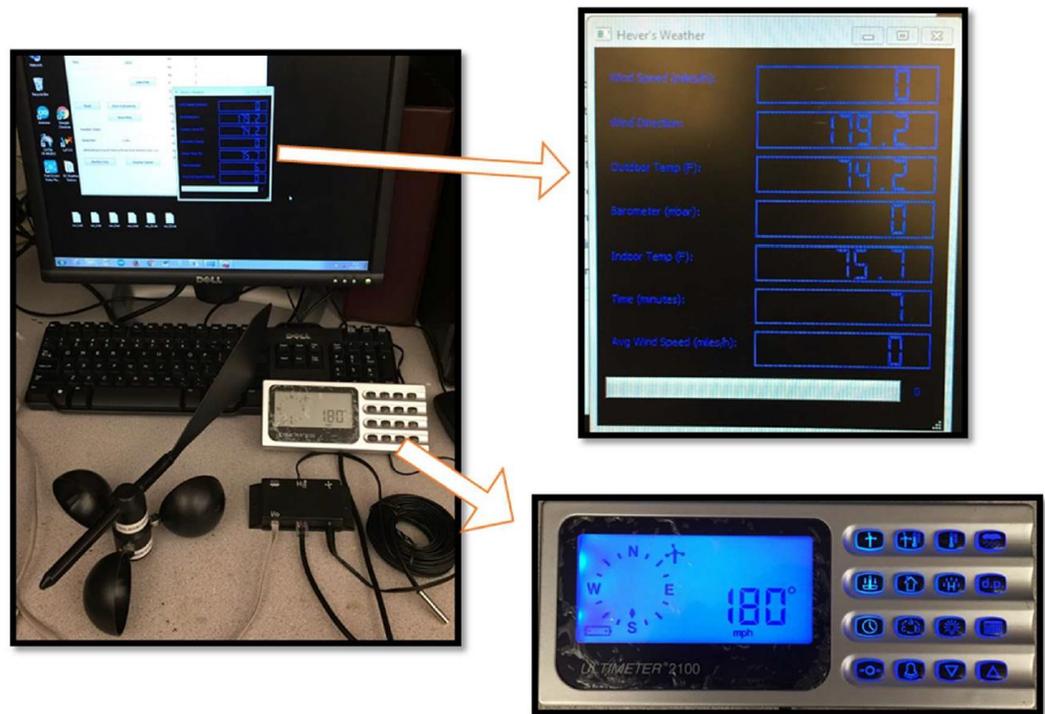
Figure 42 Ground Control Station's Weather Station

The weather station collects wind data at 2.9Hz with a wind speed accuracy of 0.9m/s and 5% for the 16-point magnetic direction sensing. The ground weather station setup is securely mounted on a pole close to the flight path approximately 7m above the ground.

4.6. Flight Testing Program

Three flying facilities were used, namely Daytona Beach RC Club, DeLand RC Club and the Shuttle Landing Facility (SLF) at Kennedy Space Center. The latter is shown in Figure 43. The flight tests are part of an extensive flight test program initiated to provide demonstrate of the DAP concept.

The flight tests involve operating one UAS at KSC on a fishing line and being reeled by an individual on a moving pick-up truck. The pilot rides safely in the bed of a pick-up truck using a harness, along with other personnel operating the cable to collect tension data via a load cell, and to communicate with the ground station via radio. The truck and aircraft move together in parallel to the runway, beginning at one end of the runway, and landing/stopping at the other end as displayed in Figure 44.
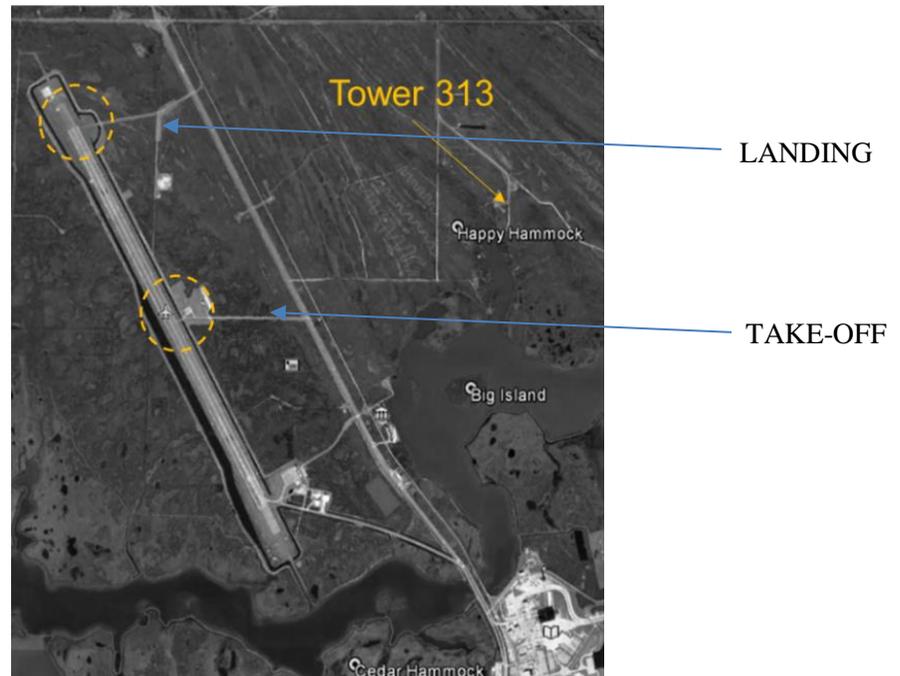
Figure 43 Shuttle Landing Facility and Tower 313

(yellow circles represent typical take-off and landing areas)

Figure 44 Pilot harnessed in a truck bed with the glider cabled to a fishing pole (taken at SLF)
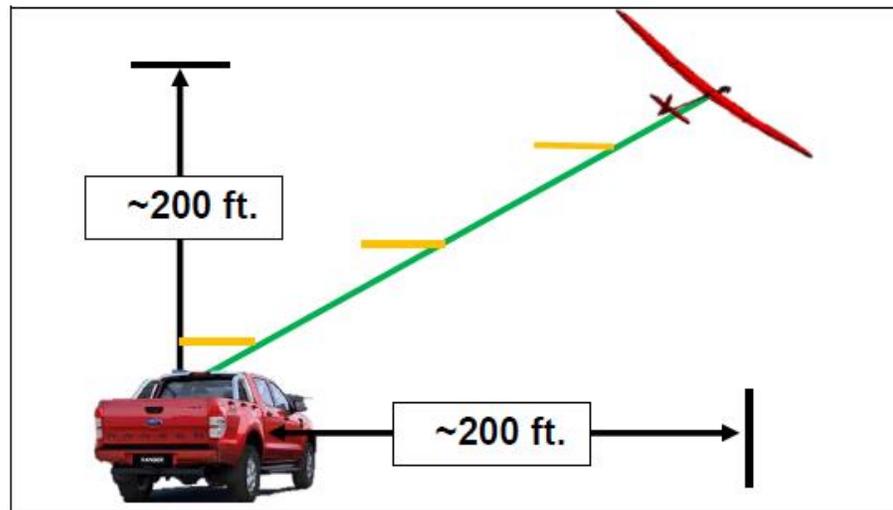
Figure 45 Truck/Cable/Glider Combination

4.6.1. Manual Flight Testing Truck/Glider

The initial direction of DAP was to provide proof-of-concept by letting an RC pilot train via two vocations: simulation (described in Chapter 2) and on numerous Truck/Cable/Glider flights using the flight testing program described. The aim was to show

the *SAIL* UAS "towing" the truck with the appropriate cable tension force, as if the truck were the second aircraft, as shown in Figure 45. A load cell was used to collect cable tension data, then analyzed against data collected from the PX4 to evaluate that when the power was cut-off that the glider pulled on the cable in an attempt to sail.

The flight test data displayed in Figure 46 is from a test at NASA SLF. The airspace provided ample length for the pilot and truck to get into sailing position without having to make a turn. Furthermore, wind profiles recorded by nearby Weather Tower 313 can provide target altitude, UAS orientation, ground speed and horizontal spacing required for effective sailing. Note that these tests were predominantly manual hence FFC controller was not implemented.
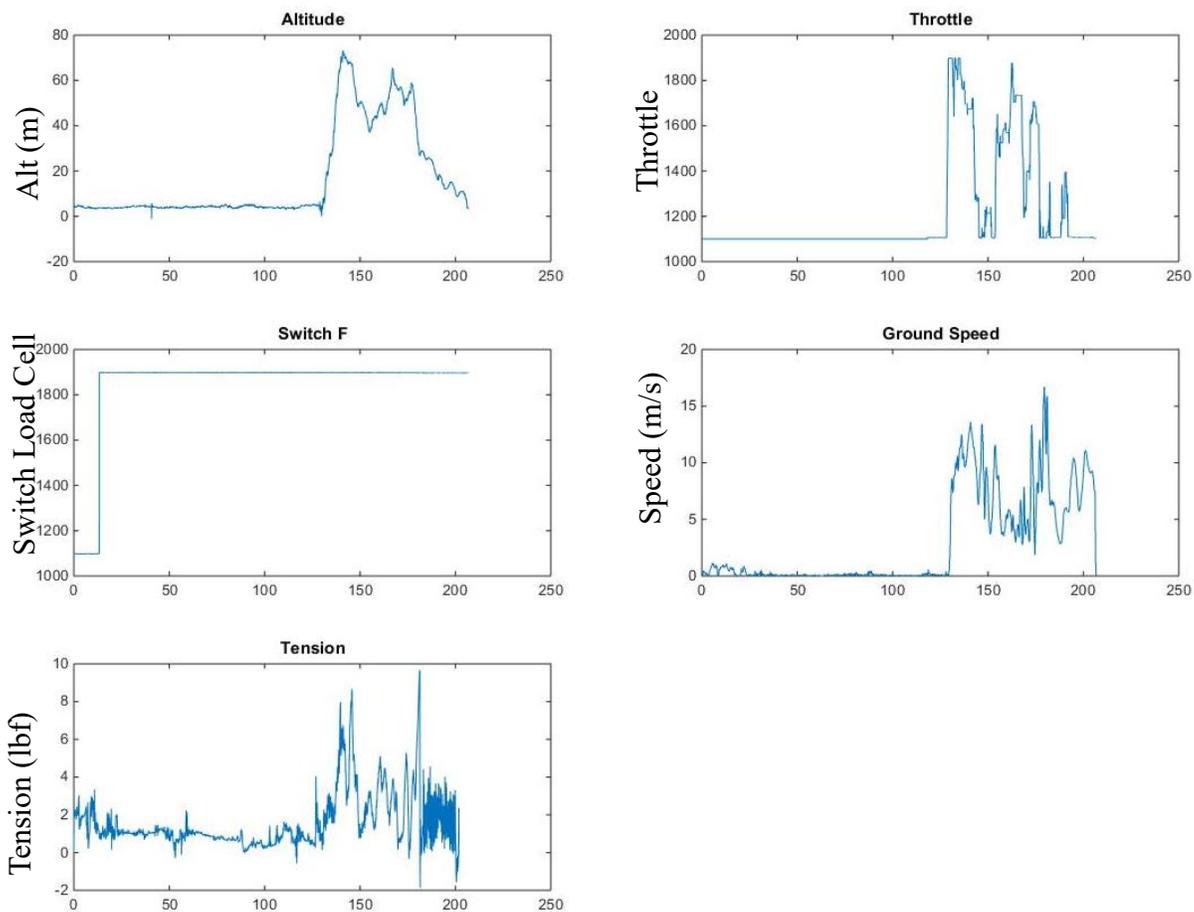
Figure 46 Flight Test: Fully Manual Truck/Cable/Glider

The above data recorded from the flight test provided no evidence that the aircraft sailed. Sailing would imply that:

- Altitude and ground speed hold (or increase)

- Throttle if OFF (=1100)

- Tension is significant (> 4 lbf)

However, there was no supportive evidence, which is understandable because unlike a kite-surfer there is no way for the possible to 'feel' the sail and relying solely on visual cues. This led the research into the direction of autonomous flight.

4.6.2. Flight testing using a Formation Flight Controller without the Cable

The formation flight controller has three segments: vertical, lateral and forward. In flight, the FFC was tested with a linear controller. Figures $47 - 50$ display flight test data during the tuning phase. The PWM value of 1500 denotes that the pilot is switching from manual flight command to auto-command is on. These flight test were performed at Daytona Beach RC Club. The problem was simplified by decoupling the components that is first tuning the vertical components, then the lateral components, finally the forward components. Furthermore, only a proportional controller was used in the outer-loop and inner-loop. In a future study, various controllers may be implemented.

The plots in Figure 47 show the glider holding the commanded altitude $z = 140\ m$. The dotted lines highlight the autonomous segments. The plots in Figure 48 show the glider tracking in the lateral component, the command tested was for the controller to hold the y, once switched to autonomous.
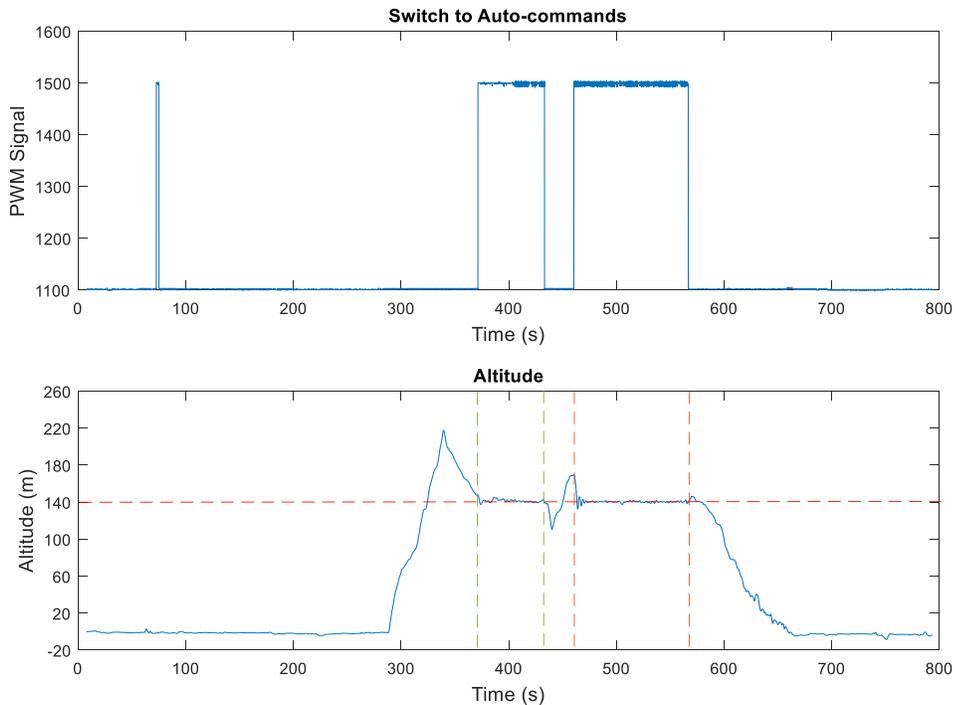
Figure 47 Flight Test: Altitude Hold
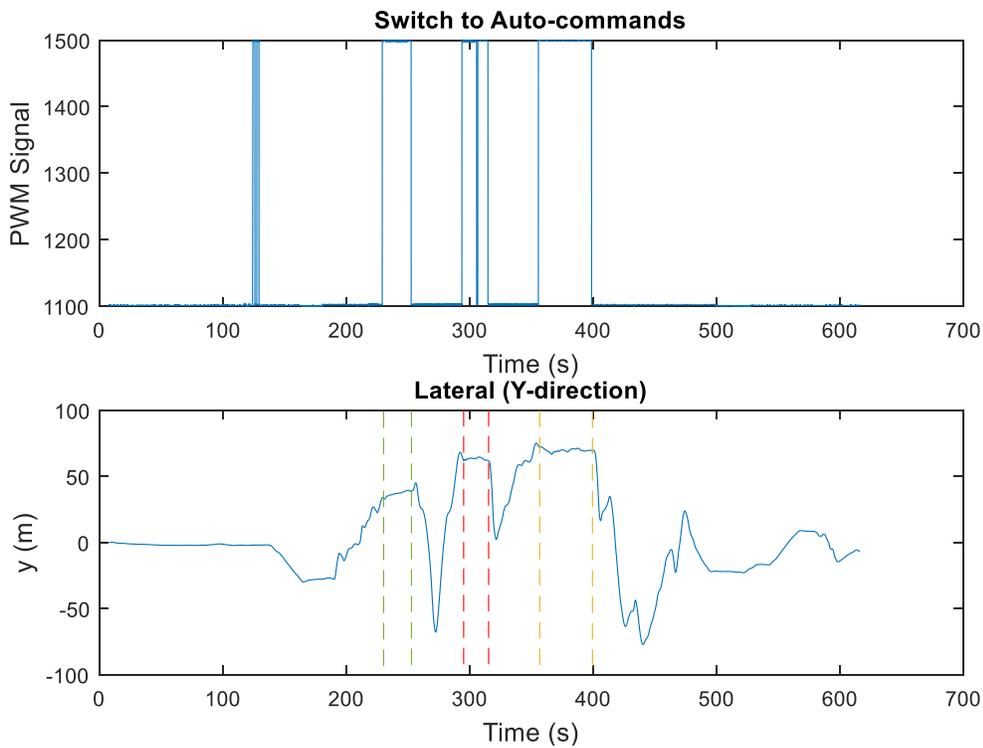
Figure 48 Flight Test: Lateral Tracking

Figure 49 shows forward tracking during tuning, since the gains can be adjusted in-flight an improvement can be seen in the last segment. Figure 50 shows a segment of the ground velocity it has a +/-1 m/s accuracy around the commanded.
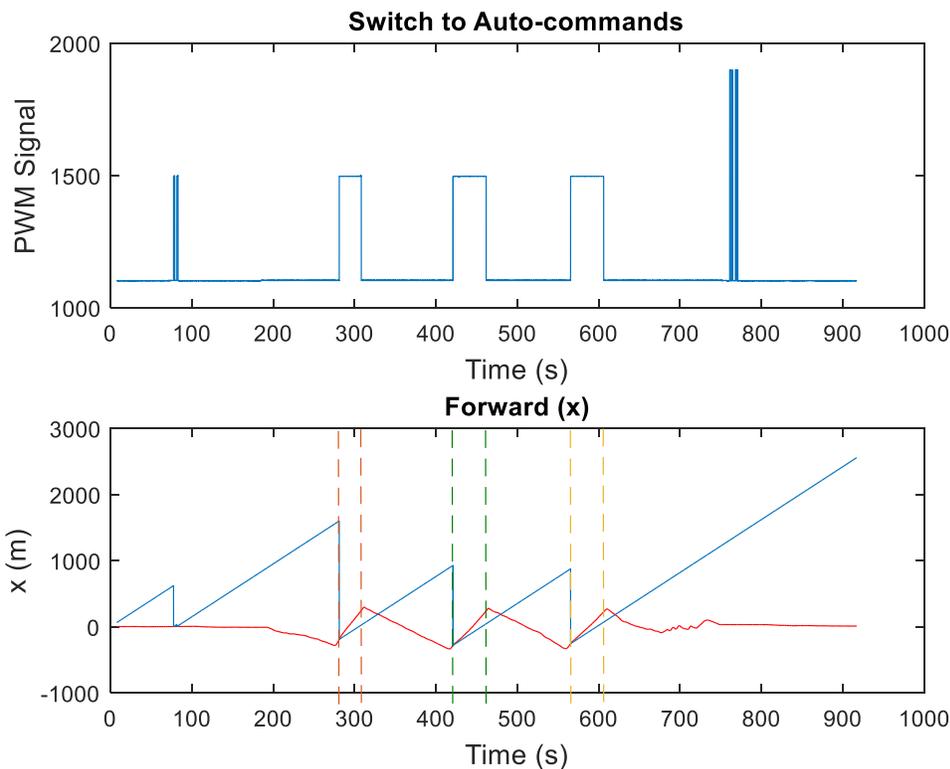
Figure 49 Flight Test: Forward Tracking in Tuning Phase
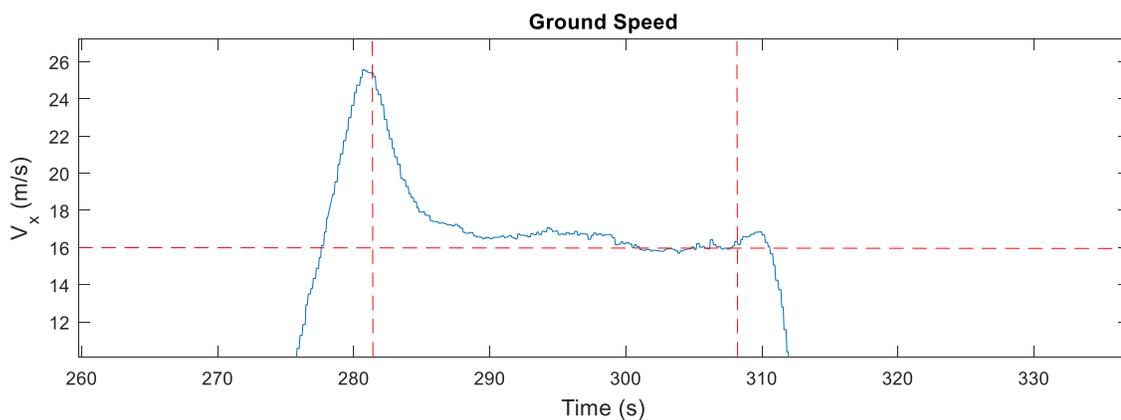
Figure 50 Flight Test: Segment of Forward

An penultimate test would include combining all three components tracking a trajectory such as the generic paths utilized in (Moncayo, et al., 2013) "figure-8" and an oval. This would further test the adequacy of the tuned parameters in the FFC controller.

4.7. Wind Measurement and Estimation

Aside from the control laws the UAS glider is required to have wind sensing technologies because to achieve *sailing* the aircraft must be oriented into a favorable configuration referred to as sailing conditions. Therefore, this study extends its focus into identifying and assessing various methods of attaining the wind velocity and direction in real-time either by estimation using the given the avionic components on-board the test-bed or by implementing an addition instrument. The two approaches investigated are as follows:

1. Estimation of wind parameters using an Extended Kalman Filter (EKF)

   - 3 different methods from (Rhudy, Gu, Gross, & Chao, 2017)

2. Direct measurement of angle of attack (alpha/α) and sideslip angle (beta/β)

   - M1: Mechanical Vanes

   - M2: Seven-Hole Air Data Boom (ADB)

Different algorithms were flight tested on a modified Skywalker 1880 (for further details see Appendix C) prior to implementation in the DAP glider. The RC airplane offers a low-cost system that is capable of satisfying the needs of the tests. These modifications include: a landing gear, pitot-static tube and a different motor i.e. Turnigy D3542/6 Brushless Motor (see Figure 51). However, the avionics and flight test software are similar to the glider.

Supplementary work on this chapter can be found in (Nshuti, Coulter, Festa,

Engblom, & Moncayo, 2018).

Figure 51 Modified Skywalker

4.7.1. EKF to Estimate Wind Parameters

The Extended Kalman Filter is used for non-linear discrete-time applications. The purpose of an EKF is that given the inputs, measured outputs and assumptions on the process and output noise then estimate unmeasured states and actual process outputs.
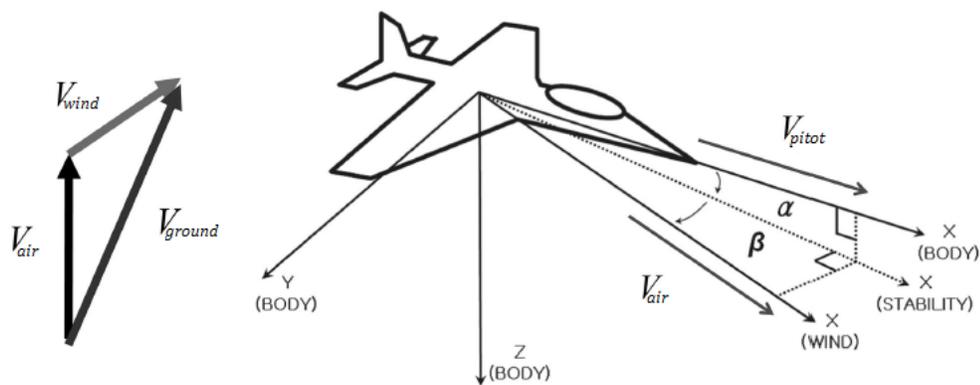
Figure 52 Wind Triangle and Airspeed definition (Cho, Kim, Lee, & Kee, 2011)

Where V_{wind} is wind velocity, V_{ground} is the ground velocity of an aircraft, V_{air} is

velocity of the aircraft relative to air, V_{pitot} is airspeed measured by a Pitot static tube.

(Rhudy, Gu, Gross, & Chao, 2017) presents comparisons of wind estimation techniques depending on what sensors are available on the UAS using a UKF. However, all methods used the wind triangle relationship, shown in Figure 52. The wind triangle relationship requires information on both ground speed and airspeed. Thus, all methods use GPS for velocity estimates and pitot-static tube for airspeed.

In this study, the wind parameter estimates were tested in-flight and then compared to values collected from the PX4 uORB block (described section 4.4) in and the measurements from ERAU Mobile UAS Ground Weather Station (4.5).

Table 14 defines the construction of the state space system for each method i.e. state vector **x**, input vector **u** and output vector **y**.

Table 14 EKF Formulations

Method	States	Input	Measurements
1	$\hat{x} = [u_w^n \ v_w^n \ w_w^n \ \zeta]^T$	$u = [V_N^{GPS} \ V_E^{GPS} \ V_D^{GPS}]^T$	$y = p_d$
2	$\hat{x} = [V_N \ V_E \ V_D \ u_w^n \ v_w^n \ w_w^n \ \zeta]^T$	$u = [a_x \ a_y \ a_z]^T$	$y = [V_N \ V_E \ V_D \ p_d]$
3	$\hat{x} = [u \ v \ w \ u_w^n \ v_w^n \ w_w^n]^T$	$u = [a_x \ a_y \ a_z \ p \ q \ r]^T$	$y = [V_N \ V_E \ V_D \ V_{pitot}]$

Where

$u_w^n \ v_w^n \ w_w^n$ are the wind velocities,

ζ is the scale factor, which is an accumulated parameter defining the effects of air density, angle of attack and angle of sideslip;

$V_N \ V_E \ V_D$ are the north, east and down components of ground speed from the GPS receiver;

p_d is the dynamic pressure measured from the pitot-static tube;

$a_x \, a_y \, a_z$ are the acceleration components of the aircraft;

$p \, q \, r$ roll, pitch and yaw rates, respectively

$u \, v \, w$ the estimates of airspeed in body frame

V_{pitot} airspeed from the pitot-static tube

Method 1: GPS Correction Factor based EKF

This method considers the estimation of north, east and down components of wind velocity u_w^n , v_w^n and w_w^n as well as a scale factor ζ, which is a collective parameter employed to estimate the effect of air density, angle of attack and sideslip angle.

The state dynamics for wind are described by random walk with zero-mean Gaussian process noise w vector with covariance $\boldsymbol{Q}$:

$$x_k = x_{k-1} + w_{k-1} \tag{4.1}$$

Using the wind triangle relationship, the output is determined as follows:

$$V_{air} = V_{ground} - V_{wind} \tag{4.2}$$

Taking the square of the L$_2$ norm of the air, ground and wind velocity vectors which are expressed in the NED reference frame.

$$V_{air}^2 = (V_N^{GPS} - u_w^n)^2 + (V_E^{GPS} - v_w^n)^2 + (V_D^{GPS} - w_w^n)^2 \tag{4.3}$$

The airspeed from the pitot-tube can be expressed in terms of total airspeed V_{air}:

$$V_{pitot} = V_{air} \cos \alpha \cos \beta \tag{4.4}$$

where α is angle of attack and β is sideslip angle. Bernoulli's equation gives:

$$p_d = \frac{\rho}{2} V_{pitot}^2 \tag{4.5}$$

where ρ is the density of air. Thus the scale factor is defined as follows:

$$\zeta = \frac{\rho}{2} \cos^2 \alpha \cos^2 \beta \tag{4.6}$$

The output equation:

$$y = p_d = \zeta[(V_N^{GPS} - u_w^n)^2 + (V_E^{GPS} - v_w^n)^2 + (V_D^{GPS} - w_w^n)^2] + v_k \qquad (4.7)$$

where v is the zero-mean Gaussian measurement noise vector with variance $\boldsymbol{R}$.

Method 2: GPS + IMU based EKF

Method 2 is based on (Rhudy et al, 2017) formulation #3. However, the flight software includes another KF for attitude estimation, therefore Euler attitude angle and rates are not included here. This method expands on Method 1 by including information from the IMU. Thus, 3-DOF of ground speed can be estimated as states instead of inputs to the state space system. By converting the body-axis accelerations of the aircraft to Earth frame using the Direct Cosine Matrix (DCM) and adding gravity to the third component:

$$\begin{bmatrix} \dot{V}_N \\ \dot{V}_E \\ \dot{V}_D \end{bmatrix} = \textbf{DCM}(\phi, \theta, \psi)\left(\begin{bmatrix} a_x \\ a_y \\ a_z \end{bmatrix} + w^a\right) - \begin{bmatrix} 0 \\ 0 \\ g \end{bmatrix} \qquad (4.8)$$

where ϕ, θ, ψ are roll, pitch and yaw Euler angles, while w^a is accelerometer Gaussian noise with zero-mean and the DCM is given by:

$$\textbf{DCM}(\phi, \theta, \psi) = \begin{bmatrix} \cos\theta\cos\psi & -\cos\phi\sin\psi + \sin\phi\sin\theta\cos\psi & \sin\phi\sin\psi + \cos\phi\sin\theta\cos\psi \\ \cos\theta\sin\psi & \cos\phi\cos\psi + \sin\phi\sin\theta\sin\psi & -\sin\phi\cos\psi + \cos\phi\sin\theta\sin\psi \\ -\sin\theta & \sin\phi\cos\theta & \cos\phi\cos\theta \end{bmatrix}$$

$$(4.9)$$

The dynamics of the wind states are modeled as in equation (4.1). The output equation is partially given by (4.7) and:

$$\begin{bmatrix} V_N \\ V_E \\ V_D \end{bmatrix} = \begin{bmatrix} V_N^{GPS} \\ V_E^{GPS} \\ V_D^{GPS} \end{bmatrix} + v^{GPS} \qquad (4.10)$$

where v^{GPS} is the Gaussian measurement noise with zero-mean and covariance $\boldsymbol{R}$

from GPS estimates. This method helps to smooth abrupt changes from GPS sensor.

Method 3: Linear Velocities based EKF

Method 3 is based on (Rhudy et al, 2017) formulation #4, except the bias parameters are not included because a separate KF is used on the data from the IMU sensor. Furthermore, α and β are not included in the measurements however for a future study wind vanes or ADB may be added to the UAS. This method expands on the previous two by including V_{pitot} airspeed from the pitot-static tube as an additional measurement. Thus, neither the scale factor ζ is required nor the ground speeds as in GPS and IMU based KF.

The state dynamics of the body-axis velocity states are formulated as:

$$\begin{bmatrix} \dot{u} \\ \dot{v} \\ \dot{w} \end{bmatrix} = \begin{bmatrix} 0 & -w & v \\ w & 0 & -u \\ -v & u & 0 \end{bmatrix} \left(\begin{bmatrix} p \\ q \\ r \end{bmatrix} + w^w \right) + DCM(\phi,\theta,\psi)^T \begin{bmatrix} 0 \\ 0 \\ g \end{bmatrix} + \begin{bmatrix} a_x \\ a_y \\ a_z \end{bmatrix} + w^a \quad (4.11)$$

where w^a angular rate error. The dynamics of the wind states are modeled as in equation (4.1). For the output equation, the body-axis velocities can be rotated into Earth reference frame and corrected for wind:

$$\begin{bmatrix} V_N^{GPS} \\ V_E^{GPS} \\ V_D^{GPS} \end{bmatrix} = DCM(\phi,\theta,\psi) \begin{bmatrix} u \\ v \\ w \end{bmatrix} + \begin{bmatrix} u_w^n \\ v_w^n \\ w_w^n \end{bmatrix} + v^{GPS} \quad (4.12)$$

Since the pitot-tube is mounted along the longitudinal axis (as shown in Figure 51), airspeed is measured in the body *x*-axis, thus output equation:

$$V_{pitot} = u + v^{pitot} \quad (4.13)$$

where v^{pitot} is the Gaussian measurement noise from the pitot-static tube with zero mean and covariance $\boldsymbol{R}$.

EKF Wind Estimation Results

For this section, data from the FDCRL's Ground Control Station's Weather Station was used. Details on the GCS and its weather station are provided in Section (4.5).

Upon analyzing an example of flight test data, Method 2 (using 6 states) and Method 3 (using 7 states) were noticeably yielding the better results. Results plotting Method 2 and 3 compared to the GCS weather station are shown in Figure 53.

Both methods 2 (in red) and 3 (in blue) appear to follow a similar trend to the weather station reference (in yellow). Take note that between 0-20 s and 90-100 s are take-off and landing phases of flight.

The difference between these and the weather station reference comes from the fact that the weather station measured the wind parameters at 7 meters above the ground whereas the UAS flies at about 150 m. Though it is possible to find the same wind speed despite the difference in altitude, the same cannot be said concerning the wind direction. This may explain the discrepancy between the reference and the EKF outputs.
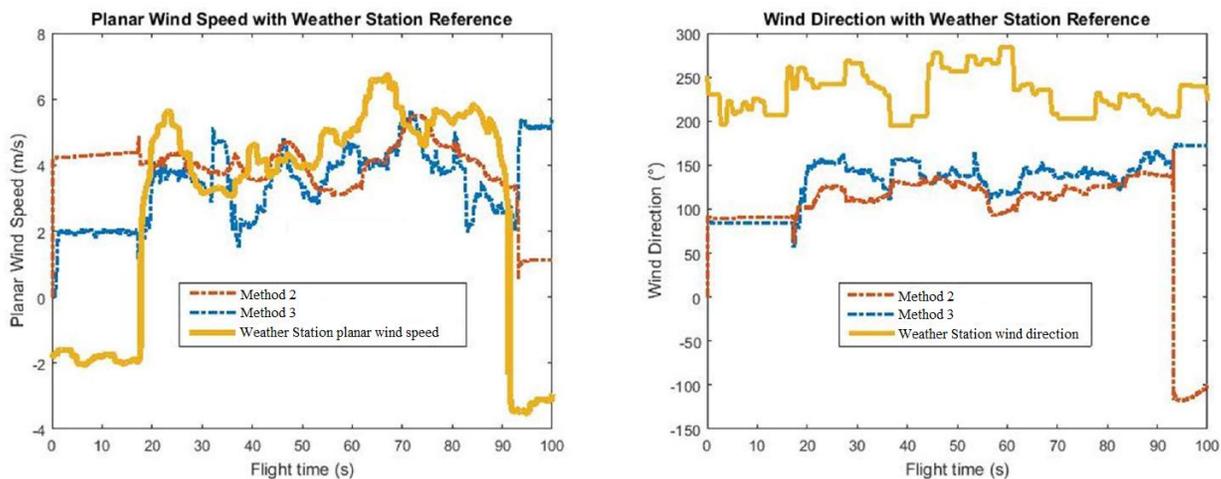
Figure 53 Wind Parameters vs Weather Station Data

The fact that both EKF results are close was a sign that the results were promising. For this reason, the weather station was not used as a reference for future flight tests. This led to the implementation and study with vanes and ADB.

4.7.2. Angle of Attack and Sideslip Angle Measurement

Among the suggestions of (Rhudy, Gu, Gross, & Chao, 2017), it includes a direct measurement of angle of attack and sideslip angle via weather vanes. A novel concept that was originally presented in (Rhudy, Larrabee, Chao, Gu, & Napolitano, 2013). The results showed that the wind trends were better captured with the inclusion of angle of attack and sideslip angle measurements which means producing superior wind estimates when compared to weather station data.

Weather Vanes

Weather vanes offer a direct measurement of angle of attack and sideslip angle. It provides measurements of the relative flow angles of the UAS which are related to the airspeed.

The weather vanes used for this test were in-house 3D printed components with high resolution attached to potentiometers. In a previous investigation measurement errors were attributed to friction from the potentiometers. Therefore, frictionless potentiometers where chosen: Bourns' 6538S frictionless potentiometers (10 kOhm resistance and ±10% tolerance). Two potentiometers are used, one for angle of attack and the other for sideslip angle shown in Figure 54.
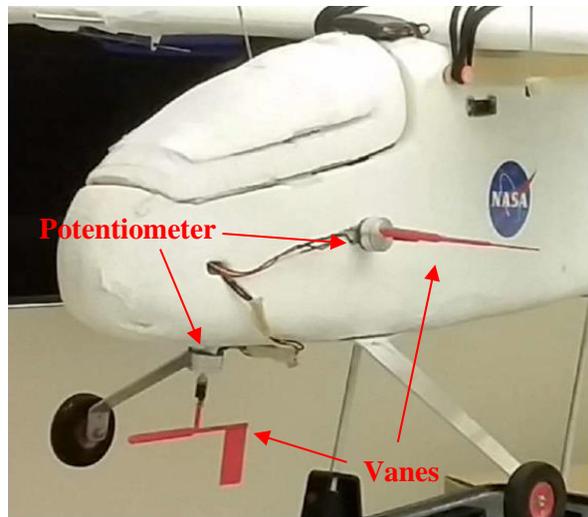
Figure 54 Vanes and potentiometers on Skywalker

Prior to implementing the EKF estimation, preliminary flight tests were performed to test the correctness of the vanes at no wind conditions, because pitch and angle of attack are close at zero wind. This is demonstrated in Figure 55.
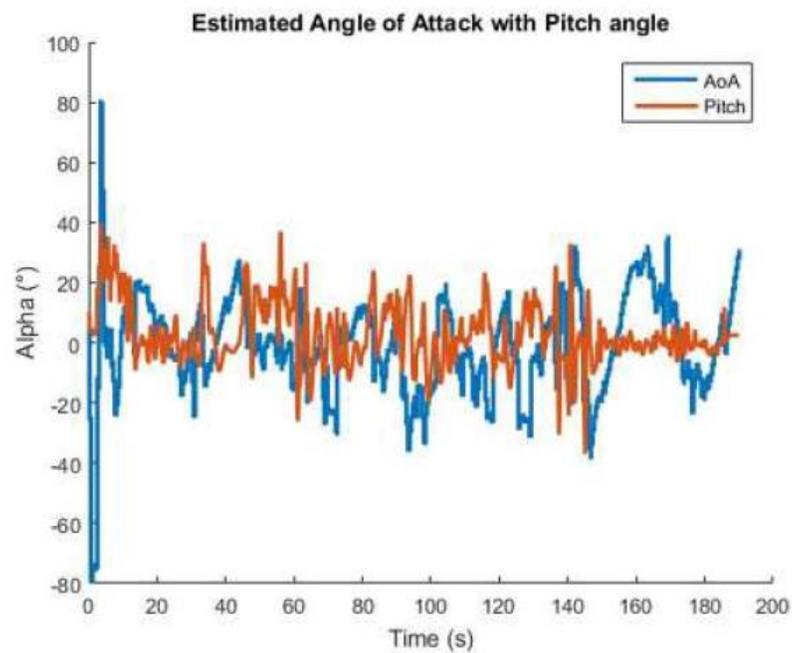
Figure 55 Angle of attack (AoA) vs Pitch angle

Figure 55 illustrates that the vanes attempt to have the same trend as the pitch but with low accuracy. Inconsequentially, other flight tests were performed implementing the EKF methods to compare the vanes as demonstrated in Figure 56:
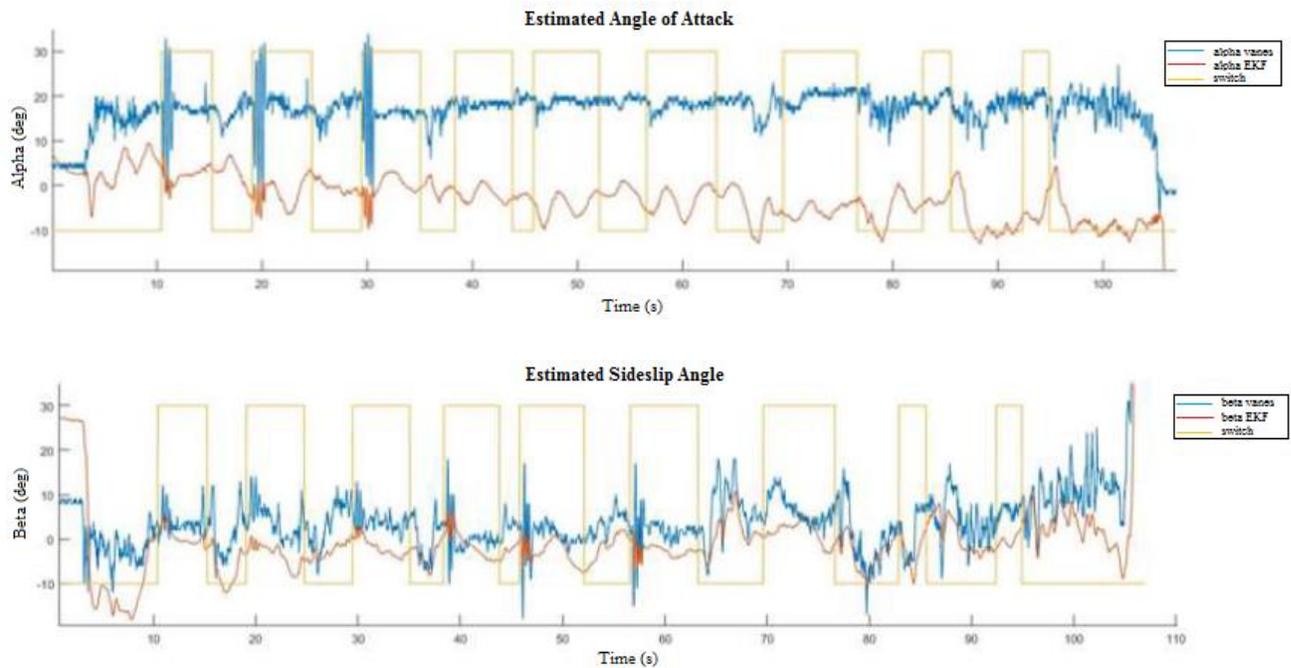
Figure 56 Alpha-vane vs. Alpha-EKF (top) and Beta-vane vs Beta-EKF (bottom)

The potentiometer plots are in blue, the EKF plots are in orange. One square on the yellow plot represents the beginning and end of maneuvers. The RC pilot performed different sets of maneuvers such as elevator doublets and rudder doublets during the flight. Doublet maneuvers are injected onto a control surface to excite the UAS dynamics. These are two-sided pulses, usually with each pulse being symmetric in amplitude and duration.

The results show a large discrepancy in angle of attack, possibly due to the lack of wind measurement data in the down axis. A better tracking estimation performance was acquired for sideslip angle. However, for both angles the wind vanes displayed a low resolution in their ability to capture high frequency dynamics.

Seven-Hole Probe

To design the 7-hole airdata probe this research was based on the work presented in (Zilliac, 1989). This led to a non-nulling, conical-ended 7-hole probe which was built in-house. The probe tip contains seven pressure ports, one of which sits at the tip of the cone, with the remaining six arranged in a ring downstream, see Figure 57.
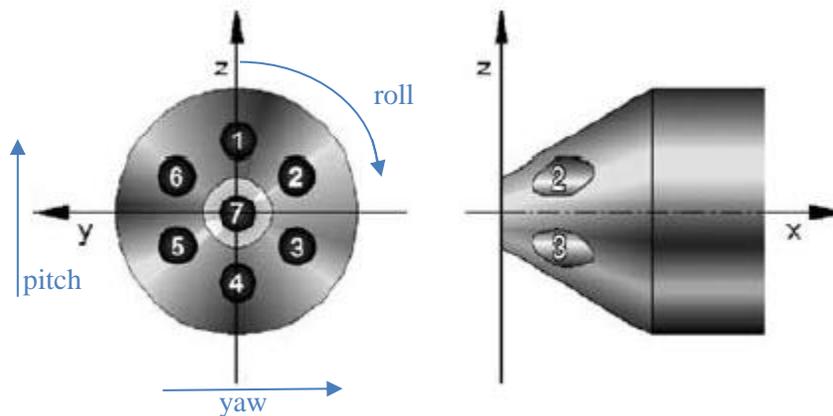
Figure 57 Stem of 7-hole probe

The coefficient equations are different for different angles of attack. At low angles, the flow remains attached over the probe tip. Under such conditions, greater probe sensitivity can be gained by using pressures measured by all seven ports (Zilliac, 1989). As the angle increases for high angles of attack, the flow on the downwind or upwind side (depending on direction) of the probe eventually separates. The pressure data from the region of separated flow is not steady and does not represent the flow that is measured (Crawford, 2011). For this reason, the low angle regime i.e. where the flow is attached over all seven pressure ports is considered for this study.

Low Angle Coefficients

In low angle flow, the highest pressure is read in port 7, P_7. Thus P_7 has approximately the total flow pressure. Since it is assumed that the flow does not separate, the approximate static pressure can be found:

$$\bar{P} = \frac{1}{6}(P_1 + P_2 + P_3 + P_4 + P_5 + P_6)$$

(4.14)

Velocity-invariant pressure coefficients can be calculated using equations normalized by the dynamic pressure of the flow:

$$C_{P_{t_a}} = \frac{P_4 - P_1}{P_7 - \bar{P}} \qquad C_{P_{t_b}} = \frac{P_3 - P_6}{P_7 - \bar{P}} \qquad C_{P_{t_c}} = \frac{P_2 - P_5}{P_7 - \bar{P}}$$

(4.15)

Based on the linear combination of the directional pressure coefficients, the coefficients that represent pitch and yaw as described in Figure 57 are given by:

$$C_{P_{\alpha_7}} = C_{P_{t_a}} + \frac{C_{P_{t_b}} - C_{P_{t_c}}}{2}$$

(4.16)

$$C_{P_{\beta_7}} = \frac{1}{\sqrt{3}}\left(C_{P_{t_b}} + C_{P_{t_c}}\right)$$

(4.17)

The total and static pressure coefficients are given by:

$$C_{P_{total_7}} = \frac{P_7 - P_{total}}{P_7 - \bar{P}} \qquad C_{P_{static_7}} = \frac{\bar{P} - P_{static}}{P_7 - \bar{P}}$$

(4.18)

Seven-Hole Air Data Boom Calibration

The seven-hole probe was built in-house using stainless steel, because of its resistance to corrosion, heat damage and low weight. The probe is 12 in in length with 0.25 in total radius. The ADB calibration was performed using ERAU wind tunnel. Details of the test components are provided in Table 15 and a placement map is shown in Figure 58:

Table 15 ADB Test Components

Components	Purpose
APM 2.6	Low-cost onboard flight computer. Using the APM2 Simulink Blockset, a code was developed that moves the servos and logs data on flash memory.
Servos	To position the probe in different combinations of alpha and beta.
Pitot-Static	To measure static pressure
0.15 psi differential pressure sensors by Merit Sensor	7 pressure sensors for each port on the ADB
NiMH 4.8 V 2A	Power supply
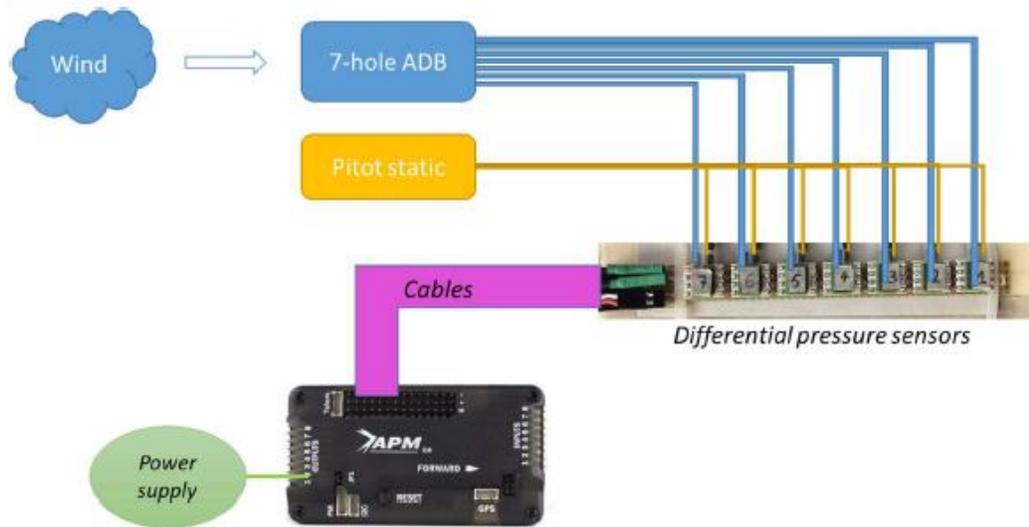
Figure 58 ADB Placement Map

During the calibration process, the probe is submitted to a set of very well characterized incoming flows inside a wind tunnel with the provenience direction defined by the values of two angles. A MATLAB/Simulink code is built on the APM 2.6 to provide

timed commands to move the servos in predetermined orientations of angle of attack and sideslip angle. The ADB is placed in the wind tunnel to collect data for known varying wind speeds. Figure 59 shows test rig built for the wind tunnel calibrations.
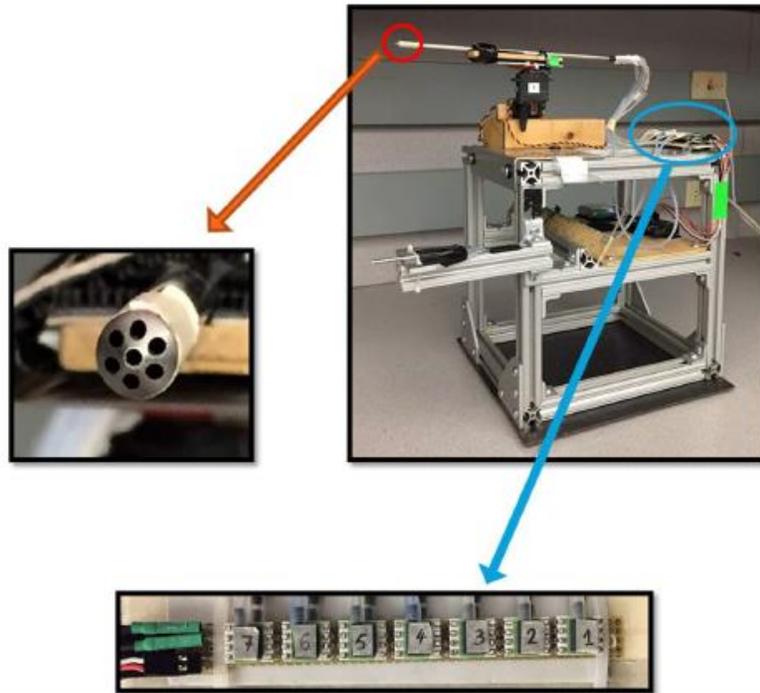
Figure 59 ADB Wind Tunnel Setup

The onboard computer commands the servos to move from -25° to 25° in increments of 5° for both alpha and beta. The wind speeds tested were: 10 m/s, 15 m/s, 20 m/s and 25 m/s. The data collected is then post-processed and analyzed using MATLAB. Figure 60 shows a sample of the post-processing data at wind speed 20 m/s. The top 2 plots show the average coefficient pressure (left) and total pressure at P_7 (right). The bottom 2 plots show the angle of attack (left) and sideslip (right) measured.
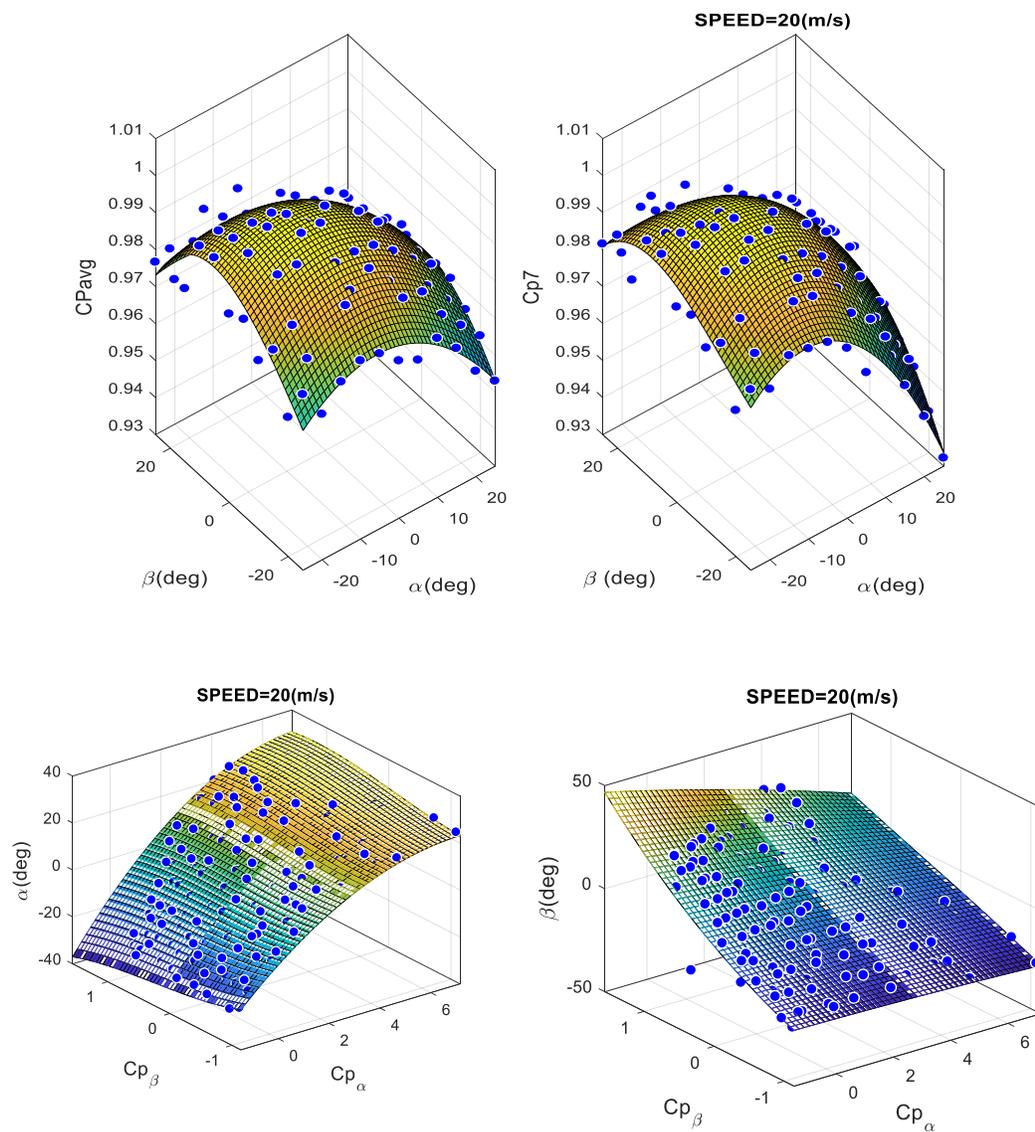
Figure 60 ADB Wind Tunnel Calibration at 20 m/s

Flight Testing with ADB

The ADB was mounted in the nose of the Skywalker UAS to measure angle of attack and sideslip angle to capture the local environment as shown in Figure 61.
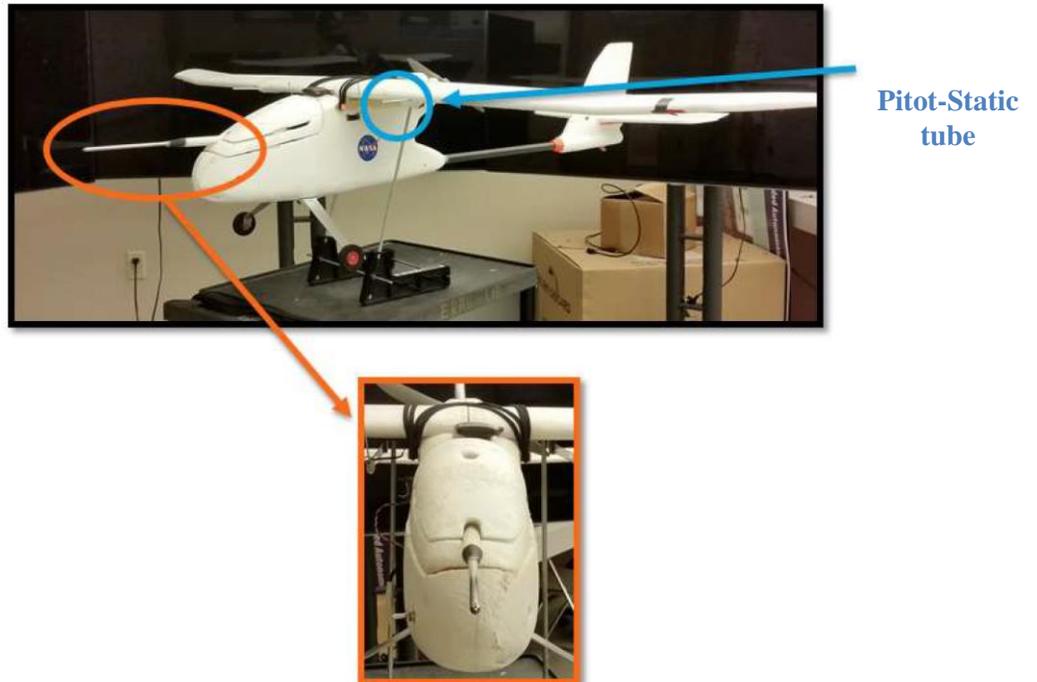
Figure 61 ADB mounted on Skywalker III
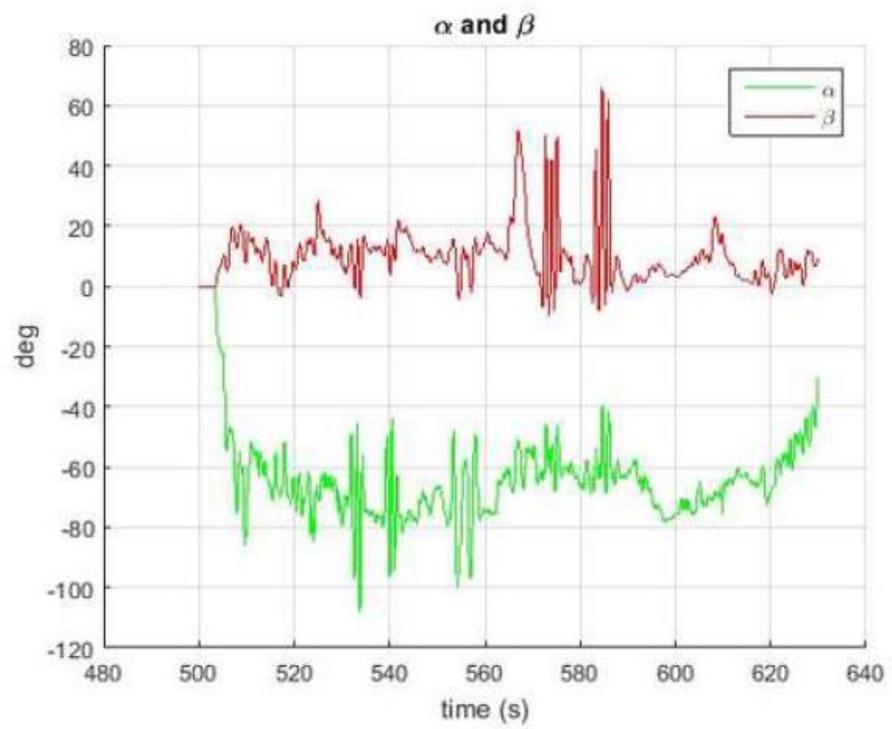
Figure 62 ADB Flight Test Data

During the flight test, the ADB was mounted with a 40° bias in alpha instead of being leveled because landing gear was not accounted for. The results are illustrated in Figure 62, despite the mounting bias, the ADB was capable of capturing alpha and beta with good resolution. At ~530s and 540s the pilot performed elevator doublets, these are clearly attained because the excitation is captured i.e. the pitch up and pitch down from the maneuver. Furthermore, sideslip angle shows at ~570s and 585s the rudder doublets are also clearly captured. Note that the frequency associated with the doublet maneuver is unknown, thus these results assume the accurate capture of pilot input. Therefore, the trends of angle of attack and sideslip angle using the air-data probe are promising because they register the effect and they are sensitive to the maneuver. However, the results do not prove accuracy but prove that the probe responds and follow-on work can be pursued to improve the accuracy. The inaccuracies maybe due to imprecisions in the wind tunnel and/or noisy pressure sensors.

In conclusion, this study implemented a number of methods to determine wind parameters, i.e. wind estimation and direct measurement. For wind estimation, the results showed that the increased number of measured states improve the wind speed and wind direction apprehended when compared to the ground control weather station. Although, it was concluded that the GCS did not provide a fair comparison during flight tests because the weather station is mounted at 7m above the ground while the Skywalker is flying 150m above ground. For direct measurement of wind parameters, the angle of attack and sideslip angle were evaluated using wind vanes and seven-hole air-data probe. The results show a low accuracy in the measurements from the vanes as compared to the EKF methods. Results from the multi-hole probe, showed that both angle of attack and sideslip angle were

captured relative to the maneuver being performed by the RC pilot, i.e. elevator doublets and rudder doublets, respectively. Finally, to further this work the air-data boom can be improved for accuracy and it can provide additional states to enhance wind estimation. Therefore, it could be installed on the DAP glider.

CHAPTER 5: Conclusion & Recommendations

This UAS research effort has evolved as an integral part to support the proof-of-concept of DAP, a novel approach to utilizing and implementing atmospheric satellites at a low-cost with the ability to station-keep for years at a time, using wind shears and requiring no propulsion. The DAP concept presents an unprecedented dynamic and control problem which requires the development of novel flight control laws. This study designs said control laws, as well as develops a simulation environment and a research test-bed for testing these control laws.

To simplify the problem, the *BOARD* aircraft was replaced with a Truck model for both simulation and flight testing. The *SAIL* UAS is required to maintain sailing conditions and sustain the appropriate configuration so that there is constant tension in the cable, thus creating a situation where propulsion is not required. The study implemented and analyzed the $\mathcal{L}_1$ adaptive control laws to enhance the performance of the UAS. And performed a comparison study between a PID controller and $\mathcal{L}_1$ adaptive controller. In general, the adaptive augmentation performed better than the PID especially in non-ideal environmental conditions.

A UAS research test-bed was developed using subscale gliders of 4m wing span and flying below 500ft. Results from manual flight tests showed that the RC pilot was incapable of putting the UAS into a sailing mode because there was no way for the pilot to 'feel' the aircraft. This led to an investigation into autonomous flight, a FF based controller was implemented that tracks components in lateral, forward and vertical. These components were tuned separately during flight tests. It is recommended that in future all three components are integrated together and required to follow a trajectory such as a

'figure 8'.

To achieve the DAP concept, wind conditions are integral part of formulating sailing conditions. Therefore, a study was performed evaluating various wind estimation techniques, that may be implemented on-board the UAS platform. The results showed that the airdata probe was capable of capturing doublet maneuvers with good resolution, relative to the weather vanes. In future, adding the angle of attack and sideslip angle measurements from the probe to estimation, EKF Method #3 would potentially provide enhanced accuracy in the wind speed and wind direction values.

Additional future recommendations include implementation of $\mathcal{L}_1$ adaptive control on the UAS. Utilizing the ADB to perform a system identification that can enhance the Vortex Lattice Method model that generated this simulation. This would increase options of investigating various control laws such as using additional nonlinear controllers that can be applied such as the Nonlinear Dynamic Inversion (NLDI), which could be supplementary to the current control architecture by placing it in the Outer-loop. As well implementing the characterized propulsion subsystem into the thrust model of the simulation.

REFERENCES

Andersen, D., & Haley, D. (1993, September 17). *NASA Tests New Laser Air Data System on SR-71 Blackbird*. Retrieved from NASA : http://www.nasa-usa.de/home/hqnews/1993/93-163.txt

Arain, B., & Kendoul, F. (2014). Real-time wind speed estimation and compensation for improved flight. *IEEE Transactions on Aerospace and Electronic Systems, vol. 50, no. 2*, pp. 1599-1606.

Azinheira, J. R., Paivab, D. E., Ramos, J. G., & Bueno, S. S. (April 2000). Mission Path Following for an Autonomous Unmanned Airship. *IEEE International Conference on Robotics and Automation*, (pp. pp. 1269-1275.). San Francisco, CA.

Beard, R., & McLain, T. (2012). Small Unmanned Aircraft: Theory and Practice. *Princeton University Press*, Princeton, NJ.

Beard, R., Kingston, D., Quigley, M., Snyder, D., Christiansen, R., Johnson, W., . . . Goodrich, M. A. (2005). Autonomous Vehicle Technologies for Small Fixed-Wing UAVs. *AIAA Journal of Aerospace Computing, Information, and Communications. Volume 2. Issue 1*, pp. 92-108.

Bleicher, A. (2013, December 31). *Introducing Solara, the Atmospheric Satellite - IEEE Spectrum*. Retrieved from IEEE Spectrum: https://spectrum.ieee.org/aerospace/aviation/introducing-solara-the-atmospheric-satellite

Boyle, A. (2016, June 9). *Boeing tries again for long-flying solar plane*. Retrieved from GeekWire - Breaking News in Technology and Business: https://www.geekwire.com/2016/boeing-tries-design-solar-airplane-stay-aloft-years/

Bryer, D. W. (1971). Pressure-probe methods for determining wind speed and flow direction. London: Her Majesty's Stationary Office.

Campa, G., Napolitano, M. R., Seanor, B., & Perhinschi, M. G. (2004). Design of Control Laws for Maneuvered Formation Flight. *American Control Conference.*

Cao, C., & Hovakimyan, N. (2006a). Design and analysis of a novel L1 adaptive control architecture, Part I: Control signal and asymptotic stability. *American Control Conference*, (pp. pp. 3397-3408). Minneapolis, MN.

Cao, C., & Hovakimyan, N. (2006b). Design and analysis of a novel L1 adaptive control architecture, Part II: Guaranteed transient performance. *American Control Conference*, (pp. pp. 3403–3408). Minneapolis, MN.

Cao, C., & Hovakimyan, N. (2007a). Stability Margins of L1 Adaptive Control Architecture. *American Control Conference*, pp. 3931–3936.

Cao, C., & Hovakimyan, N. (2007b). L1 Adaptive Controller for Systems in the Presence of Unmodeled Actuator Dynamics. *IEEE Conference on Decision and Control, 2007*, pp. 891–896.

Cao, C., & Hovakimyan, N. (2007c). Guaranteed Transient Performance with L1 Adaptive Controller for Systems with Unknown Time-Varying Parameters and Bounded Disturbances: Part I. *Amercian Control Conference*, pp. 3925–3930.

Cao, C., & Hovakimyan, N. (2008a). Design and Analysis of a Novel L1 Adaptive Control Architecture with Guaranteed Transient Performance. *IEEE Transactions on Automatic Control, Vol. 53, No. 3*, pp. 586–591.

Cao, C., & Hovakimyan, N. (2008b). L1 Adaptive Output Feedback Controller for Systems of Unknown Dimension. *IEEE Transactions on Automatic Control, Vol. 53, No. 3*, pp. 815–821.

Cao, C., & Hovakimyan, N. (2008c). L1 Adaptive Output Feedback Controller for Systems of Unknown Dimension. *IEEE Transactions on Automatic Control*, vol. 53, no. 3, pp. 815-821.

Cao, C., & Hovakimyan, N. (2009). L1 adaptive output-feedback controller for non-stricly-positive-real reference systems: Missile longitudinal autopilot design. *AIAA Journal of Guidance, Control, and Dynamics*, pp. 717–726.

Chilali, M., & Gahinet, P. (1996). H∞ design with pole placement constraints: an LMI approach. *Automatic Control. IEEE Transactions. Volume 41. Issue 3*, pp.358-367.

Cho, A., Kang, Y. S., Park, B. J., & Yoo, C. S. (2013). Airflow angle and wind estimation using GPS/INS navigation data and airspeed. *13th Int. Conf. Control, Automation and Systems (ICCAS).* Gwangju, Korea.

Cho, A., Kim, J., Lee, S., & Kee, C. (2011). Wind estimation and airspeed calibration using a UAV with a single-antenna GPS receiver and pitot tube. *IEEE Trans. Aerosp. Electron. Syst., vol. 47, no. 1*, pp. 109–117.

Coulter, N., Moncayo, H., & Engblom, W. (2018a). Virtual Demonstration of a Novel Stratospheric Dual Aircraft Platform Concept. *AIAA Modeling and Simulation Technologies Conference*.

Coulter, N., Moncayo, H., & Engblom, W. (2018b). Evaluation and Comparison of Sailing Flight Optimization Algorithms for a Stratospheric Dual Aircraft Platform Concept. *AIAA Modeling and Simulation Technologies Conference.* AIAA.

Crawford, J. D. (2011). *Design and Calibration of Seven Hole Probes for Flow Measurement.* Kingston, Ontario, Canada: A theis submitted to the Department of Mechanical and Materials Engineering at Queen's University.

Engblom, W. (2014). Development of Atmospheric Satellite Concept based on Sailing. *Applied Aerodynamics Proceedings.* AIAA.

Engblom, W. A. (2015). *Palm Coast, FL, US Patent No. 8,931,727 B2.*

Engblom, W. A., Decker, R. K., Moncayo, H. Y., Barott, W. C., Sanchez, E. L., & Giovagnoli, A. A. (2016). *Virtual Flight Demonstration of the Stratospheric Dual-Aircraft Platform.* NIAC Phase I Report.

Engblom, W., & Decker, R. (2016). Virtual Flight Demonstration of the Stratospheric

Dual-Aircraft Platform. *Applied Aerodynamics Conference.* AIAA SciTech.

Franko, S. (2009). LQR-Based Trajectory Control of Full Envelope, Autonomous Helicopter. *World Congress on Engineering.* London.

Gallagher, S. (2013, August 18). *Almost orbital, solar-powered drone offered as "atmospheric satellite" | Ars Technica*. Retrieved from Ars Technica: https://arstechnica.com/information-technology/2013/08/almost-orbital-solar-powered-drone-offered-as-atmospheric-satellite/

Gregory, I., Xargay, E., Cao, C., & Hovakimyan, N. (2010). Flight Test of an L1 Adaptive Controller on the NASA AirSTAR Flight Test Vehicle. *AIAA Guidance, Navigation, and Control Conference.* Canada.

Hajiyev, C., & S., V. (2013). LQR Controller with Kalman Estimator Applied to UAV. *Longitudinal Dynamics (Volume 4, Issue 1)*, pp. 36-41.

Hovakimyan, N., & Cao, C. (2010). *L1 Adaptive Control Theory.* Philadelphia, PA: Society for Industrial and Applied Mathematics.

Hovakimyan, N., & Cao, C. (2010). *L1 Adaptive Control Theory: Guaranteed Robustness with Fast Adaptation.* Philadelphia, PA: SIAM, ISBN: 0898-71704-3, Series: Advances in Design and Control.

Jun, L., & Yuntang, L. (2011). Dynamic analysis and PID control for a quadrotor. *Mechatronics and Automation (ICMA)*, (p. pp.573.578).

Kada, B., & Ghazzawi, Y. (2011). Robust PID Controller Design for an UAV Flight Control System. *World Congress on Engineering and Computer Science. Volume 2*, (pp. 945-950). San Francisco, USA.

Kharisov, E. (2013). *L1 Adaptive Output-Feedback Control Architectures.* Urbana-Champaign: University of Illinois, PHD Dissertations at Urbana-Champaign.

Kinoshita, T., & Imado, F. (2006). A Study on the Optimal Flight Control for an Autonomous UAV. *Mechatronics Automation, IEEE International Conference*, (p. pp.996.1001).

Krishnamoorthy, K. (2015). *Fault Tolerance Analysis of L1 Adaptive Control System for Unmanned Aerial Vehicles.* West Virginia University: ProQuest Dissertations Publishing.

Kumon, M., Mizumoto, I., & Iwai, Z. (2005). Wind estimation by unmanned air vehicle with delta wing. *IEEE Int. Conf. Robot. Autom., Barcelona, Spain*, pp. 1896–1901.

Laurence, R. J., & Argrow, B. M. (2017). Flight Results from a Small UAS Distributed Flush Airdata System. *9th AIAA Atmospheric and Space Environments Conference, AIAA Aviation* (pp. pp. (AIAA 2017-4476)). Denver, CO: [Available online at https://doi.org/10.2514/].

Laurence, R. J., Argrow, B. M., & Frew, E. W. (2016). Development of Wind Sensing from Small UAS with Distributed Pressure Sensors. *8th AIAA Atmospheric and Space Environments Conference, AIAA Aviation* (pp. pp. (AIAA 2017-4199)).

Washington, DC: [Available online at http://dx.doi.org/10.2514/6.2016-4199].

Lee, J. H., Sevil, H. E., Dogan, A., & Hullender, D. (2013). Estimation of maneuvering aircraft states and time-varying wind with turbulence. *Aerospace Science Technologies*, vol. 31, pp. 87–98.

Lefas, C. C. (1987). 43. Real-time wind estimation and tracking with transponder downlinked airspeed and heading data. *IEEE Trans. Aerosp. Electron. Syst., vol. AES-23, no. 2*, pp. 169–174.

Masar, I., & Stohr, E. (2011). Gain-scheduled LQR-control for an Autonomous Airship. *18th International Conference on Process Control*, (pp. pp.197-204). Tatranská Lomnica, Slovakia.

McLaren, S. (2008). *Velocity estimate following air data system failure.* OH, USA: M.S. thesis, Air Force Institute of Technology, Wright Patterson Air Force Base.

Mehdi, S. B. (2012). *Simulink Toolbox for L1 Adaptive Control.* UIUC Dissertation.

Moncayo, H., Krishnamoorty, K., Wilburn, B., Wilburn, J., Perhinschi, M., & Lyons, B. (2013). Performance Analysis of Fault Tolerant UAV Baseline Control Laws with L1 Adaptive Augmentation. *Journal of Modeling, Simulation, Identification, and Control*.

Nshuti, C., Coulter, N., Festa, D., Engblom, W., & Moncayo, H. (2018). Modeling, Simulation and Flight Testing to Support Proof of a Stratospheric Dual Aircraft Platform Concept. *AIAA SciTech Conference.* Kissimmee, FL: AIAA.

Oner, K. T., Ertugrul, C., Efe, S., Cevdet, H., Taylan, A., & Mustafa, U. (2009). LQR and SMC Stabilization of a New Unmanned Aerial Vehicle. *World Academy of Science, Engineering & Technology*, 373-378.

Perhinschi, M. G. (1997). A Modified Genetic Algorithm for the Design of Autonomous Helicopter Control System. *AIAA Guidance, Navigation and Control Conference*, (pp. pp. 1111-1120). New Orleans, USA.

Pfeifer, E., & Kassab, F. (2012). Dynamic Feedback Controller of an Unmanned Aerial Vehicle. *Robotics Symposium and Latin American Robotics Symposium (SBR-LARS)*, (pp. pp.261-266).

Pilot Engineering Group, M. (2015, November 25). *Pixhawk Pilot Support Package (PSP)*. Retrieved from https://www.mathworks.com/hardwaresupport/

Quindlen, J., & Langelaan, J. (2013). Flush Air Data Sensing for Soaring-Capable UAVs. *51st AIAA Aerospace Sciences Meeting.*

Rhudy, M. B., Larrabee, T., Chao, H., Gu, Y., & Napolitano, M. (2013). UAV Attitude, Heading, and Wind Estimation Using GPS/INS and an Air Data System. *AIAA Guidance, Navigation, and Control (GNC) Conference.*

Rhudy, M., Gu, Y., Gross, J., & Chao, H. (2017). Onboard Wind Velocity Estimation Comparison for Unmanned Aircraft Systems. *IEEE Transactions on Aerospace and Electronic Systems, Vol 53., No. 1*, (pp. pp. 55-66).

Salih, A. L., Moghavvemi, M., Mohamed, H. A., & Gaeid, K. S. (2010). Flight PID

Controller Design for a UAV Quadrotor. *Scientific Research and Essays 5.23* , 3660-3667.

Samy, I., Postlethwaite, I., Gu, D., & Green, J. (2010). Neural-Network-Based Flush Air Data Sensing System Demonstrated on a Mini Air Vehicle. *Journal of Aircraft, Vol. 47, No. 1*, pp. 18-31.

Sechrist, G. (2002, October 30). *Illumin - Dynamic Soaring*. Retrieved from Illumin - Volume XVIII Issue I: http://illumin.usc.edu/189/dynamic-soaring/

Sukamar, P., & Selig, M. (2013). Dynamic Soaring of Sailplanes over Open Fields. *Journal of Aircraft (Volume 50)*, DOI: 10.2514/1.C031940.

Sung, K. H., & Yoonsu, N. (2003). Stable fuzzy control system design with pole-placement constraint: an LMI approach. *Computers in Industry. Volume 51. Issue 1*, 1-11.

Ting, E., & Ayoubi, M. A. (2012). An Optimal Fuzzy-PID Controller for Aircraft Pitch Control. *Infotech@Aerospace Conferences* .

Whitmore, S. A. (1991). Development of a Pneumatic High-Angle-of-Attack Flush Airdata Sensing (HI-FADS) System. *NASA Technical Memorandum 104241*.

Wilburn, B., Perhinschi, M. G., Moncayo, H., Karas, O., & Wilburn, J. (2013). Unmanned Aerial Vehicle Trajectory Tracking Algorithm Comparison. *International Journal of Intelligent Unmanned Systems. Vol. 1. Iss. 3*, pp. 276-302.

Willems, J., Engblom, W., Moncayo, H., & Nshuti, C. (2018). Verification, Validation, and Application of Shear Stress Transport Transitional Model to a R/C Aircraft. Submitted to AIAA SciTech Forum. *AIAA SciTech Conference.* Kissimmee, FL.

Zilliac, G. G. (1989). *Calibration of Seven-Hole Pressure Probes for Use in Fluid Flows with Large Angularity.* Moffett Field, California: NASA Ames Research Center.

Appendix A: Propulsion Test Data

Hacker A30

Run 1	ESC(A):	50	Batt. Cap (mAh)	1300	Motor Initial Temp	71		Volts	Temp(F)
							Batt. Start	16.75	71
Desc: AR8000 Rx, no PX4, 4S 1300mAh battery									
Time(total)	Power setting	Motor Temp (F)	ESC Temp (F)	Amps	Static updraft (lbf)	End Volts	Batt End	14.71	71.6
1:00	48%	108	91	16.2	2.91	15.66	Delta	-2.04	0.6
3:00	35%	112	101	4.55	1.1	15.38			
5:00	35%	104	85	4.51	1.1	15.17	Date	24-Jan	
7:00	35%	105	84	4.67	1.1	14.98			
9:00	35%	97	85	4.57	1.1	14.8			
10:00	35%	94	82	4.37	1.1	14.71			

Run 2	ESC(A):	70	Batt. Cap (mAh)	1300	Motor Initial Temp	83		Volts	Temp(F)
							Batt. Start	16.66	65
Desc: AR8000 Rx, no PX4, 4S 1300mAh battery									
Time(total)	Power setting	Motor Temp (F)	ESC Temp (F)	Amps	Static updraft (lbf)	End Volts	Batt End	14.85	70
1:00	65%	114	77	13.8	3.1	15.35	Delta	-1.81	5
3:00	50%	104	97	3.6	1	15.13			
5:00	50%	91	99	3.61	0.93	14.94	Date	24-Jan	
7:00	50%	88	96	3.6	0.92	14.84			
9:00	50%	102	97	3.61	0.92	14.72			

Time(total)	Power setting	Motor Temp (F)	ESC Temp (F)	Amps	Static updraft (lbf)	End Volts
10:00	50%	103	96	3.53	0.91	14.85

Run 3	ESC(A):	50	Batt. Cap (mAh)	3500	Motor Initial Temp	74		Volts	Temp(F)
							Batt. Start	16.6	60
Desc: AR8000 Rx, PX4 added, 4S 1300mAh battery									
Time(total)	Power setting	Motor Temp (F)	ESC Temp (F)	Amps	Static updraft (lbf)	End Volts	Batt End	15.5	70
1:00	49%	100	77	13.8	3	15.7	Delta	-1.1	10
3:00	40%	101	97	3.6	1.1	15.67			
5:00	40%	104	99	3.61	1.1	15.58	Date	24-Jan	
7:00	40%	101	96	3.6	1	15.47			
9:00	40%	100	97	3.61	1	15.35			
10:00	40%	101	96	3.53	1	15.5			

Run 4	ESC(A):	50	Batt. Cap (mAh)	1300	Motor Initial Temp	56		Volts	Temp(F)
							Batt. Start	16.37	60
Desc: T1 Flight Pkg, NO PX4									
Time(total)	Power setting	Motor Temp (F)	ESC Temp (F)	Amps	Static updraft (lbf)	End Volts	Batt End	14.81	68.6
1:00	49%	62	62	17.6	3.11	14.57	Delta	-1.56	8.6
3:00	40%	89	84	3.99	1.01	15.05			
5:00	40%	83	83	3.93	1.01	14.91	Date	24-Jan	
7:00	40%	83	89	3.87	0.99	14.77			
9:00	40%	86	88	3.83	0.98	14.69			
10:00	40%	83	76	3.8	0.98	14.81			

Run 5	ESC(A):	50	Batt. Cap (mAh)	3500	Motor Initial Temp	55		Volts	Temp(F)
Desc: T1 Flight Pkg, PX4 in the loop							Batt. Start	15.76	50
Time(total)	Power setting	Motor Temp (F)	ESC Temp (F)	Amps	Static updraft (lbf)	End Volts	Batt End	14.74	59
1:00	49%	84	81	16.96	3.11	14.48	Delta	-1.02	9
3:00	40%	70	69	4.27	1.05	15			
5:00	40%	70	79	4.17	1.04	14.85	Date	24-Jan	
7:00	40%	79	89	4.19	1.05	14.73			
9:00	40%	60	73	4.13	1.02	14.61			
10:00	40%	74	74	4.13	1.03	14.74			

E-Flite P25

Run 1	ESC(A):	70	Batt. Cap (mAh)	1300	Motor Initial Temp			Volts	Temp(F)
Desc: AR8000 Rx, no PX4, 11"x8" prop							Batt. Start	12.44	
Time(total)	Power setting	Motor Temp (F)	ESC Temp (F)	Amps	Static updraft (lbf)	End Volts	Batt End	11.09	102
1:00	75%	86	87	8.96	1.34		Delta	-1.35	102
2:00	75%	88	88	7.8	1.22	11.8			
3:00	100%	109	95	21.6	2.5	11.6	Date	21-Jan	
4:08	100%	117	95	20.3	2.4				

Run 2	ESC(A):	50	Batt. Cap (mAh)	1300	Motor Initial Temp	81		Volts	Temp(F)
Desc: AR8000 Rx, no PX4, 11"x8" prop							Batt. Start	12.59	72
Time(total)	Power setting	Motor Temp (F)	ESC Temp (F)	Amps	Static updraft (lbf)	End Volts	Batt End		
1:00	75%	90	78	15.3	2.24	11.95	Delta	-12.59	-72
2:00	75%	95	76	14.6	2	11.6			
3:00	100%	100	77	22	2.55	11.3	Date	21-Jan	
	100%								

Appendix B: Sailing Conditions

Sailing Conditions at Wind Speed 6 Kts and Wind Direction 90°

Specifications	Value
Horizontal Heading (deg)	-0.7048 (NOTE: 0.0 deg is due North)
Length of Cable (m)	150
SAIL Specifications	
Mass (kg)	3.00
Altitude (m)	150.00
Yaw Angle (deg)	13.980
Pitch Angle (deg)	7.1800
Roll Angle (deg)	-24.789
Angle of Attack (deg)	7.90
Sideslip (deg)	0.00
Position of SAIL relative to Truck	
North (m)	11.8
East (m)	-110.46

Appendix C: Skywalker 1880

Figure. Skywalker 1880

Skywalker Dimensions and Mass Properties

Wing Area (m²)	0.41143
Wing MAC (m)	0.22647
Wingspan (m)	1.88
Horizontal Tail Span (m)	56.26
Horizontal Tail MAC (m)	17.1
Vertical Tail Span (m)	24.4
Vertical Tail MAC (m)	19.5
Total Length (m)	1.183
Weight (Kg)	0.9525